



Eidgenössische Technische Hochschule Zürich  
Swiss Federal Institute of Technology Zurich



Master's thesis in collaboration with the WSL Institute for Snow and Avalanche  
Research SLF

# **The Influence of Forest Structure on Soil Water Balance and Shallow Landslides**

**Annette Temperli - 16 918 450**

**Supervisor:** Dr. Peter Bebi, WSL Institute for Snow and Avalanche Research SLF

**Co-Supervisors:** Dr. Alexander Bast, WSL Institute for Snow and Avalanche Research SLF  
Dr. Frank Graf, WSL Institute for Snow and Avalanche Research SLF

Master's degree programme in Environmental Sciences, Forest and Landscape Management

Davos, 05. December 2022



---

## Abstract

Forest provides an important protective function against shallow landslides and floods. Roots stabilise soil and regulate soil water balance, which can prevent the development of shallow landslides. Studies have shown that the structure of the forest can have a decisive influence on the quality of the protective function of the forest. It is assumed that "well" managed forest stands with high species and structural diversity provide higher protection than "poor" managed forest stands with low species diversity and uniform structure. The effects from structural differences on the soil water balance in the forest, especially with regard to extreme precipitation events, are not yet fully known. In this thesis the soil water content in a forest stand susceptible to landslides in Davos Monstein (GR) was investigated. The focus lied on the comparison of soil moisture dynamics of "well" and "poor" structured forest stands over short- and long-term periods. Electrical resistivity tomography (ERT) was used to observe spatial variations in soil moisture due to precipitation events. In addition, the correlation between coverage rate of the vegetation layers and temporal soil hydrology was investigated. During long-lasting precipitation events and snowmelt, a higher water storage capacity was observed in the "well" structured forest stands, which could be observed from lower increases in soil moisture. Furthermore, over the study period the "well" structured forest stands showed higher volumetric water content, which may be due to lower interception, evapotranspiration and higher water infiltration in the more thinned forest stand. Unfortunately, the ERT survey did not take place during long-lasting precipitation events, thus the results could not accurately visualise the reactions to extreme precipitation events. Nevertheless, the tomograms showed clear differences between the forest stands in terms of rooting intensity and water consumption of the trees in the rooting zone. For a profound understanding, investigations of soil moisture dynamics over longer time periods are needed, with a stronger focus on extreme precipitation events and the effects of regeneration interventions in dense forest stands.

---

---

## Table of Contents

|   |           |
|---|-----------|
| <b>Abstract</b>   | <b>I</b>  |
| <b>List of Tables</b>   | <b>IV</b> |
| <b>List of Figures</b>  | <b>IX</b> |
| <b>1. Introduction</b>  | <b>1</b>  |
| <b>2. Material and Methods</b>  | <b>4</b>  |
| 2.1. Study Area . . . . .   | 4         |
| 2.2. Field Work and Data Collection . . . . .                                       | 5         |
| 2.2.1. Experimental Setup . . . . .   | 5         |
| 2.2.2. Vegetation Recording . . . . .   | 6         |
| 2.2.3. Data Logger and Sensors . . . . .  | 7         |
| 2.2.4. Electrical Resistivity Tomography (ERT) . . . . .                            | 8         |
| 2.2.5. Additional Data . . . . .  | 9         |
| 2.3. Data Analysis . . . . .  | 10        |
| 2.3.1. Vegetation Data . . . . .  | 10        |
| 2.3.2. Logger and Sensor Data . . . . .   | 10        |
| 2.3.3. Electrical Resistivity Data . . . . .  | 10        |
| <b>3. Results</b>   | <b>16</b> |
| 3.1. Vegetation Recording . . . . .   | 16        |
| 3.2. Soil Analysis . . . . .  | 19        |
| 3.3. Logger and Weather Station Data . . . . .                                      | 20        |
| 3.3.1. Overview of the Study Period . . . . .                                       | 20        |
| 3.3.2. Volumetric Water Content . . . . .   | 23        |
| 3.3.3. Soil Temperature . . . . .   | 25        |
| 3.3.4. ERT Survey Periods . . . . .   | 27        |
| 3.4. Electrical Resistivity Tomography-Survey . . . . .                             | 34        |
| 3.4.1. Overview ERT-Survey Sites . . . . .  | 34        |
| 3.4.2. Individual Electrical Resistivity Tomography . . . . .                       | 37        |
| 3.4.3. Time-Lapse Electrical Resistivity Tomography . . . . .                       | 41        |
| 3.4.4. Analysis Electrical Resistivity Values . . . . .                             | 44        |
| 3.4.5. Correlation of Electrical Resistivity and Volumetric Water Content . . . . . | 48        |
| <b>4. Discussion</b>  | <b>50</b> |
| 4.1. Vegetation Recording . . . . .   | 50        |
| 4.2. Logger and Weather Station Data . . . . .                                      | 51        |
| 4.3. Electrical Resistivity Tomography . . . . .                                    | 53        |
| <b>5. Conclusion</b>  | <b>56</b> |
| <b>6. Declaration of Originality</b>  | <b>61</b> |
| <b>7. Appendix</b>  | <b>62</b> |
| <b>A. Vegetation Recording</b>  | <b>62</b> |
| A.1. Results Vegetation Recording . . . . .   | 62        |
| A.2. Species List of Herb and Shrub Layer . . . . .                                 | 70        |
| A.3. Photo Documentation of the Vegetation Recording . . . . .                      | 71        |
| <b>B. Soil Analysis</b>   | <b>85</b> |
| B.1. Photo Documentation Soil Profile . . . . .                                     | 85        |



|  |           |
|--|-----------|
| <b>C. Logger and Weather Station Data</b>                | <b>87</b> |
| C.1. Kruskal-Wallis Test . . . . .                       | 87        |
| <b>D. Electrical Resistivity Tomography</b>              | <b>90</b> |
| D.1. Output Inversion . . . . .                          | 90        |
| D.2. Inversions with Wenner-Schlumberger Array . . . . . | 93        |
| D.3. Resistivity Analysis with WENSL Array . . . . .     | 97        |

---

## List of Tables

|    |   |    |
|----|---|----|
| 1. | Overview of the categories for the vegetation recording. For each layer soil, herb, shrub and tree, the coverage of the different categories were recorded. . . . .   | 7  |
| 2. | Overview of the technical specification from the Sensors Teros 12 and 21 [24, 25]. .  | 8  |
| 3. | Overview of the technical specification from the All-in-One Weather Station Atmos 41 [23]. . . . .  | 8  |
| 4. | Calculated values in x- and z-direction to extract the corresponding electrical resistivity values at the different VWC sensor depths. . . . .  | 15 |
| 5. | Overview of the soil horizons of the sites Well001 and Poor_meas001. The soil profiles were done during the sensor installation. . . . .  | 20 |
| 6. | Overview of the recorded species with the corresponding indicators. The ecological indicator values according to Landolt et. al. include the factors: moisture index F, reaction index R, nutrient index N, light index L, temperature index T, continent index K. Site name are abbreviated. . . . .   | 70 |
| 7. | Overview of the time-lapse resistivity inversions. The column measurements read shows the number of measurements which were used for the inversion after filtering im pre-processing. The number of inversions describes the number of calculation runs needed to achieve a result in the desired range. The Final RMS Misfit describes the achieved error at the last inversion. . . . .                 | 90 |
| 8. | Overview of the output from the individual resistivity inversions. The column measurements read shows the number of measurements which were used for the inversion after filtering im pre-processing. The number of inversions describes the number of calculation runs needed to achieve a result in the desired range. The Final RMS Misfit describes the achieved error at the last inversion. . . . . | 91 |

## List of Figures

|            |  |    |
|------------|--|----|
| Figure 1.  | General map of the study area Lücherwald below Davos Monstein. The black crosses give an overview of the sites, where the sensors and data loggers were installed [8]. . . . .   | 4  |
| Figure 2.  | Overview of the experimental setup on each site. The six vegetation recording areas are shown in green, with a distance of 2.5 m to each end. The data logger with the sensors lies approximately in the centre of the site. The red line represents the ERT profile line, which was only installed at site Well001 and Poor_meas001. . . . .  | 6  |
| Figure 3.  | Soil Temperature values from the sensor Teros 12 at depth of 30 cm during the ERT survey period. On the left for July and on the right side for August. . . . .  | 11 |
| Figure 4.  | Triangular meshes as input parameter for the inversion in ResIpy. The meshes were constructed for dipole-dipole arrays on the left side is the profile from Well001 and on the right side Poor_meas001. . . . .  | 12 |
| Figure 5.  | Triangular meshes as input parameter for the inversion in ResIpy. The meshes were constructed for Wenner-Schlumberger arrays on the left side is the profile from Well001 and on the right side Poor_meas001. . . . .  | 13 |
| Figure 6.  | Overview of the used general and advanced inversion settings in the software ResIpy. . . . .   | 14 |
| Figure 7.  | Coverage rates in percentage from all vegetation layers (soil, herb, shrub and tree) at the first day of recording 13.05.2022. The stackbars are divided in the shown categories. The brown shades described the categories in the soil layer, the blue-green shades the categories in the herb layer, the red shades the categories in the shrub layer and yellow the canopy cover in the tree layer. . . . .   | 17 |
| Figure 8.  | Coverage rates in percentage from all vegetation layers (soil, herb, shrub and tree) at the last day of recording 05.08.2022. The stackbars are divided in the shown categories. The brown shades described the categories in the soil layer, the blue-green shades the categories in the herb layer, the red shades the categories in the shrub layer and yellow the canopy cover in the tree layer. . . . .  | 18 |
| Figure 9.  | Development of the coverage rate in percentage from the herb layer over the entire recording period. The stackbars are divided in the shown categories. The blue-green shades describe the categories in the herb layer . . . . .  | 19 |
| Figure 10. | Grain size distribution curve as result of the soil sample analysis from Lücherwald. The curve shows the weight percent of each specific grain size. . . . .   | 20 |
| Figure 11. | Overview of the weather and volumetric water content VWC data during the study period February to August 2022. <b>A</b> Daily precipitation from weather station Lücherwald with the supplementing of precipitation from the weather station Davos Dorf in May and June, <b>B</b> Total snow depth from weather station Monstein Dorf, <b>C</b> Daily average temperature from weather station Lücherwald, <b>D</b> VWC at 10 cm from all sites, <b>E</b> VWC at 30 cm from all sites, <b>F</b> VWC at 50 cm from all sites. The purple highlighted areas indicate interesting events. <b>1</b> Start of snowmelt, <b>2</b> Long precipitation event, <b>3</b> Dry phase, <b>4</b> First reaction of all VWC values after dry phase. . . . . | 22 |
| Figure 12. | Boxplots of the VWC values at 10 cm depth from all sites. All values of the study period from February to August 2022 are included. . . . .  | 23 |
| Figure 13. | Boxplots of the VWC values at 30 cm depth at all sites. All values of the study period from February to August 2022 are included. . . . .  | 24 |
| Figure 14. | Boxplots of the VWC values at 50 cm depth at all sites. All values of the study period from February to August 2022 are included. . . . .  | 25 |
| Figure 15. | Boxplots of the soil temperature values at 10 cm depth from all sites. All values of the study period from February to August 2022 are included. . . . .   | 26 |
| Figure 16. | Boxplots of the soil temperature values at 30 cm depth at all sites. All values of the study period from February to August 2022 are included. . . . .   | 26 |
| Figure 17. | Boxplots of the soil temperature values at 50 cm depth at all sites. All values of the study period from February to August 2022 are included. . . . .   | 27 |

|  |    |
|--|----|
| Figure 18. Overview of the weather and volumetric water content data during the ERT survey period in July from 02.07-26.07 with focus on the sites Poor_meas001 and Well001. <b>A</b> Hourly precipitation from weather station Lücherwald, <b>B</b> Air temperature from weather station Lücherwald, <b>C</b> Vapour pressure deficit from weather station Lücherwald, <b>D</b> VWC at 10 cm from sites Poor_meas001 and Well001, <b>E</b> VWC at 30 cm from sites Poor_meas001 and Well001, <b>F</b> VWC at 50 cm from sites Poor_meas001 and Well001. The purple highlighted areas indicate the ERT survey dates. . . . . | 29 |
| Figure 19. Overview of the weather and volumetric water content data during the ERT survey period in August from 16.08-23.08 with focus on the sites Poor_meas001 and Well001. <b>A</b> Hourly precipitation from weather station Lücherwald, <b>B</b> Air temperature from weather station Lücherwald, <b>C</b> Vapour pressure deficit from weather station Lücherwald, <b>D</b> VWC at 10 cm from sites Poor_meas001 and Well001, <b>E</b> VWC at 30 cm from sites Poor_meas001 and Well001, <b>F</b> VWC at 50 cm from sites Poor_meas001 and Well001. The purple highlights indicate the ERT survey dates . . . . .     | 30 |
| Figure 20. Detailed illustration of precipitation from the weather station Lücherwald and VWC during the ERT survey period. The left figure covers the measurement from 19.07. and the right figure the measurement from 21.07.. The purple highlighted areas indicate the time period of the survey. . . . .  | 31 |
| Figure 21. Detailed illustration of precipitation at the weather station Lücherwald and VWC during the ERT survey period. The left figure covers the measurement from 22.07. and the right figure the measurement from 24.07.. The purple highlighted areas indicate the time period of the survey. . . . .  | 32 |
| Figure 22. Detailed illustration of the precipitation at weather station Lücherwald and the volumetric water content VWC during the ERT survey period. The left figure covers the measurement from the 18.08. and the right figure the measurement from the 19.08.. The purple highlights indicate the time period of the survey. . . . .  | 33 |
| Figure 23. Detailed illustration of the precipitation at weather station Lücherwald and the volumetric water content VWC during the ERT survey period. The figure covers the measurement from the 22.08.. The purple highlights indicate the time period of the survey. . . . .  | 33 |
| Figure 24. Electrical resistivity tomogram at site Well001 from the 18.08. with dipole-dipole array. For a better orientation and imagination, the vegetation layers were drawn schematically, as well as a scale for the depth. The white numbers indicate the number of the electrodes. . . . .  | 34 |
| Figure 25. Electrical resistivity tomogram at site Poor_meas001 from the 18.08. with dipole-dipole array. For a better orientation and imagination, the vegetation layers were drawn schematically, as well as a scale for the depth. The white numbers indicate the number of the electrodes. . . . .   | 35 |
| Figure 26. Overview maps of the ERT survey site Well001. The map gives an impression of how many trees are located at the sites as the exact location. The radius of the circle gives an indication of the DBH of the trees. The blue dots indicate regeneration that was too small to record the DBH mass. . . . .  | 36 |
| Figure 27. Overview maps of the ERT survey site Poor_meas001. The map gives an impression of how many trees are located at the sites as the exact location. The radius of the circle gives an indication of the DBH of the trees. The blue dots indicate regeneration that was too small to record the DBH mass. . . . .   | 36 |
| Figure 28. Individual electrical resistivity tomograms from the sites Poor_meas001 and Well001 with the dipole-dipole array from the July survey. The tomograms from 19., 21., 22. and 24.07. are shown. . . . .   | 39 |
| Figure 29. Individual electrical resistivity tomograms from the sites Poor_meas001 and Well001 with the dipole-dipole array from the August survey. The tomograms from the 18., 19., and 22.08. are shown. . . . .   | 40 |

|   |    |
|---|----|
| Figure 30. Time-lapse electrical resistivity tomograms from the sites Poor_meas001 and Well001 with the dipole-dipole array from the July survey. From the 19.07. the electrical resistivity tomogram is shown. From the 21, 22. and 24.07. the difference tomograms are shown. . . . .   | 42 |
| Figure 31. Time-lapse electrical resistivity tomograms from the sites Poor_meas001 and Well001 with the dipole-dipole array from the July survey. From the 18.08. the electrical resistivity tomogram is shown. From the 19. and 22.08. the difference tomograms are shown. . . . .   | 43 |
| Figure 32. Boxplots of the modelled electrical resistivity values of the dipole-dipole array during July survey. All survey dates are presented. . . . .  | 45 |
| Figure 33. Histograms of the modelled electrical resistivity values of the dipole-dipole array during July survey. All survey dates are presented. <b>A</b> Poor_meas001 and <b>B</b> Well001 . . . . .   | 46 |
| Figure 34. Boxplots of the modelled electrical resistivity values of the dipole-dipole array during August survey. All survey dates are presented. . . . .  | 47 |
| Figure 35. Histograms of the modelled electrical resistivity values of the dipole-dipole array during August survey. All survey dates are presented. <b>A</b> Poor_meas001 and <b>B</b> Well001 . . . . .   | 47 |
| Figure 36. Scatter plot of VWC and electrical resistivity values from depths 30 and 50 cm. Data points from both sites and all ERT surveys were used. The blue trend line shows a smoothed curve according to the method LOESS. . . . .   | 49 |
| Figure 37. Scatter plot of VWC and electrical resistivity values separated by depth. Data points from both sites and all ERT surveys were used. The blue line shows a smoothed curve according to the method LOESS. The green and red lines show the smoothed curve of the respective site. On the left side are the data points from 30 cm and on the right side the data points from 50 cm illustrated. . . . . | 49 |
| Figure 38. Coverage rates in percentage from all vegetation layers (soil, herb, shrub and tree) at 19.05.2022. The stackbars are divided in the shown categories. The brown shades described the categories in the soil layer, the blue-green shades the categories in the herb layer, the red shades the categories in the shrub layer and yellow the canopy cover in the tree layer . . . . .                   | 62 |
| Figure 39. Coverage rates in percentage from all vegetation layers (soil, herb, shrub and tree) at 27.05.2022. The stackbars are divided in the shown categories. The brown shades described the categories in the soil layer, the blue-green shades the categories in the herb layer, the red shades the categories in the shrub layer and yellow the canopy cover in the tree layer . . . . .                   | 63 |
| Figure 40. Coverage rates in percentage from all vegetation layers (soil, herb, shrub and tree) at 03.06.2022. The stackbars are divided in the shown categories. The brown shades described the categories in the soil layer, the blue-green shades the categories in the herb layer, the red shades the categories in the shrub layer and yellow the canopy cover in the tree layer . . . . .                   | 64 |
| Figure 41. Coverage rates in percentage from all vegetation layers (soil, herb, shrub and tree) at 10.06.2022. The stackbars are divided in the shown categories. The brown shades described the categories in the soil layer, the blue-green shades the categories in the herb layer, the red shades the categories in the shrub layer and yellow the canopy cover in the tree layer . . . . .                   | 65 |
| Figure 42. Coverage rates in percentage from all vegetation layers (soil, herb, shrub and tree) at 17.06.2022. The stackbars are divided in the shown categories. The brown shades described the categories in the soil layer, the blue-green shades the categories in the herb layer, the red shades the categories in the shrub layer and yellow the canopy cover in the tree layer . . . . .                   | 66 |

|   |    |
|---|----|
| Figure 43. Coverage rates in percentage from all vegetation layers (soil, herb, shrub and tree) at 24.06.2022. The stackbars are divided in the shown categories. The brown shades described the categories in the soil layer, the blue-green shades the categories in the herb layer, the red shades the categories in the shrub layer and yellow the canopy cover in the tree layer . . . . . | 67 |
| Figure 44. Coverage rates in percentage from all vegetation layers (soil, herb, shrub and tree) at 08.07.2022. The stackbars are divided in the shown categories. The brown shades described the categories in the soil layer, the blue-green shades the categories in the herb layer, the red shades the categories in the shrub layer and yellow the canopy cover in the tree layer . . . . . | 68 |
| Figure 45. Coverage rates in percentage from all vegetation layers (soil, herb, shrub and tree) at 22.07.2022. The stackbars are divided in the shown categories. The brown shades described the categories in the soil layer, the blue-green shades the categories in the herb layer, the red shades the categories in the shrub layer and yellow the canopy cover in the tree layer . . . . . | 69 |
| Figure 46. Photo documentation of the vegetation recording from the first (13.05.2022) and last (05.08.2022) recording day at site Meteo. . . . .   | 72 |
| Figure 47. Photo documentation of the vegetation recording from the first (13.05.2022) and last (05.08.2022) recording day at site Well001. . . . .   | 74 |
| Figure 48. Photo documentation of the vegetation recording from the first (13.05.2022) and last (05.08.2022) recording day at site Well002. . . . .   | 76 |
| Figure 49. Photo documentation of the vegetation recording from the first (13.05.2022) and last (05.08.2022) recording day at site Poor_meas001. . . . .  | 78 |
| Figure 50. Photo documentation of the vegetation recording from the first (13.05.2022) and last (05.08.2022) recording day at site Poor_meas002. . . . .  | 80 |
| Figure 51. Photo documentation of the vegetation recording from the first (13.05.2022) and last (05.08.2022) recording day at site Poor001. . . . .   | 82 |
| Figure 52. Photo documentation of the vegetation recording from the first (13.05.2022) and last (05.08.2022) recording day at site Poor002. . . . .   | 84 |
| Figure 53. Soil profile at Well001 with depth of 60 cm. The soil profile was done during the installation of the sensor and data loggers. . . . .   | 85 |
| Figure 54. Soil profile at Poor_meas001 with depth of 60 cm. The soil profile was done during the installation of the sensor and data loggers. . . . .  | 86 |
| Figure 55. Result of Kruskal-Wallis rank sum test and Dunn test with the method "Holm" with the variable VWC at depth 10 cm. . . . .  | 87 |
| Figure 56. Result of Kruskal-Wallis rank sum test and Dunn test with the method "Holm" with the variable VWC at depth 30 cm. . . . .  | 87 |
| Figure 57. Result Kruskal-Wallis rank sum test and Dunn test with the method "Holm" with the variable VWC at depth 50 cm. . . . .   | 88 |
| Figure 58. Result Kruskal-Wallis rank sum test and Dunn test with the method "Holm" with the variable soil temperature at depth 10 cm. . . . .  | 88 |
| Figure 59. Result Kruskal-Wallis rank sum test and Dunn test with the method "Holm" with the variable soil temperature at depth 30 cm. . . . .  | 89 |
| Figure 60. Result Kruskal-Wallis rank sum test and Dunn test with the method "Holm" with the variable soil temperature at depth 50 cm. . . . .  | 89 |
| Figure 61. Individual electrical resistivity tomograms from the sites Poor_meas001 and Well001 with the Wenner-Schlumberger array from the July survey. The tomograms from 19., 21., 22. and 24.07. are shown. . . . .  | 93 |
| Figure 62. Individual electrical resistivity tomograms from the sites Poor_meas001 and Well001 with the Wenner-Schlumberger array from the August survey. The tomograms from the 18., 19., and 22.08. are shown. The data set from 19.08. at Poor_meas001 is invalid. . . . .   | 94 |

---

|  |    |
|--|----|
| Figure 63. Time-lapse electrical resistivity tomograms from the sites Poor_meas001 and Well001 with the Wenner-Schlumberger array from the July survey. From the 19.07. the electrical resistivity tomogram is shown. From the 21, 22. and 24.07. the difference tomograms are shown. . . . .  | 95 |
| Figure 64. Time-lapse electrical resistivity tomograms from the sites Poor_meas001 and Well001 with the Wenner-Schlumberger array from the July survey. From the 18.08. the electrical resistivity tomogram is shown. From the 19. and 22.08. the difference tomograms are shown. The data set from 19.08. at Poor_meas001 is invalid. . . . . | 96 |
| Figure 65. Boxplot of the modelled electrical resistivity values of the Wenner-Schlumberger array during July survey. <b>A</b> Poor_meas001 and <b>B</b> Well001 . . . . .   | 97 |
| Figure 66. Histogram of the modelled electrical resistivity values of the Wenner-Schlumberger array during July survey. . . . .  | 98 |
| Figure 67. Boxplots of the modelled electrical resistivity values of the Wenner-Schlumberger array during August survey. . . . .   | 98 |
| Figure 68. Histograms of the modelled electrical resistivity values of the Wenner-Schlumberger array during August survey. <b>A</b> Poor_meas001 and <b>B</b> Well001 . . . . .  | 99 |

## 1. Introduction

Forest has an important protective function against landslides and floods due to the positive effect on the soil water balance. Forest cover especially protects from shallow landslides, which occur at a depth of 0 - 2 m and thus are formed in the rooting zone of the trees. The tree roots exert a mechanical reinforcement on the soil and can affect the intensity of landslides. Furthermore, forest influences the soil water balance through interception, transpiration and improved water infiltration. An ideal forest stand can improve the stability conditions of a slope angle, and thus a lower landslide activity can be expected. However, from a slope angle of 40°, the protective function of the forest decreases significantly [13].

The protective effect of forest strongly depends on the intensity of the precipitation event. While short precipitation events in dry conditions are almost completely absorbed by interception, the effect of forest decreases with longer precipitation events. Extreme precipitation events are particularly critical in the period after snowmelt, when the soil is largely saturated and only part of the storage capacity is available. During these conditions, the risk for a shallow landslide event is high, because the soil will be saturated with a smaller amount of precipitation. Soil properties are decisive for the water storage capacity of the forest, whereby it was characterised by the parent material, climate and relief. Depending on soil properties such as depth and permeability, the influence of the forest cover can vary, because deep, normally permeable soils have a higher storage effect than shallow, heavily waterlogged soils. Moreover, intensity and depth of rooting creates a cavity system in the soil and thus increases permeability. This allows deeper water infiltration, since more of the existing water storage capacity of the soil can be utilised. Furthermore, water infiltration strongly depends on the ground cover and vegetation. In heavily compacted soils or large litter layers, the conditions for fast infiltration are poorer than in the case of an intensive herb layer. During extreme events, the infiltration capacity of the soil is important, as poor water infiltration results in more surface runoff, which can lead to soil erosion [13].

Various studies have shown that the structure of the forest stand has a distinct influence on its protective function against shallow landslides. This means that "well" managed and structured forests provide better protection against shallow landslides [5, 14, 26]. A high soil stability can be achieved through intensive and deep rooting, whereby the rooting intensity increases with the canopy cover. In addition, a well horizontal and vertical distribution of the root growth over the entire ground is decisive. With high species and age diversity, a high diversity in the rooting zone can be achieved, due to the different characteristics and rooting depths of the species. Therefore, the ideal forest structure is a small-scale, uneven-aged stand with a high canopy cover, whereby a stable regeneration is important for a long-term protection effect [13].

The analysis of Bebi et al. (2019) has shown that coniferous forests, especially spruce stands, are more susceptible to shallow landslides due to the lower soil stabilisation of shallow-rooted spruce [5]. The result of the study was that not only the occurrence of forest but also the history and structure is relevant for the protective function. The authors pointed out that due to natural forest dynamics and disturbances, the protective function against shallow landslides cannot always be guaranteed. They recommend an adapted forest management, which increases the resilience of forests and maintains the protective function with particular focus on well-timed, structure improving interventions. However, the large-scale study could not conclusively say where the priorities lie with regard to long-term protection against shallow landslides [5].

The intensity of stand interventions must be chosen carefully, as too large gaps can promote landslides and erosion. The gaps should only be as large as necessary to ensure long-term regeneration in the stand. The stabilising effect of dead roots is still guaranteed, but decreases after a few years. The range of intervention depends strongly on the slope and the soil material. The guideline values for the critical slope angle inclination differ depending on the type of unconsolidated rock: clay-rich soils have a critical guideline value from 25° and well-drained, sandy-gravelly soils have a



value from 35°. In the case of steep forest stands above the critical slope, the forest structure is of great importance, but the intervention possibilities are limited to small areas in order to prevent landslides [13]. A study by Moos et al. (2016) showed that gaps longer than 20 m in fall line critically increase the probability of a shallow landslide event [26].

The formation of shallow landslides is closely related to the process of water saturation and the increase of pore water pressure in the soil. To prevent landslide initiation, the soil must have an appropriate water retention capacity. High diversity in vegetation and succession stage promotes the stability of the soil structure and increases the water retention capacity. In first investigations in the Dischma valley, Davos (GR), the soil water content was measured in different structured forest stands. The results showed higher water storage capacity in the "well" structured forest stand compared to the "poor" structured forest. As a consequence, the soil can store more water until being saturated and thus delays or prevents the formation of shallow landslides [15].

The impact of forests on soil and slope instabilities is still a current subject for science and practice and therefore needs further investigation. This thesis is part of the research project "WaWaRu - Waldstruktur, Wasserhaushalt und flachgründige Rutschungen" conducted by the WSL Institute for Snow and Avalanche Research SLF [4]. The project uses a multifaceted approach to investigate the effect of forest structure on soil and slope instabilities. The focus lies on the interaction between forest structure, soil hydrology and evapotranspiration. The investigation includes different single point measurements on soil hydrology in "well" and "poor" structured forest stands. At two of the sites, a regeneration cut is planned. Therefore, the effect of the intervention on the soil water balance can also be investigated. Furthermore, electrical resistivity tomography (ERT) is used to measure the relative change of soil moisture along a two-dimensional section in the topsoil with the focus on precipitation events. The project is located in a potential risk area for shallow landslides near Davos Monstein. The location was selected because a landslide event occurred in a nearby area after an intervention. Based on this event, the forest stand was assumed to be a potential landslide area. In addition to the science aspect, the project intends to generate practical insights for protection forest management. The project works in close cooperation with the Rhaetian Railway, the Grisons Office for Forestry and Natural Hazards and the Davos Forestry Service.

Electrical Resistivity Tomography ERT is a widely used geophysical method to determine lateral resistivity changes along a profile and in depth. The method has been introduced mainly in geology and soil science [19]. Heterogeneity in the soil surface leads to spatial differences in soil moisture, which cannot be shown using single point measurement, therefore ERT is a suitable alternative. ERT provides to be useful for investigating spatial variations in soil moisture and the effect of vegetation on it [10]. Using Archie's law, soil moisture could be estimated directly from the measured resistivities through electrical conductivity of saturated porous medias, but this was not applied in this thesis [3].

The ERT method was not widely applied in hydrobiology or more specific in forest research yet. For example a study from Dick et al. (2018) compared soil moisture dynamics among contrasting vegetation types in the Scottish Highlands [10]. The aim was to analyse the spatiotemporal variability in soil moisture between a scots pine forest and a heather moorland shrub. The result of the study showed that the soil moisture patterns under the forest were much more heterogeneous than under the pasture, which may be related to the vegetation distribution and canopy structure. The use of ERT methods allowed a visualisation and quantification of vegetation-soil water interactions at different spatial scales and resolutions, which would not have been possible with point measurements alone.

In the study by Fäth et al. (2022), ERT method was applied in the forest to investigate spatiotemporal soil moisture changes in the subsurface. This study focused more on seasonal and interannual soil moisture dynamics in a forest to better understand the impact of damaging events

such as droughts. The results of the study provided a multidimensional representation of soil moisture changes in the rooting zone. The authors identified that even deeper subsurface areas could be important for the water supply of forest areas, which has not yet been recorded. Nevertheless, they see the ERT method as insufficient to make quantitative statements about soil moisture, as calibration with pF (index for matrix potential), water content and soil physics would be further necessary [12].

Regarding shallow landslides, Wicki et al. (2022) used the ERT method to monitor critical saturated conditions in a landslide-prone area. In this study ERT, in situ soil moisture sensor and tensiometer measurements were performed regularly over nine months, to further calculate critical saturated conditions for a regional landslide activity. The technique was found to be suitable for early detection of shallow landslides, especially for spatial soil moisture changes [34].

The aim of this thesis is to analyse the influence of forest structure on the soil water balance and thus on shallow landslides. The focus lies particularly on soil moisture dynamics during precipitation events, but also on long-term and short-term trends over the study period. For this purpose, forest areas with different structural characteristics were compared for seven months and soil moisture data was analysed. In addition, ERT surveys were carried out at a "well" and a "poor" structured forest stand, with focus on precipitation events.

This thesis investigates two main research questions:

1. Are short- or longterm differences between the sites recognisable, especially after a precipitation event regarding soil moisture and electrical resistivity?
2. Is there a correlation between temporal soil hydrology and the coverage rate of the vegetation layers?

## 2. Material and Methods

### 2.1. Study Area

The study area is located in Davos Monstein (GR) at a forest stand below the village. The name of the study area is "Lücherwald". The forest area is located at about 1500 m. a.s.l. and is oriented towards northwest. The average slope angle is between 30 and 35 degrees. According to the Geological Atlas of Switzerland, the forest stand lies on delta gravel and alluvial moraine fill of the early postglacial lake of the Davos valley [32]. The mean annual precipitation at the site amounts 1040 mm per year according to the hydrological atlas of Switzerland [27].

The forest stand is a typical spruce dominated stand of the continental high Alps. The cantonal forest type map shows that the Lücherwald lies in the high montane zone and corresponds to type 55VM *Veronico latifoliae-Piceetum melampyretosum silvatici* based on the classification by Ellenberg and Klötzli (1972) [11]. Furthermore, in the cantonal geoportal, the forest stand is classified as a protection forest of category A (high risk). The forest stand map of the canton gives the following assessment of the Lücherwald stand. The origin and management type of the forest corresponds to high forest and the development stage is estimated to be middle-aged timber trees, which means a diameter at breast height (DBH) of 36-52 cm. The crown closure is given as normal to open with a canopy cover of 80 %. The structure is classified as layered, which means a distinct crown layer and further lower trees, which can be spatially clearly separated. The stability condition is classified as stable-labile, because of a weak structure or texture of the stand. According to the cantonal instructions for forest stand mapping, a stable-labile structure and texture is defined by the following characteristics: weak stratification, partially structured, without missing parts and slight crowding of the trees. The regeneration cover in the stand is estimated at 10 %, with primarily spruce present and occasional larch and rowan. The urgency of regeneration is considered as necessary. Overall, the general need for action in the stand is rated as high [2, 18].

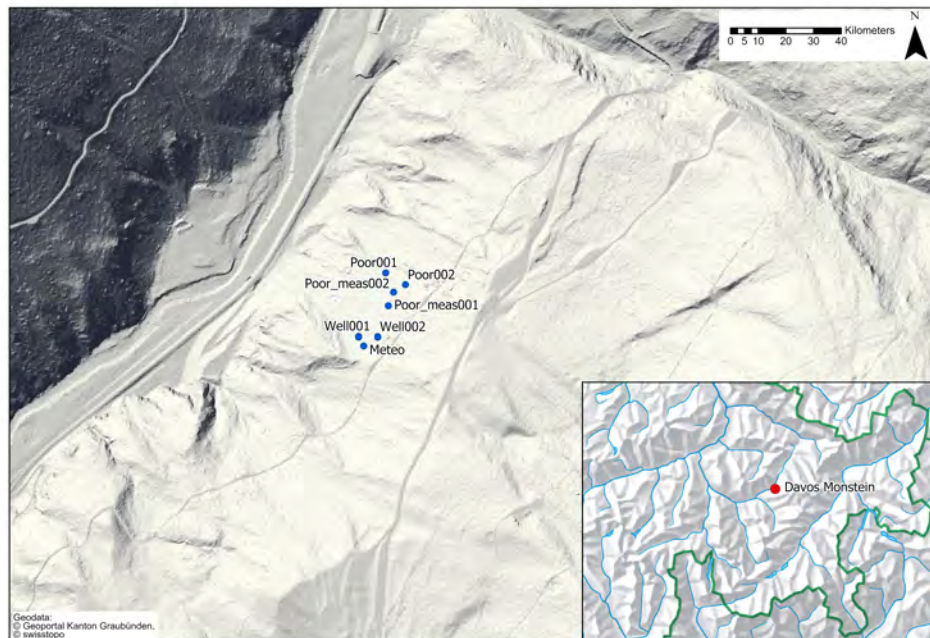


**Figure 1:** General map of the study area Lücherwald below Davos Monstein. The black crosses give an overview of the sites, where the sensors and data loggers were installed [8].

## 2.2. Field Work and Data Collection

### 2.2.1. Experimental Setup

In the project "WaWaRu" the forest stand was divided into two "well" and four "poor" structured forest stands, with future regeneration intervention planned in two of the "poor" structured stands. Thereby sites Well001 and Well002 were situated in the "well" structured forest stand. Sites Poor001 and Poor002 were situated in the "poor" structured forest stand. Sites Poor\_meas001 and Poor\_meas002 were also situated in the "poor" structured forest stand, but there the regeneration intervention is planned. Site Meteo is an exception, as it is located centred in a large gap. Figure 1 gives an overview of the site arrangement in the Lücherwald. It is important to point out that the terms "well" and "poor" are used for simplicity in this thesis, to point out the different forest structure of the sites. This refers to the fact that the "well" sites are located in a more open stand than the "poor" sites. The horizontal structure in the "well" structured stand shows more gaps with a mixed distribution of DBH. In contrast, the "poor" structured forest stand is rather a dense stand with a low diameter distribution. The vertical structure of the "well" structured forest stand shows significantly more layers than the "poor" structured forest stand, which is mainly single-layered. Furthermore, there is only occasional tree regeneration present. The "well" sites are located in a multi-layered stand with a high tree regeneration cover and shrub layer. Even though the canopy cover is not strongly developed, because the sites lie at the border of a large gap. In terms of species, the sites do not differ much in the tree layer, but more differences can be seen in the lower layers. A more detailed description of the different vegetation layers and species can be found in the results 3.1.

The field experiment was set up as follows. As part of the "WaWaRu" project, seven data loggers and one weather station have been installed in the year 2020. The weather station is located in a larger forest gap on purpose, to be more exposed to the weather. For this thesis an area of 14 by 2 m was marked out on each of the seven experimental sites. On every site, six vegetation recording areas have been marked out, which have a size of 1 by 1 m. At the sites Well001 and Poor\_meas001 a line of 11.75 m was laid approximately in the middle of the field for the electrical resistivity survey. Figure 2 gives an overview of the experimental setup. More detailed description of the methods of measurement follows in the chapters 2.2.3, 2.2.4 and 2.2.2.

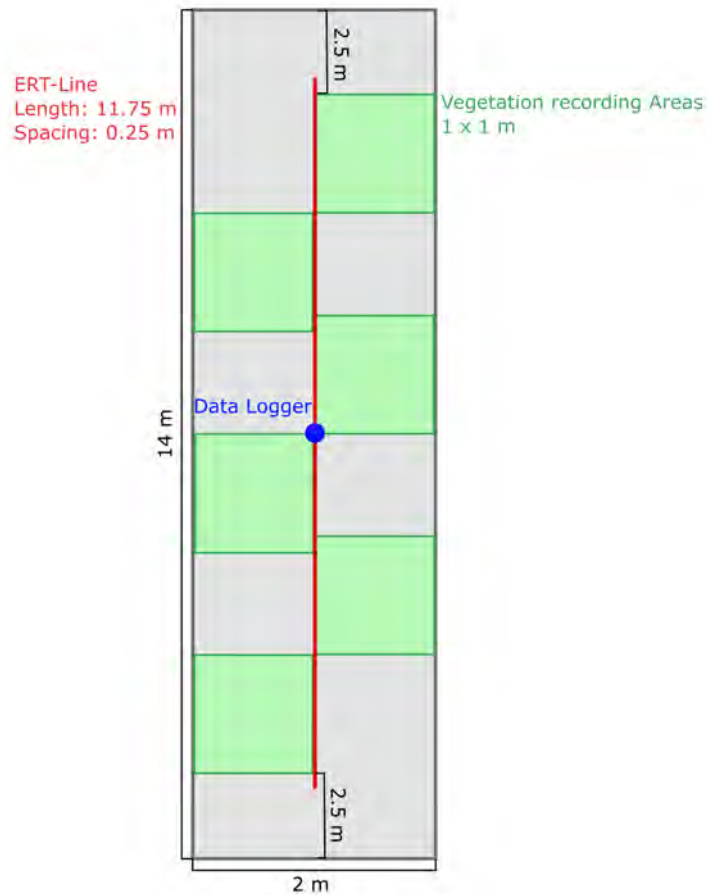


**Figure 2:** Overview of the experimental setup on each site. The six vegetation recording areas are shown in green, with a distance of 2.5 m to each end. The data logger with the sensors lies approximately in the centre of the site. The red line represents the ERT profile line, which was only installed at site Well001 and Poor\_meas001.

### 2.2.2. Vegetation Recording

From the 13.05. until the 05.08.2022 the vegetation coverage of all layers was recorded and its development observed. First, they were carried out weekly until 24.06. and then every two weeks until the 05.08.. According to the experimental design (see figure 2), the vegetation surveys were done in the green squares. The aim was to obtain a sample selection. The vegetation cover was recorded for each of four layers, the soil, herb, shrub and tree layer. The different layers were defined as follows: The herb layer includes all plants up to one meter and the shrub layer all plants from one to three meters, after that it counts to the tree layer. The vegetation was recorded according to different categories for each layer. Table 1 gives an overview for all the categories. For each vegetation layer, the percentage cover was determined. Whereby a maximum coverage of 100 % was assumed for each layer. As an aid, a mapping frame was used, which had the size of 1 m<sup>2</sup> and was divided in squares of 10 cm<sup>2</sup>. In the herb layer, most of the plants which do not match into one of the listed categories, were grouped together in the herb category. Thereby, the species was noted, although it is not an exhaustive list (see appendix A.2). The mosses were not recorded by species only the rate of coverage. As documentation, photos of the squares were taken for each survey, which are attached in the appendix A.3. Only the pictures of the first (13.05.2022) and last (05.08.2022) vegetation recording are attached, the remaining pictures can be found in the electrical appendix. The recording of the canopy cover was carried out only once at the 13.05.,

because it was assumed that the canopy would not change significantly over the recording time. The soil layer also showed only minor changes during the observation period, which are no longer visible in the results due to the further processing of the raw data. The vegetation surveys were all carried out by the same person, so that a uniform estimation can be assumed.

**Table 1:** Overview of the categories for the vegetation recording. For each layer soil, herb, shrub and tree, the coverage of the different categories were recorded.

| Layer       | Categories            |
|-------------|-----------------------|
| Soil Layer  | Stone                 |
|             | Soil                  |
|             | Root                  |
|             | Moss                  |
|             | Litter                |
|             | Dead Wood             |
| Herb Layer  | Vaccinium vitis-idaea |
|             | Vaccinium myrtillus   |
|             | Sorbus aucuparia      |
|             | Picea abies           |
|             | Larix decidua         |
| Shrub Layer | Herb                  |
|             | Lonicera nigra        |
| Tree Layer  | Lonicera alpigena     |
|             | Tree Crown            |

### 2.2.3. Data Logger and Sensors

At the start of the "WaWaRu" project seven data loggers with five sensors each were installed on every site. The measurement equipment was purchased from the Meter Group. Both sensor types Teros 12 and 21 were installed at depths of 10 and 30 cm, whereas Teros 12 was additionally installed at 50 cm. The sensor Teros 12 measures volumetric water content (VWC), soil temperature and electrical conductivity (EC). In the following, only the measuring techniques of the variables used in this thesis, VWC and soil temperature, are explained. Teros 12 measures the quantity of water contained in soil using the time-domain reflectometry (TDR-method). An electromagnetic field is used to measure the dielectric permittivity of the surrounding medium. The varying reflection of an electrical pulse generated at the end of the metal probe determines the dielectric constant, which depends on the water content of the medium. The Teros 12 sensor measures the charging time and outputs a raw value based on the dielectric constant of the substrate. Water and soil components differ greatly in their dielectric constant, while also a linear relationship exists between absolutely dry soil and pure water. Thus, changes in the VWC are directly recognisable through changed reflection velocities of the pulse [1]. The soil temperature is measured with a thermistor at the centre needle of the Teros 12 sensor [24].

The sensor Teros 21 measures soil water potential and soil temperature. Table 2 provides an overview of the sensors and their measurement variables, as well as their resolution and accuracy. Due to the higher accuracy of the sensor Teros 12 regarding the soil temperature measurement, the values of the Teros 12 were considered in this thesis.

At site Meteo, in addition to the data logger and sensors, an "All-in-One Weather Station Atmos 41" was installed. It performs the following measurements: solar radiation, precipitation, relative humidity, air temperature, humidity sensor temperature, vapour pressure, barometric pressure, horizontal wind speed, wind gust, wind direction, tilt, lightning strike count and lightning average distance. Table 3 gives an overview of the measurement variables from the weather station, as well as their resolution and accuracy. In the following, the measurement techniques of the variables

used in this thesis, precipitation, air temperature and vapour pressure deficit, are explained. The weather station measures precipitation with a 9.31-cm diameter rain gauge. Gold pins measure every drop of rain, whereby the flared hole forms a drop of a known size, and Atmos 41 can calculate the water volume. The air temperature is measured by a thermistor in the centre of the anemometer. The sensor is not protected, but since the weather station also measures wind and solar radiation, it includes this in the calculation. Vapour pressure and vapour pressure deficit (VPD) is calculated by the variables relative humidity and temperature, which are measured by a sensor [23].

In July, there was a failure of precipitation measurements due to foliage in the measuring vessel. This failure is not important for this study, since no ERT survey took place during this period. For the overview diagrams, the precipitation failure was supplemented with precipitation data from the weather station in Davos Dorf for the months May and June. The operators of this weather station are Meteo Swiss and the WSL Institute for Snow and Avalanche Research SLF.

**Table 2:** Overview of the technical specification from the Sensors Teros 12 and 21 [24, 25].

| Sensor   | Measured Variable                 | Resolution                           | Accuracy   |
|----------|-----------------------------------|--------------------------------------|--|
| Teros 12 | Volumetric Water Content (VWC)    | 0.001 m <sup>3</sup> /m <sup>3</sup> | ± 0.03 m <sup>3</sup> /m <sup>3</sup>                  |
| Teros 12 | Temperature                       | 0.1 °C                               | ± 0.5 °C from 40 to 0 °C,<br>± 0.3 °C from 0 to +60 °C |
| Teros 12 | Bulk Electrical Conductivity (EC) | 0.001 dS/m                           | ± 5 % + 0.01 dS/m from 0–10 dS/m                       |
| Teros 21 | Soil Water Potential              | 0.1 kPa                              | ± 10 % of reading + 2 kPa, from 9 to 100 kPa           |
| Teros 21 | Temperature                       | 0.1 °C                               | ±1 °C  |

**Table 3:** Overview of the technical specification from the All-in-One Weather Station Atmos 41 [23].

| Measured Variable | Resolution         | Accuracy  |
|-------------------|--------------------|---|
| Solar Radiation   | 1 W/m <sup>2</sup> | ± 5 % of measurement typical                              |
| Precipitation     | 0.017 mm           | ± 5 % of measurement from 0 to 50 mm/h                    |
| Vapour Pressure   | 0.01 kPa           | Varies with temperature and humidity, see [23]            |
| Relative Humidity | 0.1 % RH           | Varies with temperature and humidity, see [23]            |
| Air Temperature   | 0.1 °C             | ± 0.6 °C  |
| Humidity Sensor   |                    |   |
| Temperature       | 0.1 °C             | ±1.0 °C   |
| Barometric        |                    |   |
| Pressure          | 0.01 kPa           | ± 0.05 kPa at 25 °C                                       |
| Horizontal        |                    |   |
| Wind Speed        | 0.01 m/s           | The greater of 0.3 m/s or 3 % of measurement              |
| Wind Gust         | 0.01 m/s           | The greater of 0.3 m/s or 3 % of measurement              |
| Wind Direction    | 1°                 | ± 5°  |
| Tilt              | 0.1°               | ± 5°  |
| Lightning Strike  | 1 strike           | Variable with distance, >25 % detection at <10 km typical |
| Lightning Average |                    |   |
| Distance          | 3 km               | Variable  |

#### 2.2.4. Electrical Resistivity Tomography (ERT)

Electrical Resistivity Tomography (ERT) is a near-surface geophysical method to investigate processes in the subsurface of the ground. The purpose of electrical resistivity surveys is to determine the spatial resistivity distribution of the soil. For this an artificial electrical potential field gets generated and measured. The electrical resistivity is measured along a profile line with a specific number of electrodes on the soil surface. The electrodes are used both for injection of the current  $I$  (Amperes) in the topsoil and measurement of the voltage  $V$  (Volts) [19]. Considering four

electrodes, two are for source and sink of the current and two for detecting the potential. The resistivity of the ground can be determined, as the introduced current, the potential between the electrodes and the electrode configuration are known. The determined resistivity is referred to as "apparent resistivity". Using fixed electrode spacing, lateral resistivity differences along the profile can be determined up to an approximately constant investigation depth, called "pseudo-depth". Thereby, the investigation depth is determined by the electrode spacing, the smaller the spacing the smaller the range into the depth, which is related to the spatial sensitivity of the measurement [19].

In this thesis, two profile lines were placed alongside the slope at the sites Well001 and Poor\_meas001. Each profile line consists of 48 electrodes with a spacing of 0.25 m, thus the length of the profile line was 11.75 m. The electrode spacing was chosen in order to obtain a small-scale resolution of the hydrological processes and still cover the entire landslide zone of potential shallow landslides. For the ERT data survey the "Syscal Pro electrode system" from IRIS Instruments was used. Some basic instrument settings were for all surveys the same. The variable stack number, which limits the number of measurements, was set to a minimum of 3 and a maximum of 6. The quality factor  $Q_{max}$  was set to 1.

For all surveys two different electrical resistivity arrays were used, the dipole-dipole array and the Wenner-Schlumberger array. The two arrays have different configurations of the potential electrode and the current electrode. Furthermore, the arrays differ regarding resolution, sensitivity and depth of investigation. For example, the dipole-dipole array has a high sensitivity of the vertical structures and a rather low sensitivity of the horizontal structure. Whereas the Wenner-Schlumberger array has for both vertical and horizontal structure a similar medium sensitivity. The dipole-dipole array reaches greater depths than the Wenner-Schlumberger array and has a higher horizontal data coverage. Only for the signal strength does the Wenner-Schlumberger array obtain better values [29]. The arrays differ in terms of the number of measured values and the duration of the measurement. A measurement with the dipole-dipole array consisted of 1900 measurement values and lasted about 15 minutes. A measurement with the Wenner-Schlumberger array consisted of 520 measurements and took about 40 minutes. In this thesis no reciprocal measurement was carried out verifying the data.

Two ERT survey series were performed on both sites Well001 and Poor\_meas001, a longer one (9 days) in July and shorter one (3 days) in August. The ERT survey in July started at 05.07. until the 24.07.2022. The survey in August was run between the 18.08. until the 22.08.2022. Overall, 47 data sets were generated, one data set from the 19.08.2022 site Poor\_meas001 with the Wenner-Schlumberger array is invalid. It was attempted to run the measurements around the same time, which was between 09.30 a.m - 14.00 p.m. For the further calculations in this thesis, it was assumed that the measurements at Well001 took place at 10.30 am and the measurements at Poor\_meas001 at 12.30 pm.

### **2.2.5. Additional Data**

Some of the used data was generated before this thesis as part of the "WaWaRu" project. Before the installation of the data loggers and sensors, soil profiles were made and documented at each site. Previously, soil samples were taken from the Lücherwald and during this thesis a sieve and areometer analysis of the samples was made, to determine the grain size. The classification of the soils was conducted according to USCS nomenclature [31]. In addition, a comprehensive DBH and species survey of the trees in the stand was made. Thereby, the regeneration in the stand was also recorded. This data was used in this thesis to get an overview of the existing trees at the ERT study sites. The total snow depth data in figure 11 was provided from the weather station in Monstein Dorf, which is operated by Meteo Swiss.



## 2.3. Data Analysis

### 2.3.1. Vegetation Data

The aim of processing the vegetation data was to characterise the sites particularly regarding the development of the distinguished vegetation layers. Thus, from each site, an average of the values from the six recording areas was calculated for each category. From these average values, corresponding graphs were created. Furthermore, the respective ecological indicator for each species according to Landolt & al. 2010 were provided to biologically and ecologically distinguish between the sites [21]. The species were also classified according to the NaiS indicator values [13].

As no detailed analysis has been performed, it is not possible to make a definitive statement about the range of rooting zone at the sites. However, a rough assumption is useful for the interpretation of the ERT tomograms. According to the Root Atlas of Central European Forest Trees and Shrubs, spruce roots on slopes reach depths of about 1.20. It is known that spruces can develop plate-shaped root systems with sink roots [20]. Thus, in this thesis a maximum root depth of 1.20 m was assumed.

### 2.3.2. Logger and Sensor Data

The measurement series of the "WaWaRu" project started in August 2021, within this thesis the data from 01.02. until the 24.08.2022 are considered. From the 01.02. to the 17.06.2022 the measurement interval was set to 30 minutes. On the 17.06.2022 the measurement interval was set to measurements every minute and the weather station to every five minutes, to get a higher resolution. For the data analysis, all data were used, despite different measurement intervals, as the differences are negligible.

The data analysis was carried out with the software R Studio, version 2022.2.2.485 [28]. In this thesis the focus lied especially on the variables volumetric water content (VWC) and soil temperature from the sensor Teros 12. Soil water potential and bulk electrical conductivity (EC) were not further discussed. In this respect the variables precipitation, air temperature and vapour pressure deficit (VPD) were considered from the weather station. For the analysis of the named variables, mainly graphical representations over specific time periods were generated, with the focus on the ERT survey periods. In some cases, the data were presented as raw data. However, when longer time periods were considered, the data were smoothed to daily average. In contrast, precipitation was calculated to the common daily and hourly values, but was also used as raw data. In some analyses, the focus was set only on the ERT survey sites Well001 and Poor\_meas001.

The focus of the analysis of both VWC and soil temperature variables was to compare the values between the sites. Descriptive and inferential statistics were performed, whereby a Kruskal-Wallis rank sum test was applied to test whether there is a significant difference between the sites. The Kruskal-Wallis test for independent samples tests, if the central tendencies of several independent samples differ. It is a robust test and is used when the normal distribution is not fulfilled. Since the Kruskal-Wallis test only checks whether there is a central tendency, which means, if there is a significant difference between the sites, a post hoc test was also applied. For this purpose, a Dunn test was performed using the p-value adjustment method "Holm". It makes a comparison between the groups and tests which site shows a significant difference [30] The used functions in R Studio were *kruskal.test()* and *Dunn.Test()*.

### 2.3.3. Electrical Resistivity Data

Soil temperature variations during the measurement period have a significant influence on the electrical resistivity, therefore it is necessary to correct the apparent resistivity values to a standard temperature. Without a temperature adjustment, there is a risk for misinterpretation of changes in electrical resistivity [17]. In this thesis, there were no noticeably large soil temperature variations

during the measurement period. The temperature variations during the ERT survey period in July were 2.2 °C for site Well001 and 2.9 °C for site Poor\_meas001. During the ERT survey period in August, the temperature variations for Well001 were 1.2 °C and for the Poor\_meas001 site 1.0 °C. Figure 3 gives an overview of soil temperature curves at the two sites. Hence a rather simple

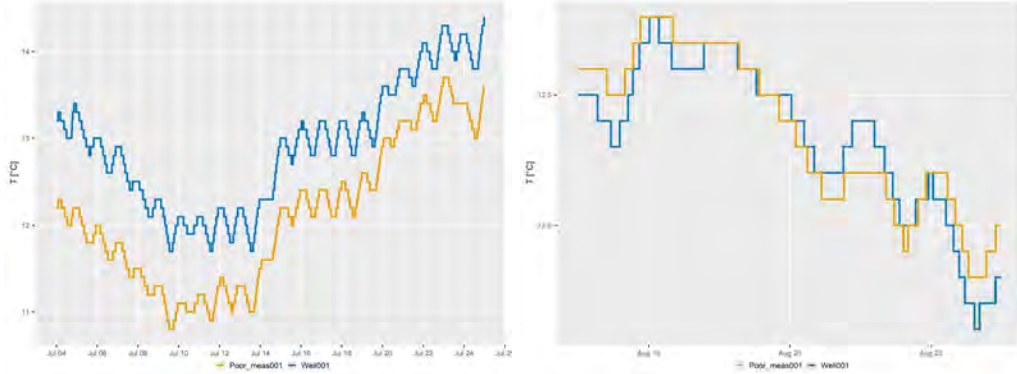


**Figure 3:** Soil Temperature values from the sensor Teros 12 at depth of 30 cm during the ERT survey period. On the left for July and on the right side for August.

temperature correction approach was chosen. The exponential equation from Corwin and Lesch (2005) [9] was used to calculate the temperature conversion factor  $f_T$ . This approach corrects the resistivity data to the standard temperature of 25 °C.

$$f_T = 0.4470 + 1.4034^{-T/26.815} \quad (1)$$

The temperature correction was applied to the apparent resistivity data before any further processing of the data. For each ERT data set a temperature conversion factor  $f_T$  was calculated. As input for variable T in the equation 1, soil temperature values from the sensor Teros 12 at a depth of 30 cm were used. The temperature values were selected for each date at the same time. For the site Well001 always at 10:30 a.m. and for the site Poor\_meas001 at 12:30 p.m. Multiplying the apparent resistivity of each data set with the temperature conversion factor gives the temperature corrected resistivity. The differences of the apparent resistivities before and after the temperature correction were not analysed in depth. However, random samples did not indicate any obvious differences between the data sets.

Electrical resistivity measurements require the use of an inverse method to obtain a resistivity model. The aim of the methods is to find the best distribution of geoelectrical parameters, which is consistent with the observed measurements. This involves minimising the misfit between the four electrode measurements and response predicted by a geoelectrical model. Due to the non-linear nature of the problem, the inversion is performed iterative until the misfit between the predicted response and the measurements lies between a given tolerance [6].

The inversion of the measured apparent resistivity data was done using the software ResIPy, which is an open-source software for complex geoelectrical inversion and modelling [6]. With the software ResIPy several inversions were modelled out of the apparent resistivity data. Inversions of the individual measurements as well as time-lapse inversions of the two surveys were processed. The time-lapse inversions were only used for the difference analysis. The analysis of the modelled resistivities was performed with the individual inversions. The inversions were processed for all apparent resistivity data sets the same, with minor differences between the dipole-dipole and Wenner-Schlumberger arrays.

The inversion parameters looked as follows: As a first step, the topography of the sites was applied to the data sets. Both sites had an individual terrain structure, which was created from

GPS points and accurate profile recording in the field. For this purpose, the top and bottom points of the ERT profile line were recorded in the field with a GPS. The rest of the profile was manually noted, with particular attention paid to steep steps or roots. The profile is read in as z-axis into the application, with the elevation values being distributed accordingly to the 48 electrodes. In the pre-processing, the apparent resistivity data was filtered to remove erroneous measurements. For the dipole-dipole array data, the stacking error was set to 0.5 %, meaning all data points with an error greater than 0.5 % were filtered out. For the Wenner-Schlumberger array data, the filter was set at 1 % due to the smaller number of data points.

In the next step, a triangular mesh was designed for both sites. A triangular mesh allows the application to handle more complicated topographies. In addition, with a mesh the accuracy of the inversion can be controlled, as the application otherwise creates a default mesh. For the generation of a mesh, the characteristic length and growth factor have to be defined. The characteristic length is associated with each electrode node, where a small length results in a finer mesh. On the contrary, the growth factor determines the increase of the mesh with depth. It is important not to choose a too fine mesh when the sensitivity is low, as this will cause more noise. Therefore, a finer mesh was created for the dipole-dipole arrays (see figure 4) than for the Wenner-Schlumberger array (see figure 5), due to the smaller number of data points [6].

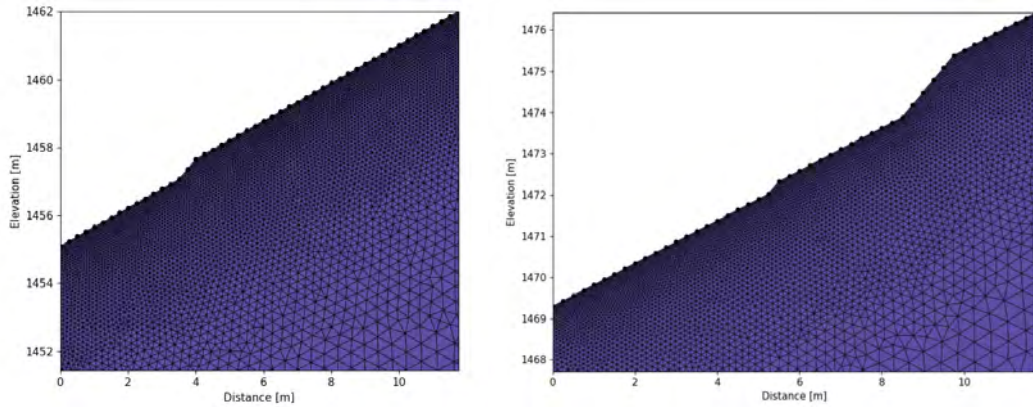


**Figure 4:** Triangular meshes as input parameter for the inversion in ResIpy. The meshes were constructed for dipole-dipole arrays on the left side is the profile from Well001 and on the right side Poor\_meas001.

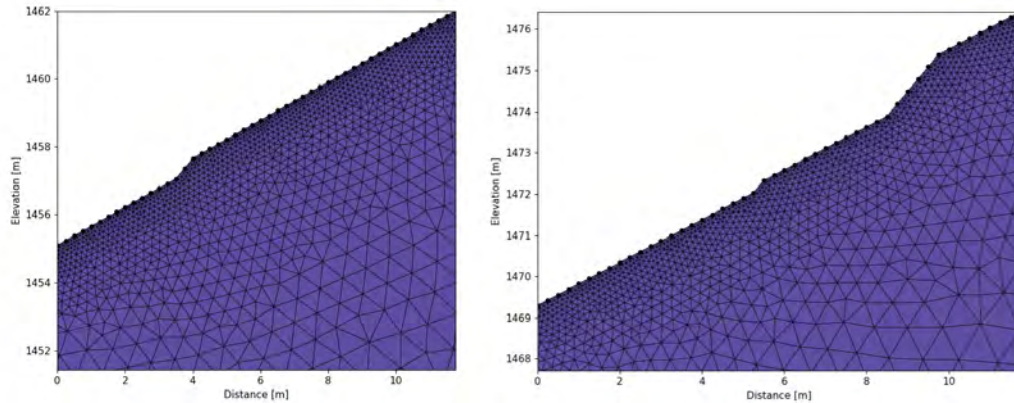


**Figure 5:** Triangular meshes as input parameter for the inversion in ResIpy. The meshes were constructed for Wenner-Schlumberger arrays on the left side is the profile from Well001 and on the right side Poor\_meas001.

For the inversion settings, everything was left at the default settings (see figure 6). The "inversion type" was a regularised inversion with linear filtering. The "target decrease" was set to 0, but it would specify the relative reduction of misfit in each iteration. It has the goal to approve the convergence, because of a slower progression of the inversion. The "data type" was logarithmic and the "regularisation mode" was set to normal regularisation. The "value for tolerance" is 1.0, which defines the desired misfit. The maximum number of iterations was set to 10. "A\_wtg" and "b\_wtg" values define the noise level, where the typically values for surface data, "a\_wtg" is about 0.01 ohms and "b\_wtg" is about 0.02 (roughly equivalent to 2 % error). The "minimum apparent resistivity" is set to  $-10e10$  and the maximum value to  $10e10$ , all other values in the data will not be considered.

In the advanced settings, only the factor "update the weights" was changed to the recommended setting "update the weights". The other settings were left at the default settings. "Number of parallel threads" was set to 16, which defines the number of logical processors that are used during parallel operations, for example time-lapse inversions. The box "crop below mesh fine region was checked", so the mesh below fine/coarse boundary depth gets cropped out. The value for "res\_matrix" is set to sensitivity matrix, which is required for the converged solution. The x, y patch size defines the parameter block size in x and z direction. The default number is 1, a higher value would shorten the computation time. The value for "alpha\_aniso" is the smoothing factor, here set to 1 for normal regularisation. If the factor would be higher than one, it results smoother horizontal models [6]. No specific post-processing of the inversion was done, only the verification that the normalised inversion error did not exceed the recommended threshold  $\pm 3$  %.

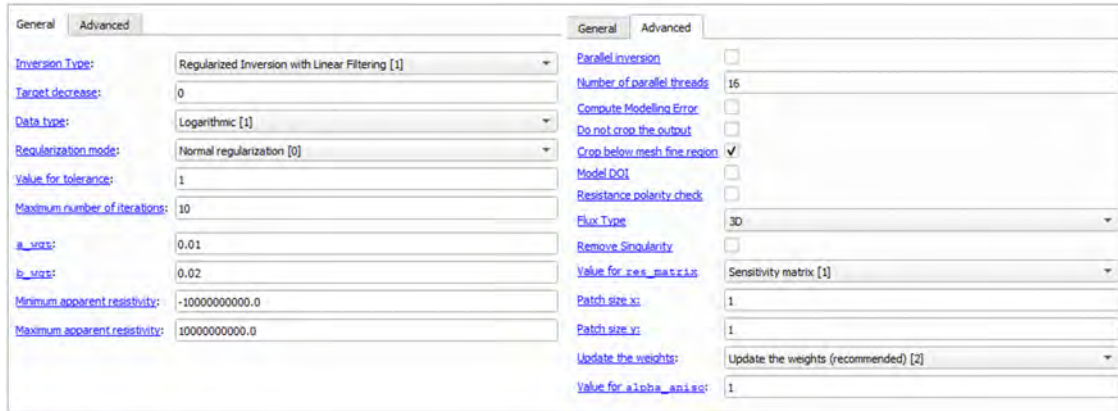


**Figure 6:** Overview of the used general and advanced inversion settings in the software ResIpy.

In this thesis, a descriptive comparison of the electrical resistivity tomograms was made, as well as an analysis of the modelled resistivity values. The analysis of the modelled resistivity values was mainly carried out with the individual inversion values. Thereby, all data of the performed ERT surveys were considered. The electrical resistivity tomograms comparison was made with the individual models and for the difference analysis the time-lapse inversion models were taken. The focus was set on the precipitation events, so from the July survey only the last four measurements (19.07. - 24.07.2022) were used. Moreover, the focus of the graphical analysis was mainly on the electrical resistivity tomograms with the dipole-dipole arrays due to the deeper range. Nevertheless, a comparison of the results from both arrays was made.

For the analysis of the modelled electrical resistivities, the values were compared using boxplots and histogram diagrams. To allow a clearer comparison, the axes with electrical resistivity values in the diagrams were limited to a maximum value of 15'000 ohm m. Based on the data comparison, it was assumed that the values above 15'000 ohm m were outliers or measurement errors. The aim of the analysis of the modelled resistivities was to find out, whether there is a significant difference between the two sites Well001 and Poor\_meas001. For this purpose, a Wilcoxon signed-rank test was performed for dependent samples, which tests if the central tendencies of two dependent samples are different. It is a robust test and is used when the normal distribution is not fulfilled. [30]. The result of the test was directly integrated into the boxplot using the standard significance representation with asterisks. The function used for the statistical test in R Studio was `geom_signif()` with `test=wilcox.test`.

The dependency of the modelled electrical resistivities and the VWC values was tested with a scatterplot. For this purpose, the specific values were plotted against each other. The VWC for all depth values were filtered out for the corresponding date and time of the ERT measurement. The corresponding electrical resistivity values were filtered out according to the following criteria: The modelled resistivity values are structured according to x and z values, which define the exact location of the resistivity measurement in the ground. The needed x-value was defined by the location of the VWC sensors in the ERT profile. In the x-direction the calculation was done with an accuracy of  $\pm 0.1$  m. From the resulting list, the resistivity values for the corresponding depths of the sensors at 30 and 50 cm had to be further extracted. It was assumed that the top z-value determines the earth's surface. In z-direction, it was calculated with an accuracy of  $\pm 0.05$  m. Table 4 gives an overview of the x- and z-directions to extract the corresponding electrical resistivity values. The data points of the depth 10 cm have not been used. Based on the length of the electrodes, it was assumed that the current field was not yet completely established at the depth of 10 cm. A smoothed conditional regression line has been added to the comparison of the electrical resistivity and the VWC values. The method of LOESS (locally estimated scatterplot smoothing) was used with a span of 0.9.

**Table 4:** Calculated values in x- and z-direction to extract the corresponding electrical resistivity values at the different VWC sensor depths.

| Site         | x [m] | z [m] (30 cm) | z [m] (50 cm) |
|--------------|-------|---------------|---------------|
| Well001      | 7.75  | 1459.46       | 1459.26       |
| Poor_meas001 | 7.5   | 1473.07       | 1472.87       |

## 3. Results

### 3.1. Vegetation Recording

In this chapter, the results of the vegetation recording are presented, whereby the focus lies on the first (13.05.2022) and last (05.08.2022) survey dates. The figures of the other recording dates can be found in the appendix A.1. The development of the herb layer over the recording period is presented. The photo documentation of the first and last vegetation recording is provided in the appendix A.3, as well as the list of species from the herb layer A.2.

Figure 7 shows the vegetation recording at the first survey day at 13.05.2022. The figure is divided in the different layers, where the coverage rate in percentage is depicted with stackbars in the recording categories. The soil layer achieved nearly 100 % coverage at each site. Rare stones were recorded at all sites. The proportion of bare soil was lower at Poor001 and Poor002, as the litter layer was more extensive. The rate of roots was higher at the "poor" structured forest stands than at the "well" structured forest stands, where only at Well002 roots were recorded. The rate of moss was strikingly higher at the "well" sites. On the "poor" sites a higher litter rate was recorded, although Well001 also had a high rate of litter. The proportion of deadwood had no distinct tendency comparing the sites. At the start of the vegetation survey, the herb layer was still at an early stage of the vegetation period, which can be seen in the images in appendix A.3. Regarding the development of the herb layer, a clear difference between the "well" and "poor" structured forest stands could be observed. At the "poor" sites, only single plants were present in the herb layer. *Vaccinium vitis-idaea* was mainly present at Well002 and sporadically at Well001 and Poor002. However, *Vaccinium myrtillus*, was most present at Meteo and rarely at the other sites. *Sorbus aucuparia* was mostly found at the "well" sites, but also rarely at the "poor" sites. *Picea Abies* as tree regeneration was only present at the "well" sites, whereas Larch regeneration was only present at Meteo. The category herb was the most distinct category at the "well" site, as all remaining herbaceous plants are combined there. At the start of recording, Well002 had the least developed herb layer with approximately 12 %, ahead of the "well" sites and Well001 had the most developed with approximately 25 %. The "poor" sites had all an equally poorly developed herb layer around 1 %. The shrub layer was not strongly developed at all sites under 10 %, only Meteo had one *Lonicera alpigena* individuum. Otherwise, there was some *Picea Abies* regeneration at the "well" sites, which belonged to the shrub layer. The "poor" sites had no shrub layer. According to the tree layer, it is clearly visible that the "poor" sites had a higher canopy cover than the "well" sites. There was no tree layer at site Meteo. Well002 with almost 25 % showed a higher canopy cover than Well001 with lower than 12 %. The "poor" sites had a canopy cover range from 62 to 76 %.



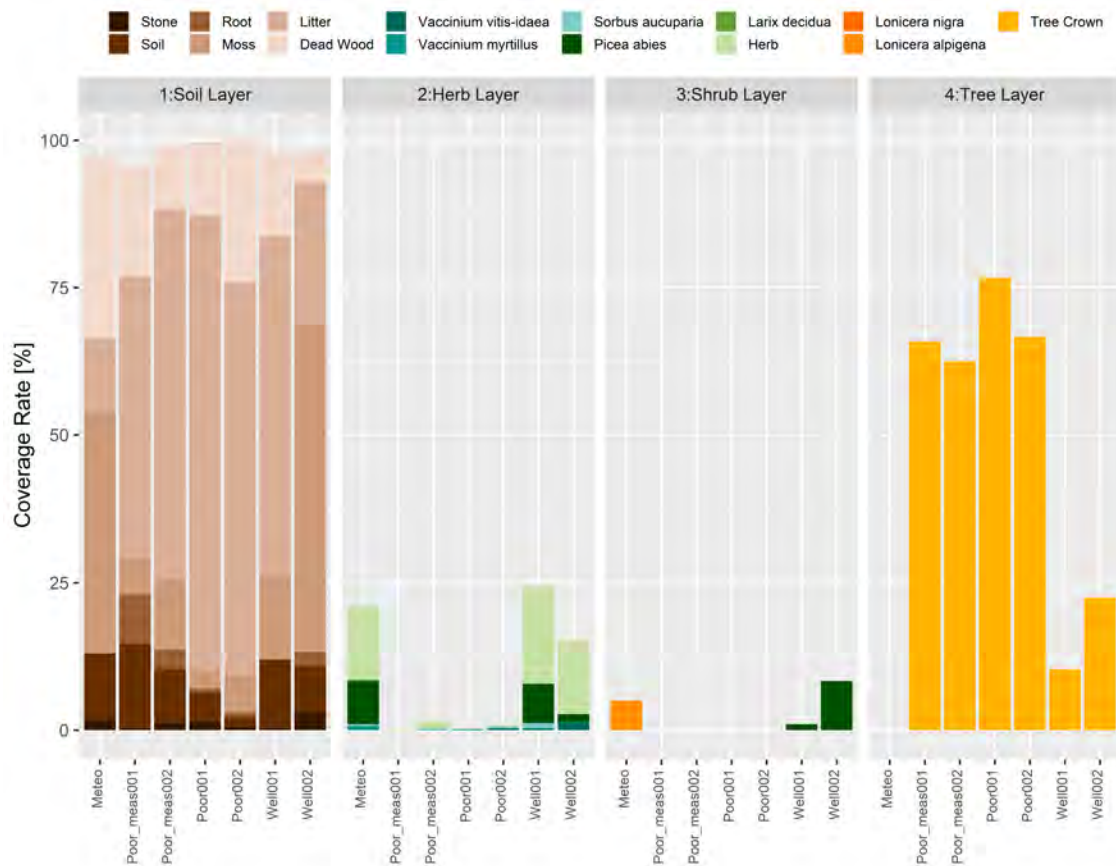


**Figure 7:** Coverage rates in percentage from all vegetation layers (soil, herb, shrub and tree) at the first day of recording 13.05.2022. The stackbars are divided in the shown categories. The brown shades described the categories in the soil layer, the blue-green shades the categories in the herb layer, the red shades the categories in the shrub layer and yellow the canopy cover in the tree layer.

At the last day of recording at 05.08.2022 the coverage rate of soil and tree layer did not change compared to the first day of recording (see figure 8). However, the coverage rates of the herb and shrub layers had further developed. It is clear that the herb layer in particular increased at the "well" sites, whereby Meteo and Well001 achieved almost 50 % coverage and Well002 still had the lowest coverage of the "well" sites. Poor\_meas001 developed a small herb layer during the growing season, whereas at the other "poor" sites, the herb coverage was only slightly higher approximately under 5 %. At all sites, mainly the category herb increased, as well as both *Vaccinium* species and *Sorbus aucuparia*, to a smaller extent. The categories *Larix decidua* and *Picea abies* did not change. There were no major changes in the shrub layer. At the Meteo site, one individual of *Lonicera nigra* increased in size and thus overlapped with the recording area.

The development of the herb layer showed a steep growth during the recording period until 24.06.2022, especially at the "well" sites and to a smaller extent at the "poor" sites (see figure 9). However, from this date on until 05.08.2022 the growth levelled off and did not change any more.



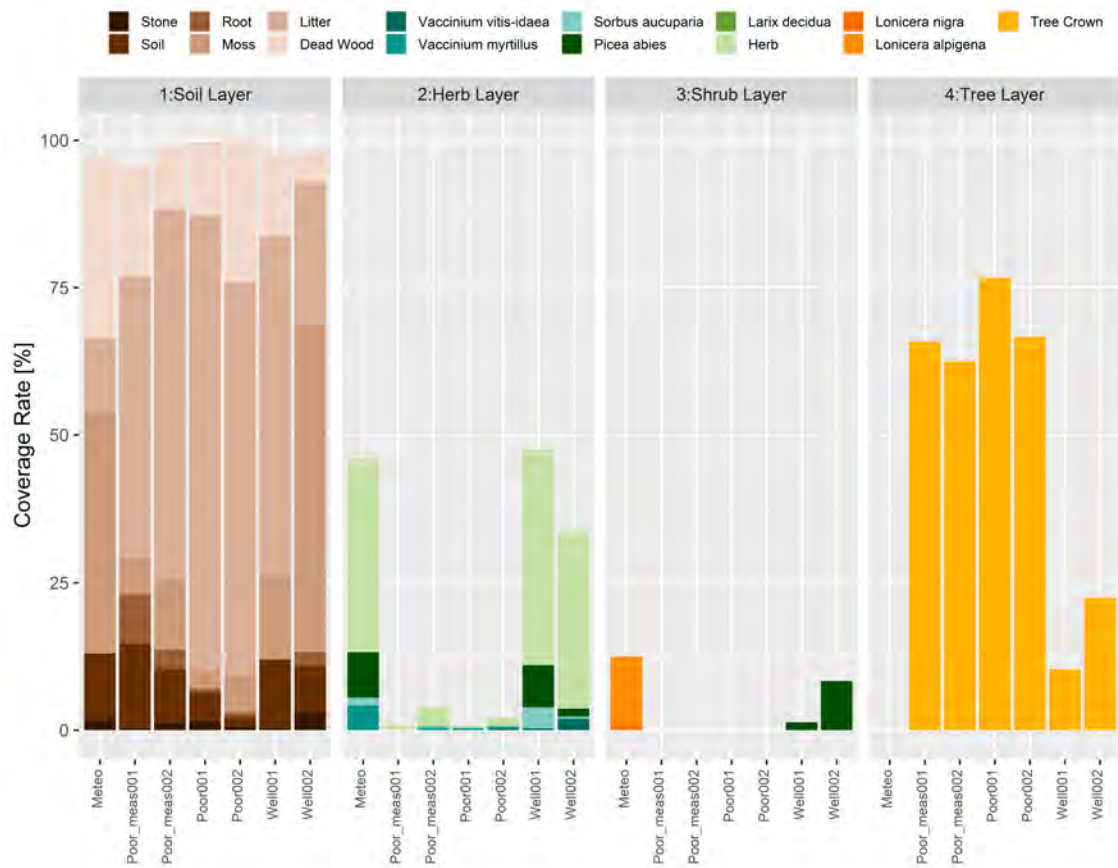


**Figure 8:** Coverage rates in percentage from all vegetation layers (soil, herb, shrub and tree) at the last day of recording 05.08.2022. The stackbars are divided in the shown categories. The brown shades described the categories in the soil layer, the blue-green shades the categories in the herb layer, the red shades the categories in the shrub layer and yellow the canopy cover in the tree layer.

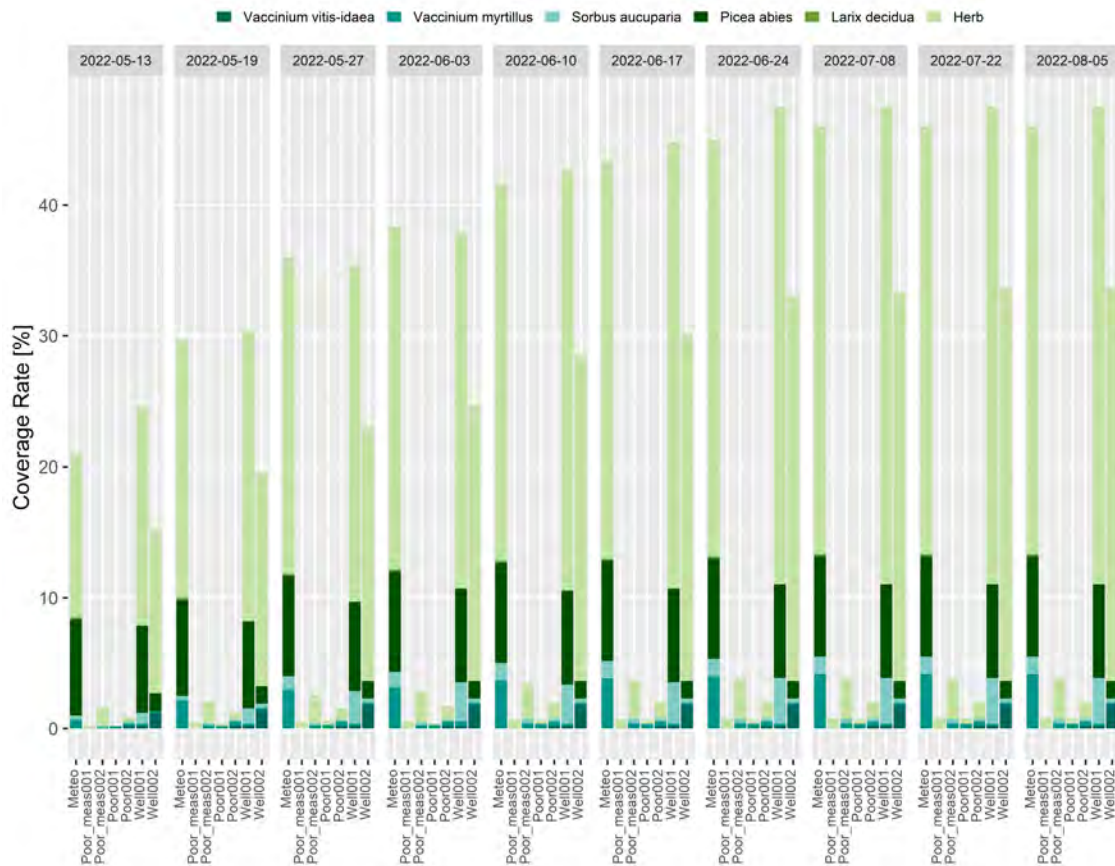


**Figure 9:** Development of the coverage rate in percentage from the herb layer over the entire recording period. The stackbars are divided in the shown categories. The blue-green shades describe the categories in the herb layer

The following section gives a summary of the ecological indicator values of the recorded herbaceous plants (see appendix A.2). Regarding soil moisture, mainly species were present, which indicate humidity and alternately wetness or dryness. Furthermore, species ranging from strong acidity indicators to neutrality indicators were present, but no lime indicators. Most species were moderately nutrient-demanding, only the occasional *Urtica dioica* or *Rubus fruticosus* were strong nutrient-demanding. There were mainly shade and semi-shade preferring plants, only few light preferring plants occurred on the "well" sites. The majority of the present plants preferred cool to medium-warm temperatures. The continental numbers indicated locations from suboceanic to intermediate and subcontinental. It could be observed that the few herbaceous plant species on the "poor" sites were mostly acidity indicators. In contrast, on the "well" sites were many humidity indicating herbaceous species. Basically, the vegetation recording confirmed the forest type 55 VM mentioned in the methods 2.1, although the forest site could also correspond to type 55 *Veronica latifoliae-Piceetum*.

### 3.2. Soil Analysis

In the following chapter, the results of the sieve analysis of the soil samples are presented, as well as a short summary of the soil profiles from site Well001 and Poor\_meas001. The grain size distribution curve is shown in figure 10, which is the result of the sieve analysis from the soil samples of Lücherwald. According to the Swiss standard for geotechnical parameters, the soil type determination corresponded to a well graded gravel with silt and sand (GW-GM), whereby

the last 15 % from 85 % to 100 % no longer corresponded to the norm curve. In the grain size distribution of Lücherwald, the curve had a concave shape starting at 80 %, as there were fewer grains with diameters over 20 mm [31]. Photos of the soil profiles from Well001 and Poor\_meas001 are attached in the appendix B.1.

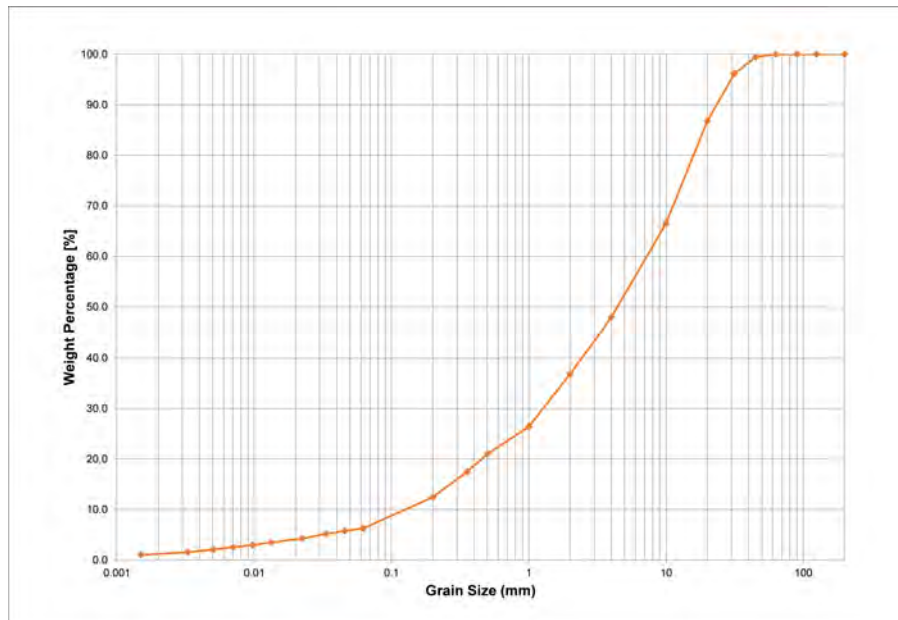


**Figure 10:** Grain size distribution curve as result of the soil sample analysis from Lücherwald. The curve shows the weight percent of each specific grain size.

In order to give an impression of the soil profiles at site Well001 and Poor\_meas001, these are presented in table 5. Both sites have mull as hummus form. At Well001, the soil changes from the humic terrestrial topsoil horizon Ah directly to the initial terrestrial topsoil horizon Ci. In contrast, at Poor\_meas001 a humic topsoil horizon Bh is in between.

**Table 5:** Overview of the soil horizons of the sites Well001 and Poor\_meas001. The soil profiles were done during the sensor installation.

| Site         | Soil Horizons  |
|--------------|--|
| Well001      | L - Of (5 cm) - Ah (16 cm) - Ci (33 cm) - Cii (60 cm)                                |
| Poor_meas001 | L (1 cm) - Of (10 cm) - Ah (15 cm) - Ae (26 cm) - Bh (28) - Ci (30 cm) - Cii (70 cm) |

### 3.3. Logger and Weather Station Data

#### 3.3.1. Overview of the Study Period

In this section the investigated results of the weather and logger data in the Lücherwald study area are presented. The focus of the weather data lies on precipitation, air temperature and vapour pressure deficit. The focus of the logger data lies on VWC and soil temperatures values. Especially data trends during the study period are presented, as well as the analysis of value distributions.

Figure 11 provides an overview of the weather conditions and the corresponding VWC values at all sites during the study period. In the figure the effect of weather conditions on the VWC in the soil is illustrated. The purple highlighted areas indicate events, which were interesting to study in depth. In general, it is clearly visible that the VWC in 10 cm depth showed higher variability between the sites. 30 and 50 cm run more similar and with smaller differences between the sites.

Only sensor Poor\_meas001 run shallower at both depths and showed less reactions to precipitation events. At 50 cm, the values of all sites showed a large decrease at mid May, except Meteo and Well001 remained the same height. Poor001 had distinctly lower values at 10 cm depth over the entire study period and showed nearly no reaction to precipitation events. In the other depths the site showed less low values compared to the other sites. Over the entire study period and at all depths, Meteo had the highest VWC values. At the 10 cm sensor the other sites partly overlapped and run less similar than at the other depths. Well001 showed lower VWC values at 10 cm than at 30 and 50 cm, where it showed the highest values next to Meteo. Well002 showed high VWC values at 10 cm and rather low values at the other depths. In comparison, the "well" sites at 10 cm showed less large-scale variability than the "poor" sites, especially Poor002 and Poor\_meas001.

Snowmelt in mid-march is shown with the first highlighted area. The total snow depth decreased and the temperatures increased. Thereby, it is clearly visible, how VWC values at all depth strongly increased. The VWC values at 30 and 50 cm reacted with a slight delay according to infiltration. For the VWC values at 10 cm, Meteo showed the strongest increase with the highest peak at almost  $0.4 \text{ m}^3/\text{m}^3$ . In comparison, Poor\_meas001 showed a delayed and flat increase. Poor\_meas002 and Poor002 both showed steep increases in VWC, with Poor002 reaching a higher peak at almost  $0.3 \text{ m}^3/\text{m}^3$ . Poor001 showed almost no response to snowmelt and showed distinctly lower values between  $0.05$  and  $0.1 \text{ m}^3/\text{m}^3$  than the other sites. Well001 and Well002 both showed increases, but not as high as the "poor" sites. Well002 showed higher values than Well001 even before the snowmelt. The VWC values at 30 cm had similar increases, except for Poor\_meas001, which showed almost no response. Well001 had the largest increase, reaching almost  $0.25 \text{ m}^3/\text{m}^3$ , where the peak at 10 cm was lower than  $0.2 \text{ m}^3/\text{m}^3$ . Nearly all VWC values at 50 cm showed an increase, but not as large as at the other depths. Meteo, Poor\_meas002 and Well001 were close to each other, with Poor\_meas002 showing the largest increase. At 50 cm Poor001 did not have the lowest values in comparison to the other depths, but still showed only a small reaction.

The second highlight indicates the reaction of the VWC values after a long-lasting precipitation event. At all depths, a clear increase in the VWC value could be observed, as well as a slight delay due to infiltration. A slight delay in the increase due to interception between the "well" and "poor" sites was also visible at all depths. At 10 cm Poor\_meas001 showed the largest increase and Poor\_meas002 the most delayed. Compared to the "well" sites, the "poor" sites showed a larger increase in value. At 30 cm Meteo and Well001 showed the clearest and largest increase. The "poor" sites showed smaller increases, especially Poor\_meas001. Well002 had the lowest VWC values next to Poor001. At 50 cm the situation is similar with smaller and a shallower peaks, whereas Poor\_meas002 showed the largest increase over a longer time period. The values lie closer together with a clear gap between Meteo and Well001 and the "poor" sites as well as Well002.

The third highlight shows a dry period with high temperatures in July, which lasted several days. The sensors at 10 cm showed a clear decrease in VWC values with the exception of Poor001. The decrease was roughly parallel, with Poor\_meas001 showing the largest decrease from  $0.3 \text{ m}^3/\text{m}^3$  to  $0.15 \text{ m}^3/\text{m}^3$ . At depths of 30 and 50 cm, a decrease in VWC could be observed, but to a smaller scale. It is striking that only Meteo and Well001 showed an increase after the first precipitation event. At 30 cm, a response to precipitation can also only be observed at Meteo and Well001, although it was flatter. However, at 50 cm almost no reaction to the first precipitation could be observed.

The first reaction to precipitation, which was visible at all sensors, is highlighted in the fourth purple area. Previously, only Meteo and Well001 showed a clear response to precipitation over several days and the other sites had no increases. At 10 cm, a grouping of the "well" sites at  $0.2 \text{ m}^3/\text{m}^3$  and the "poor" sites with lower values at  $0.15 \text{ m}^3/\text{m}^3$  and lower could be observed, whereby Meteo had much higher values around  $0.3 \text{ m}^3/\text{m}^3$ . At the lower sensors 30 and 50 cm, a gap between Meteo and Well001 and the other sensors was visible.

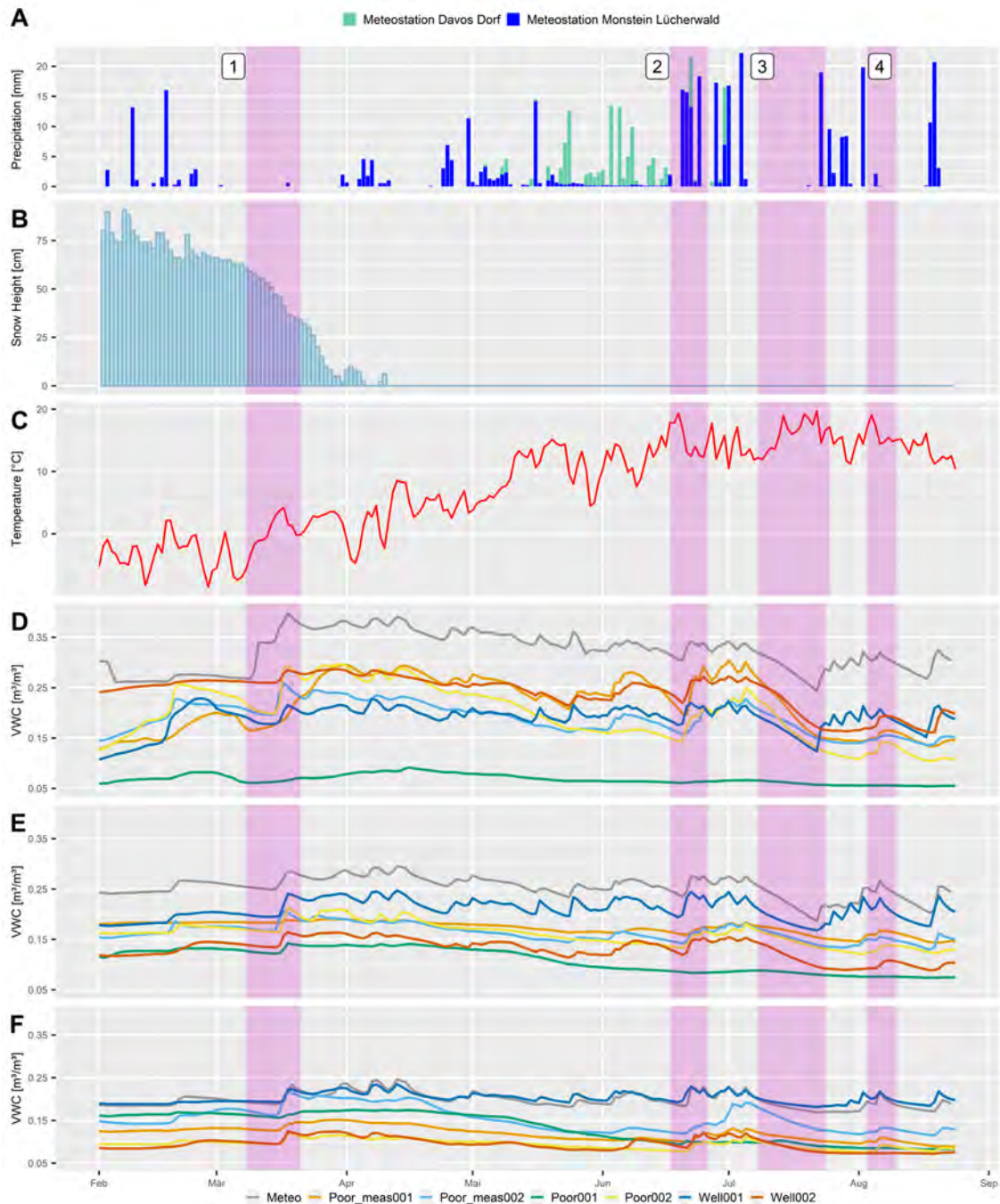


**Figure 11:** Overview of the weather and volumetric water content VWC data during the study period February to August 2022. **A** Daily precipitation from weather station Lücherwald with the supplementing of precipitation from the weather station Davos Dorf in May and June, **B** Total snow depth from weather station Monstein Dorf, **C** Daily average temperature from weather station Lücherwald, **D** VWC at 10 cm from all sites, **E** VWC at 30 cm from all sites, **F** VWC at 50 cm from all sites. The purple highlighted areas indicate interesting events. **1** Start of snowmelt, **2** Long precipitation event, **3** Dry phase, **4** First reaction of all VWC values after dry phase.



### 3.3.2. Volumetric Water Content

The following boxplots give an impression of the VWC values over the study period. This illustration allows to compare between the sites and to identify possible trends. The outputs of the Kruskal-Wallis sum rank test and the Dunn-test as Post-Hoc test can be found in the appendix C.1

The VWC values at 10 cm depth are depicted in figure 12. Particularly striking are the low values of Poor001 compared to the other sites, as well as the much smaller interquartile range. In contrast to the other sites, Meteo had much higher values over  $0.3 \text{ m}^3/\text{m}^3$ . The boxes of the other sites were all in the range of approximately  $0.14 - 0.26 \text{ m}^3/\text{m}^3$ . Poor\_meas001, Poor002 and Well002 showed a wider interquartile range, which means higher value variability. Meteo, Poor\_meas002 and Well001 showed smaller interquartile ranges with a few outliers. The medians of the "poor" sites, with the exception of Poor001, were all close to each other, with Poor002 being slightly lower, below  $0.15 \text{ m}^3/\text{m}^3$ . The medians of the "well" sites were also close to each other near  $0.2 \text{ m}^3/\text{m}^3$ , whereas the "well" sites had higher medians of VWC values than the "poor" sites. The Kruskal-Wallis test showed that the sites differ significantly from each other ( $p\text{-value} < 2.2\text{e-}16$ ). The Dunn test showed that the comparisons of all sites have a p-value of 0 or nearly 0, meaning the VWC of all sites differ significantly from each other.

Figure 13 provides the VWC values of all sites at a depth of 30 cm. Poor001 showed again lower values than the other sites, but not as conspicuously low. The interquartile ranges were similarly wide for all boxes, with the "well" sites being slightly wider. The medians of the "poor" sites, except Poor001, were relatively close to each other around  $0.15 \text{ m}^3/\text{m}^3$ , with Poor002 again showing a lower median. In contrast, the medians of Well001 and Well002 were not close to each other. Well001 had a high median at  $0.2 \text{ m}^3/\text{m}^3$ , but still below Meteo and Well002 showed the lowest median at  $0.11 \text{ m}^3/\text{m}^3$ , next to Poor001. The result of the Kruskal-Wallis test showed a significant difference between the sites ( $p\text{-value} < 2.2\text{e-}16$ ). The Dunn test showed a p-value of 0 for the comparison of each site.

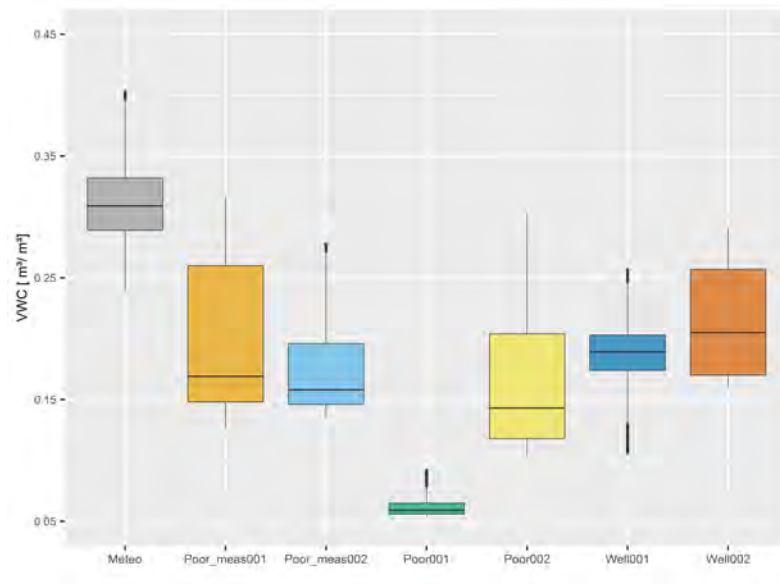


**Figure 12:** Boxplots of the VWC values at 10 cm depth from all sites. All values of the study period from February to August 2022 are included.

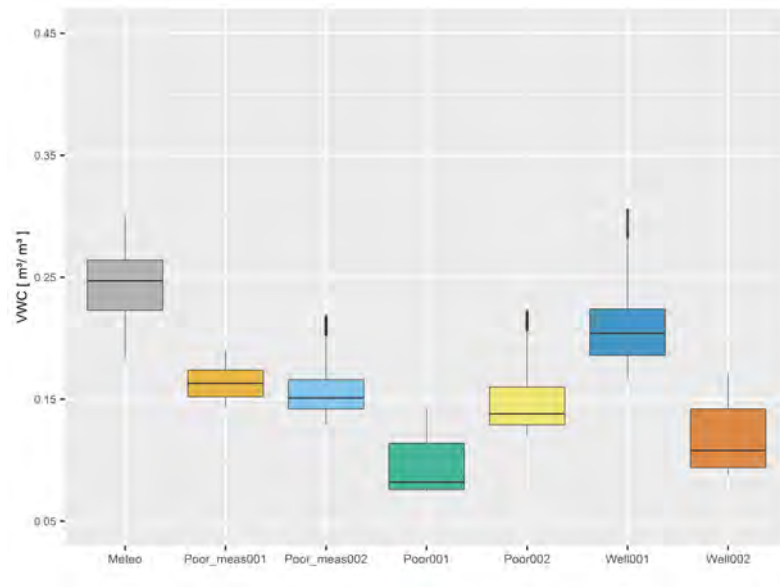


**Figure 13:** Boxplots of the VWC values at 30 cm depth at all sites. All values of the study period from February to August 2022 are included.

The VWC values for depth 50 cm are shown in figure 14. The values for Poor001 at 50 cm no longer differed strikingly from the other sites, only the interquartile range was much wider in comparison. The remaining sites had a similarly narrow interquartile range, which means much lower value variability at this depth. The medians of Meteo and Well001 showed much higher medians than the other sites. The Kruskal-Wallis test also showed a significant result and the Dunn test showed a p-value equal to 0 or nearly 0 for the comparison of each site.

Comparing the VWC values at the different depths showed that the width of the interquartile range decreases with depth, which means higher variability in soil moisture at 10 cm than at 30 and 50 cm. A clear difference between the "poor" and "well" sites was not evident at all depths. At 10 cm the "well" sites and Meteo showed higher medians, whereas for 30 and 50 cm only Meteo and Well001 showed the highest medians. The medians of VWC at Meteo, Poor002 and Well002 decreased with depth, although sometimes only slightly. However, Poor001 and Well001 did not correspond to this trend. Well001 had a higher median in VWC for 30 cm than for 10 cm and Poor001 even increased from high to low.

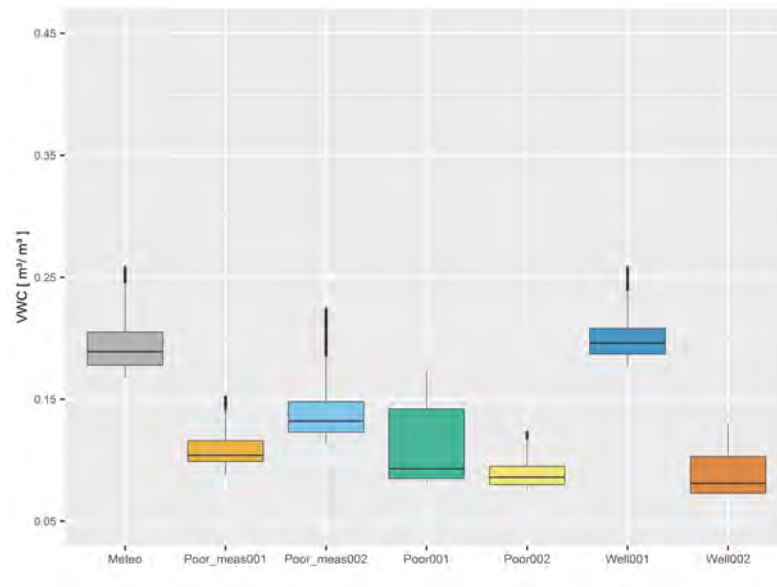


**Figure 14:** Boxplots of the VWC values at 50 cm depth at all sites. All values of the study period from February to August 2022 are included.

### 3.3.3. Soil Temperature

The following boxplots give an impression of the soil temperature values over the study period. This illustration allows comparisons between the sites and possible trends to be identified. The outputs of the Kruskal-Wallis sum rank test and the Dunn-test as Post-Hoc test can be found in the appendix C.1

Figure 15 shows the soil temperatures of all sites at a depth of 10 cm. Noticeable is the wide interquartile range of Poor001 compared to the other sites, indicating a much higher temperature variability. Meteo also showed a wider interquartile range, whereas the other sites had a similar width. All the medians of the soil temperatures lied in a similar range. Both "well" sites showed a higher median over 13 °C than the "poor" sites and Meteo, which were lower than 13 °C. The Kruskal-Wallis test showed that the sites differ significantly from each other ( $p$ -value  $< 2.2e-16$ ). The site comparisons in the Dunn test reached a significant result with  $p$ -values smaller than 0.05.

The distribution of soil temperatures at 30 cm depth appears similar to the temperatures at 10 cm (see figure 16). All sites had similar widths for the interquartile ranges, except Poor001 again was much wider and Meteo was slightly wider. The medians of the "well" sites lied close to each other and were slightly higher than the "poor" sites and Meteo, but all lower than 13 °C. The result of the Kruskal-Wallis test showed that the sites differ significantly from each other. The Dunn test showed a  $p$ -value of 0 or almost 0 for the comparison of all sites.



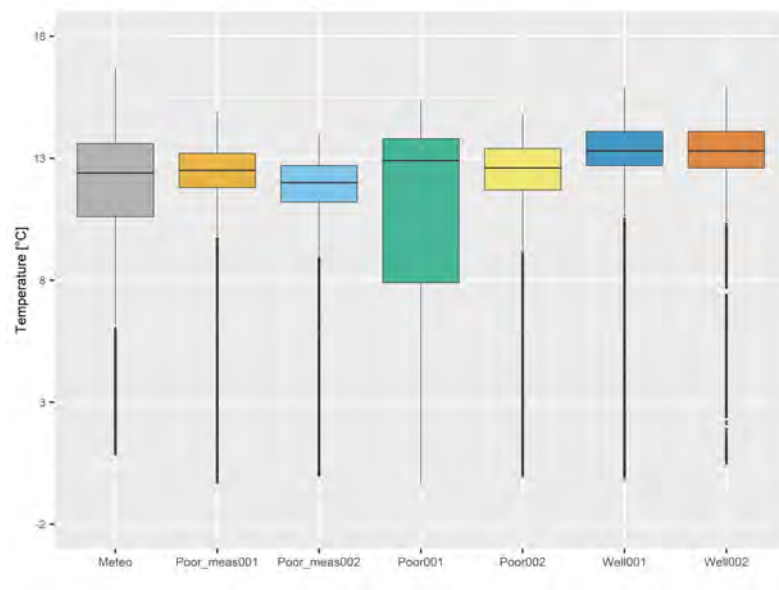


**Figure 15:** Boxplots of the soil temperature values at 10 cm depth from all sites. All values of the study period from February to August 2022 are included.

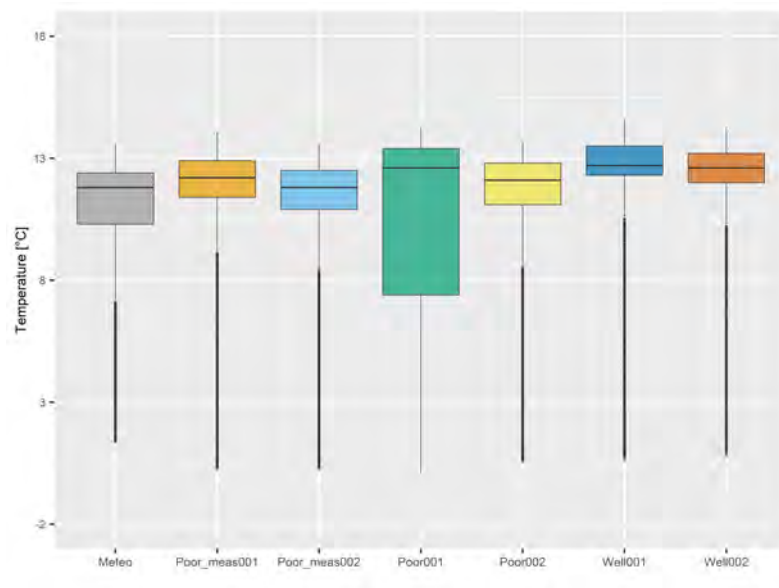


**Figure 16:** Boxplots of the soil temperature values at 30 cm depth at all sites. All values of the study period from February to August 2022 are included.

A similar constellation of the boxes with soil temperature values could also be observed at depth 50 cm. Poor001 had again a wider interquartile range than the other sites, as did site Meteo. However, Meteo had the lowest median at 50 cm, while the "well" sites had almost the same medians higher than 12 °C, which were clearly higher than the rest of the sites. The Kruskal-Wallis test showed a significant result. The comparison of the sites with the Dunn test had a significant result of 0 or almost 0 for all sites, except for the comparison of Poor001 and Poor002 with a p-value of 0.3564.

Comparing the values between the different depths, it could be observed that the soil temperatures decrease with decreasing depth. This observation applied to all sites. Furthermore, the "well" sites showed higher medians at all depths, whereas Meteo had the lowest values except for depth at 10 cm.

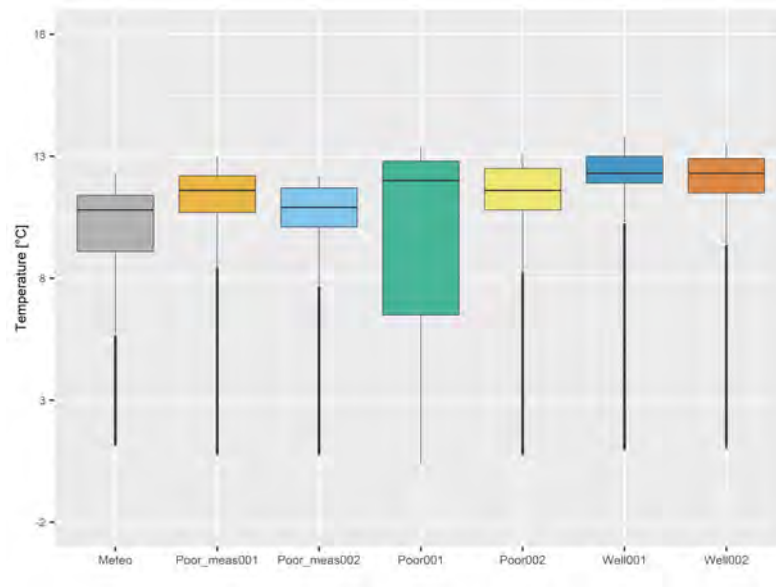


**Figure 17:** Boxplots of the soil temperature values at 50 cm depth at all sites. All values of the study period from February to August 2022 are included.

### 3.3.4. ERT Survey Periods

Figure 18 and 19 provide an overview of the weather and logger data during the ERT survey periods in July and August. Precipitation, air temperature and vapour pressure deficit are displayed from the weather station. The VPD is presented in order to estimate the evapotranspiration of the plants. The VWC values are shown only from the ERT survey sites Poor\_meas001 and Well001, for a more direct comparison. The ERT survey dates are marked in the figure.

The ERT measurement in July took place during a dry phase, which is referred to in figure 11. Shortly before the start of measurement on 04.07.2022, a precipitation event of 15 mm took place, afterwards there was no more precipitation until 23.07., then a precipitation event of 14 mm took place. The temperatures increased from 13.07. on, with the VPD behaving parallel to the air temperature. After the first precipitation event, a clear reaction from the VWC values could be observed at both sites. The 10 cm sensors showed the clearest reaction with similar peak height, whereby a slight delay between the sites could be observed, probably due to interception. At the lower sensors 30 and 50 cm, Well001 showed higher VWC values. After the first precipitation event a reaction from both sites could be observed at 30 and 50 cm, with a higher reaction from the Well001 site, Poor\_meas001 reacted much shallower. After the 04.07., the VWC values dropped constantly, most strongly at 10 cm. The values at 50 cm remained constant, with no response to the high temperatures and dry conditions.

After the second precipitation event at 23.07., the response of the sites was much more different. The 10 cm sensor from Well001 reacted clearly to the precipitation, whereas no increase was visible at Poor\_meas001. The sensors at 30 and 50 cm, also didn't show a clear response from the

Poor\_meas001. At Well001 the increase was still visible at 30 cm even though less clearly, but not at 50 cm. Interesting to observe is that the VWC values from Well001 increased to a higher value than Poor\_meas001 and remained higher.

The conditions during the ERT survey in August are illustrated in figure 19. During this period, three smaller precipitation events of 3-4 mm were recorded. Air temperatures decreased and VPD remained low during the period of precipitation. In contrast to figure 18, the sensors from Well001 had higher VWC values than Poor\_meas001 at all depths. At 10 cm, the Well001 showed a clear increase after each precipitation event, while Poor\_meas001 showed only a very shallow and delayed increase. At the lower depths 30 and 50 cm, the sensors of Poor\_meas001 did not react to the precipitation at all. Well001 showed rather high increases in VWC with a slight delay due to infiltration. The difference to 10 cm is that only one peak is visible and not after each precipitation event. In addition, it could be observed that at 50 cm depth a large difference of about  $0.1 \text{ m}^3/\text{m}^3$  existed between the sites.

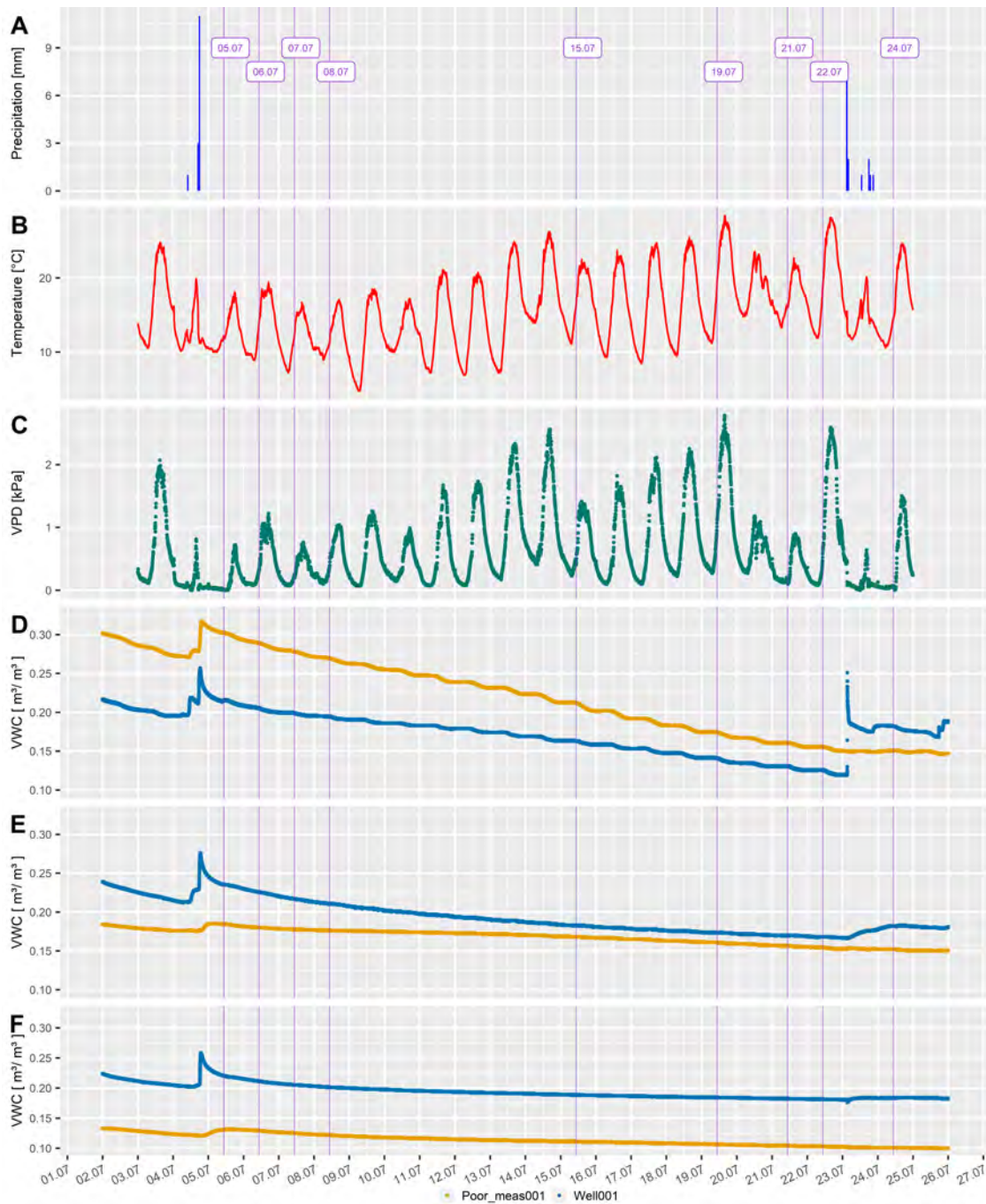


**Figure 18:** Overview of the weather and volumetric water content data during the ERT survey period in July from 02.07-26.07 with focus on the sites Poor\_meas001 and Well001. **A** Hourly precipitation from weather station Lücherwald, **B** Air temperature from weather station Lücherwald, **C** Vapour pressure deficit from weather station Lücherwald, **D** VWC at 10 cm from sites Poor\_meas001 and Well001, **E** VWC at 30 cm from sites Poor\_meas001 and Well001, **F** VWC at 50 cm from sites Poor\_meas001 and Well001. The purple highlighted areas indicate the ERT survey dates.

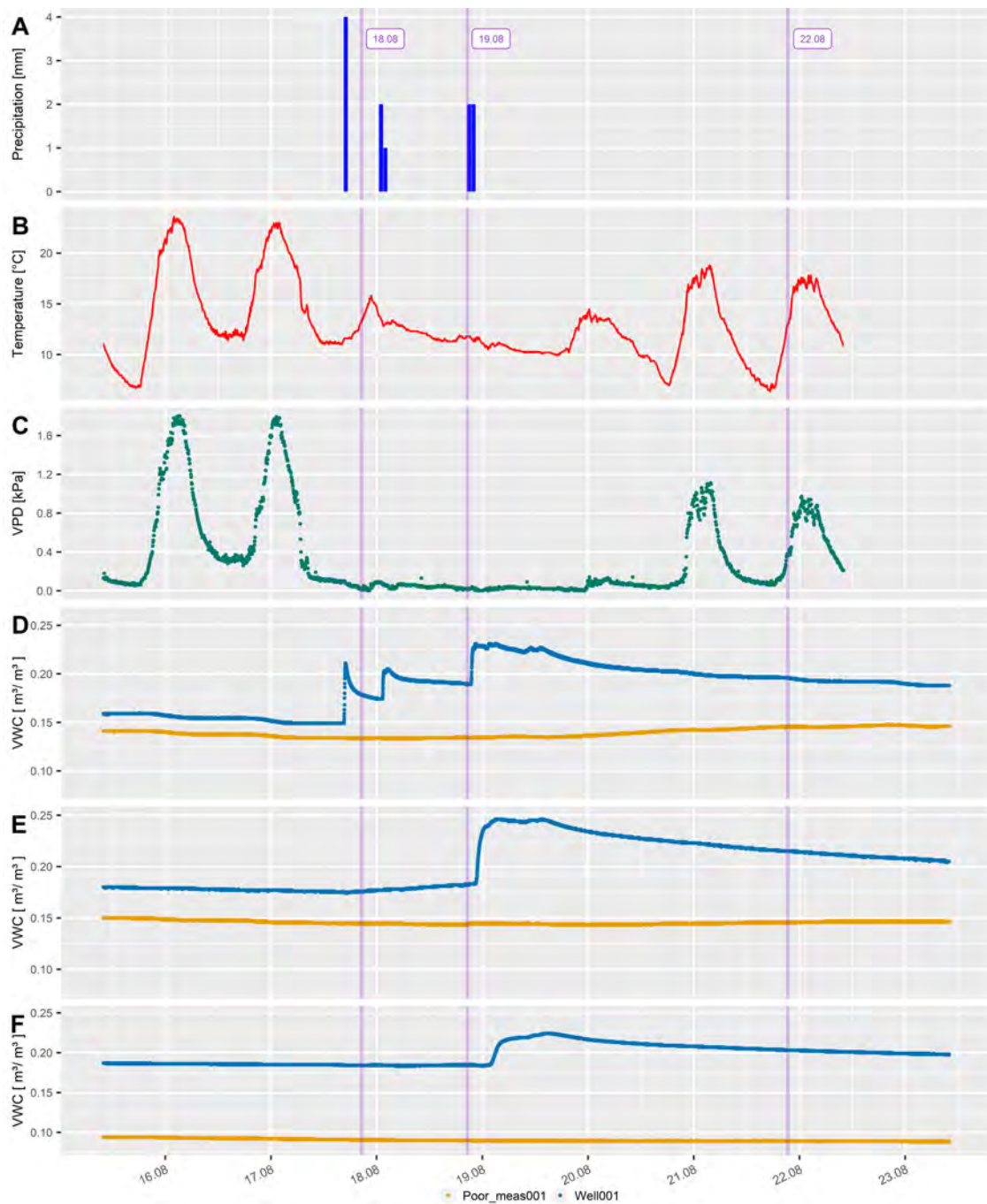
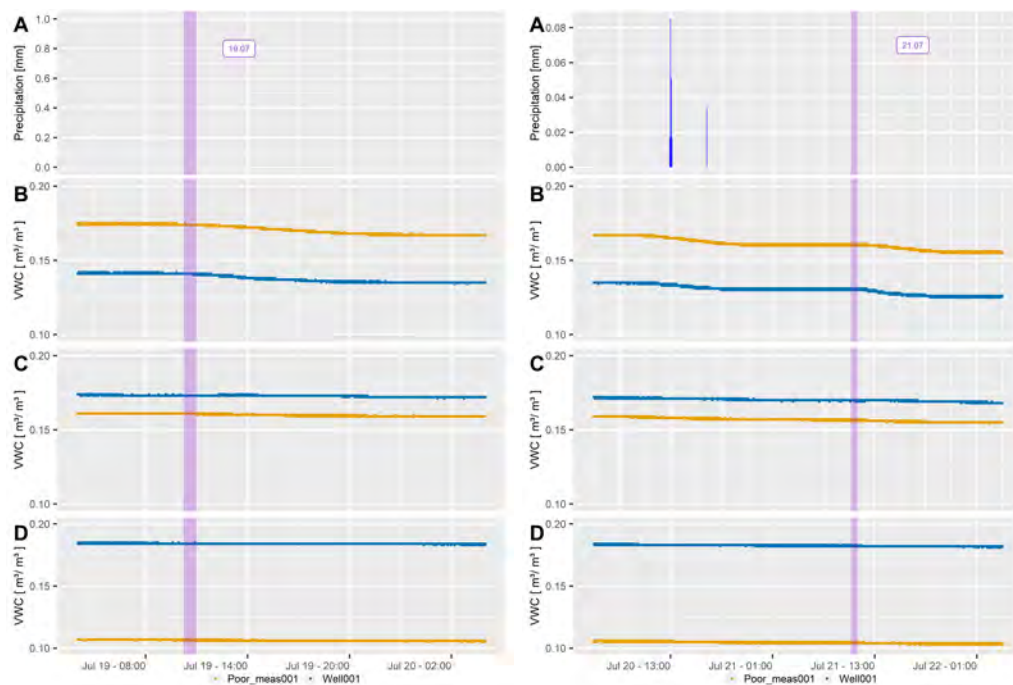


**Figure 19:** Overview of the weather and volumetric water content data during the ERT survey period in August from 16.08-23.08 with focus on the sites Poor\_meas001 and Well001. **A** Hourly precipitation from weather station Lücherwald, **B** Air temperature from weather station Lücherwald, **C** Vapour pressure deficit from weather station Lücherwald, **D** VWC at 10 cm from sites Poor\_meas001 and Well001, **E** VWC at 30 cm from sites Poor\_meas001 and Well001, **F** VWC at 50 cm from sites Poor\_meas001 and Well001. The purple highlights indicate the ERT survey dates

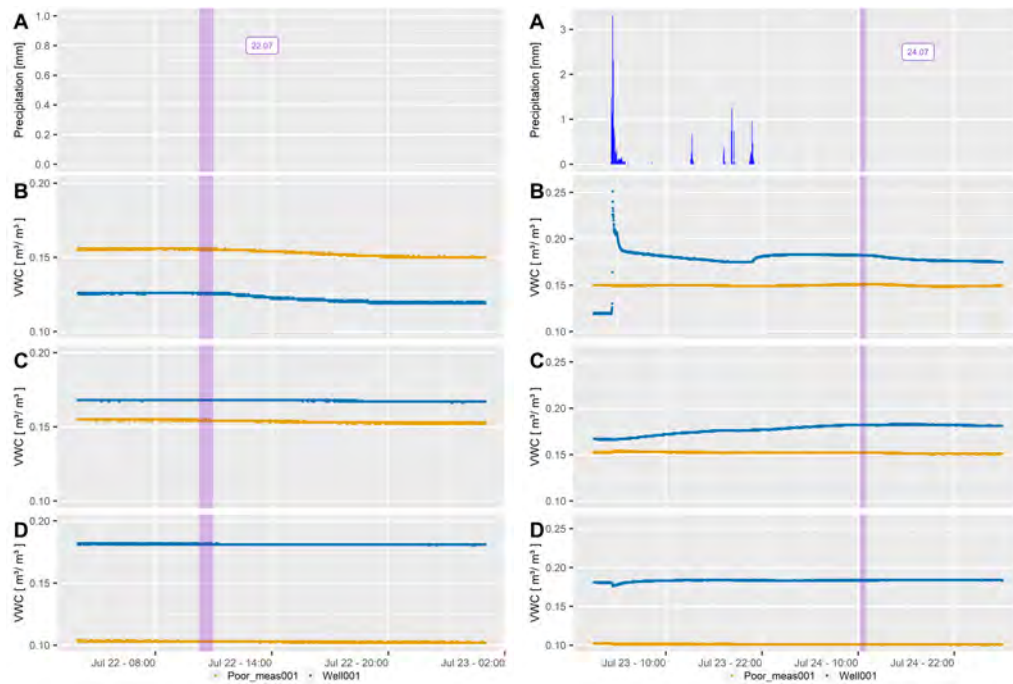


The following detail figures are intended to illustrate the VWC conditions in high resolution during the period of the ERT surveys. Precipitation and VWC are shown for all depths. Figures 20 and 21 cover the measurement in June, whereby only the last four measurements are considered in detail. The left overview in figure 20 shows the conditions on 19.07., when temperatures were still high. This could be observed at the VWC values of 10 cm, which continued to drop during the day. In contrast, at 30 cm only a slight decrease could be observed, whereas at 50 cm no change was visible. At 50 cm the difference between the sites is striking, Poor\_meas001 had much lower VWC values than Well001. On the right-hand side of figure 20, a small precipitation event is visible, but the amount of precipitation was too small to observe a reaction in the VWC values. Otherwise, at 10 cm it is clearly visible, how the VWC continued to decrease during the day. At 30 and 50 cm, no changes could be observed.

The graph on left-hand side in figure 21 shows the period of the ERT measurement at 22.07.. No precipitation event took place during this period. The VWC values showed a slight decrease over the day. A small decrease can also be observed at the 30 cm sensors. The graph on the right-hand side in figure 21 shows the period before the last ERT survey of the series on 24.07.. The figure shows the precipitation event from 23.07.. The reaction was clearly visible at site Well001, where the 10 cm VWC value increased within a few minutes after the beginning of the precipitation. The value decreased again within hours, but remained higher than Poor\_meas001, as VWC of Well001 was lower before the precipitation. There was a second smaller precipitation event, after which the VWC values of Well001 again increased, but less distinct. During the ERT survey, the VWC value was still increased. At the 30 cm sensor, the increase also started at the beginning of the precipitation event and levelled off again at a higher value shortly before the ERT survey. At 50 cm, a slight decreasing trend was visible at the start of the precipitation event, whereby the cause is not known. Otherwise no reaction could be observed to the precipitation event. At Poor\_meas001 no reaction to the precipitation event could be detected at all depths.

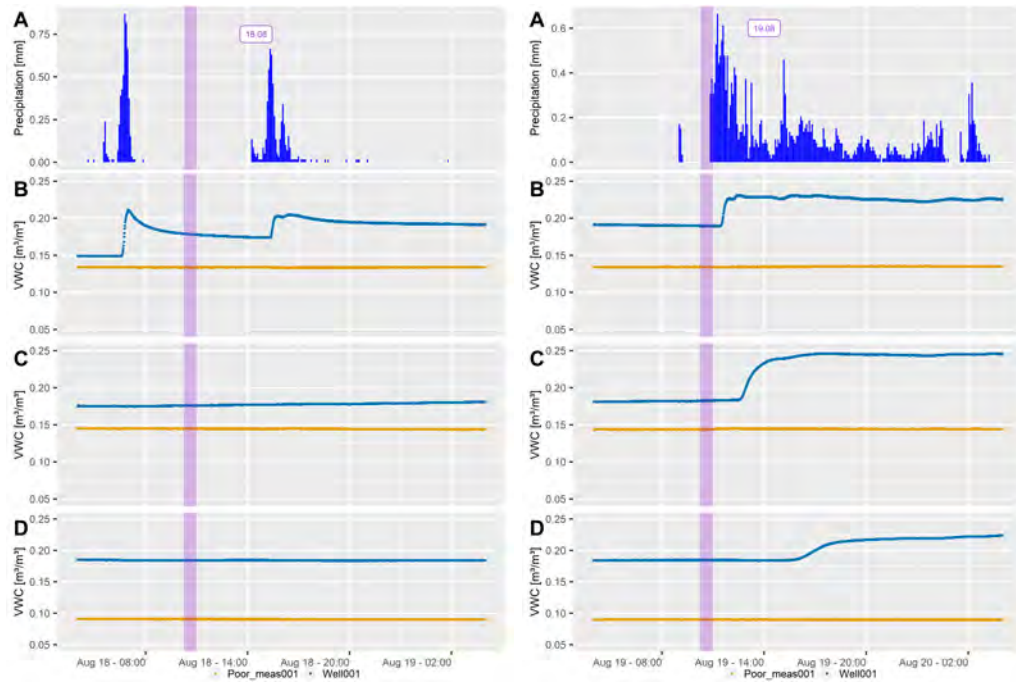


**Figure 20:** Detailed illustration of precipitation from the weather station Lücherwald and VWC during the ERT survey period. The left figure covers the measurement from 19.07. and the right figure the measurement from 21.07.. The purple highlighted areas indicate the time period of the survey.

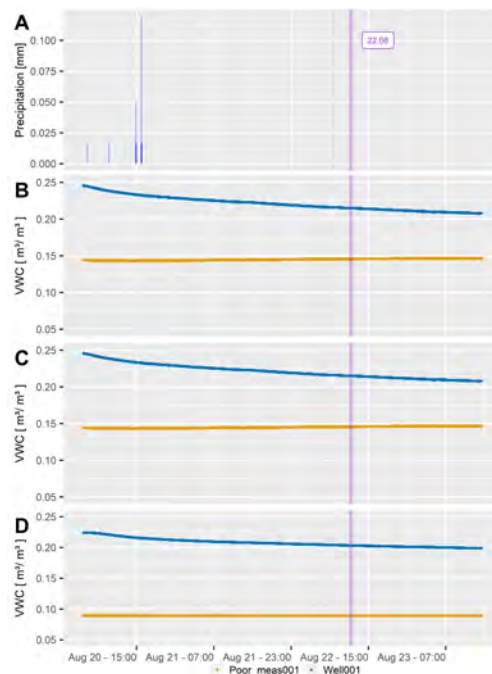


**Figure 21:** Detailed illustration of precipitation at the weather station Lücherwald and VWC during the ERT survey period. The left figure covers the measurement from 22.07. and the right figure the measurement from 24.07.. The purple highlighted areas indicate the time period of the survey.

Figure 22 and 23 show the detailed view of the ERT survey in August. The left side in figure 22 shows the measurement from the 18.08., which took place between two precipitation events. After both precipitation events, the 10 cm sensor of Well001 started to increase, whereby the second peak was less high than the first both over  $0.2 \text{ m}^3/\text{m}^3$ . The value remained high after the second precipitation. During the ERT survey, the VWC value was decreasing again. Shortly after the measurement, the 30 cm sensor showed a flat and shallow increase. The Poor\_meas001 sensors showed no reaction to the precipitation event at all depths and remained stable at nearly  $0.15 \text{ m}^3/\text{m}^3$ . On the right side in figure 22 is the measurement from 19.08., which was performed shortly before a longer precipitation event. Well001 clearly showed an increase of VWC values after the beginning of the precipitation. A time shift between the sensors due to infiltration could be observed. In addition, the increase flattened out with depth. The sensors of Poor\_meas001 showed no reaction to the precipitation at all depths. It could be clearly detected that the VWC values of Well001 on 19.08 were much higher than those of Poor\_meas001 at all depths also in comparison to the previous day. Especially at 50 cm depth there was a difference of almost  $0.1 \text{ m}^3/\text{m}^3$ . The VWC conditions during the last ERT survey of the series at 22.08. is depicted in figure 23. A small precipitation event still occurred, but with a negligible amount, as no reaction could be detected in VWC values. The VWC values of Well001 were already steadily decreasing before the ERT measurement. A small increase could be observed in the 10 and 30 cm sensors of Poor\_meas001, which is quite striking due to the delayed reaction. However, the 50 cm sensor remained stable below  $0.1 \text{ m}^3/\text{m}^3$ .



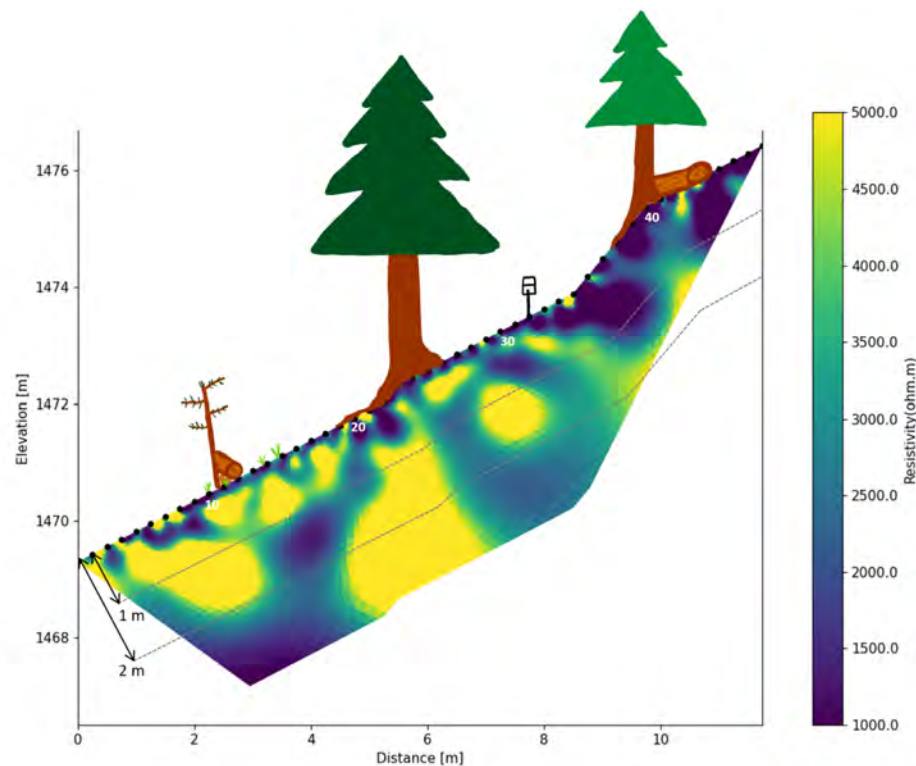
**Figure 22:** Detailed illustration of the precipitation at weather station Lücherwald and the volumetric water content VWC during the ERT survey period. The left figure covers the measurement from the 18.08. and the right figure the measurement from the 19.08.. The purple highlights indicate the time period of the survey.



**Figure 23:** Detailed illustration of the precipitation at weather station Lücherwald and the volumetric water content VWC during the ERT survey period. The figure covers the measurement from the 22.08.. The purple highlights indicate the time period of the survey.



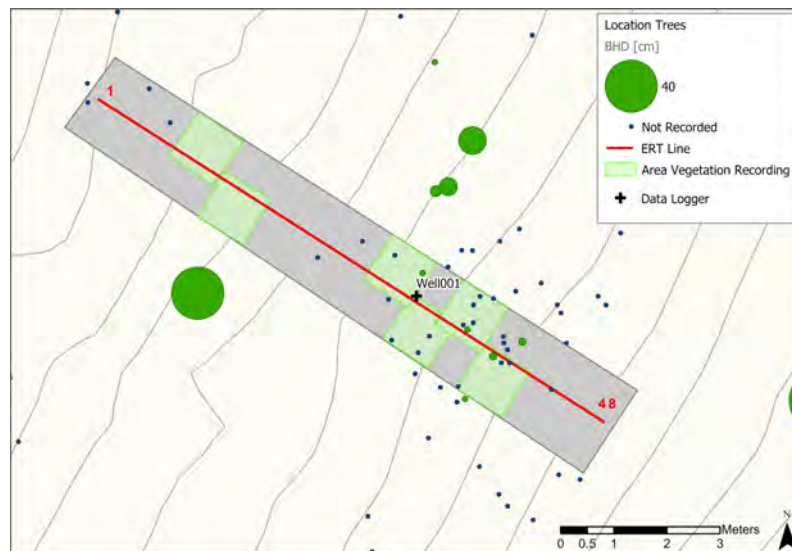




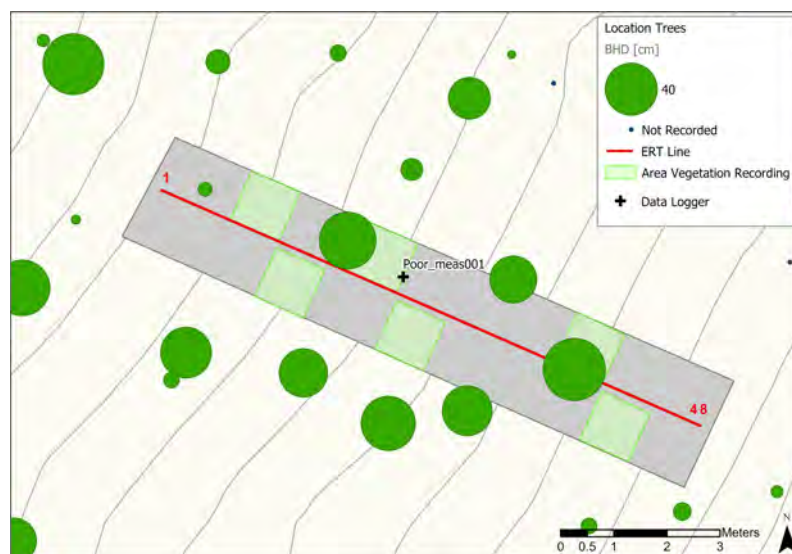
**Figure 25:** Electrical resistivity tomogram at site Poor\_meas001 from the 18.08. with dipole-dipole array. For a better orientation and imagination, the vegetation layers were drawn schematically, as well as a scale for the depth. The white numbers indicate the number of the electrodes.

Figure 24 shows the tomogram from site Well001 at 18.08. with the dipole-dipole array. Figure 25 shows the tomogram from site Poor\_meas001 with dipole-dipole array. In both figures two guide lines for 1 and 2 m are drawn as orientation. The drawings of the surface vegetation in cross-section is intended to give an impression of the situation at the study sites. In addition, the illustrations should simplify the interpretation of the tomograms. The maps ?? and 27 show site Well001 and site Poor\_meas001 from a bird's eye view to provide a better overview of all existing trees and tree regeneration in the surrounding. A detailed description of the vegetation and soil cover at the sites can be found in chapter 3.1.

Both overview illustrations for site Well001 show that herbaceous vegetation and smaller shrubs were present. Near electrode 10, a deadwood log lied across the site and near electrode 23 a spruce with DBH 40 cm was present. Between electrodes 25-40 mainly herbaceous vegetation could be found with occasional spruce regeneration. In the upper area at electrodes 40-45 was larger tree regeneration present. The map 26 shows that apart from the large spruce at electrode 23, no other trees of the same size was present at the site. Near electrode 30 were three more trees with a smaller DBH present. The blue dots in the maps show the existing tree regeneration, which was still too small for recording a DBH. At site Poor\_meas001 sporadic herbaceous vegetation was present in the lower part of Poor\_meas001 between electrode 0-15. Near electrode 10 standing and lying deadwood was present. Close to electrode 25 stood a spruce with DBH 44 cm and one at electrode 40 with DBH 48 cm. Above the spruce a deadwood trunk lied across the site. The overview map of the Poor\_meas001 (see figure 27) illustrates that there were many further spruce trees close to the site, but which were not situated directly at the ERT profile line. Compared to Well001, it is clearly visible that Poor\_meas001 is located in a much denser spruce stand.



**Figure 26:** Overview maps of the ERT survey site Well001. The map gives an impression of how many trees are located at the sites as the exact location. The radius of the circle gives an indication of the DBH of the trees. The blue dots indicate regeneration that was too small to record the DBH mass.



**Figure 27:** Overview maps of the ERT survey site Poor\_meas001. The map gives an impression of how many trees are located at the sites as the exact location. The radius of the circle gives an indication of the DBH of the trees. The blue dots indicate regeneration that was too small to record the DBH mass.

### 3.4.2. Individual Electrical Resistivity Tomography

The individual electrical resistivity tomograms from the July survey are presented in figure 61 to provide a good comparison between the sites. The tomograms of the last four measurement dates 19.07. - 24.07. are shown from both sites Poor\_meas001 and Well001.

Considering the tomograms of Poor\_meas001, similar resistivity patterns were clearly recognisable over the survey dates. The tomograms showed a small-pattern structure of high and low resistivity over the entire depth, which makes it difficult to interpret. Assuming that the rooting zone extends to about 1.20 m, the high resistivities in the topsoil could be explained by the increased water consumption of the trees in the main rooting zone and the tree roots itself. As mentioned, the site Poor\_meas001 was located in a dense spruce stand and lied between several trees with DBH above or below 40 cm. However, dense rooting can be assumed over the total ERT profile line. Whereas in the lower area at electrode 1-10, as well as in the upper area near electrode 43-48, there were fewer trees in the surroundings. Near electrode 43-48, lower resistivity could be observed, which is assumed to be due to better water infiltration and less canopy coverage. In this area, a richer moss cover was also found during the profile mapping. Below the rooting zone, a more constant pattern of high resistivities could be observed, which may be shaped by the presence of bedrock. For example, at the areas near electrode 5-10 or further in depth at electrode 18-24, bedrock could be the cause. The deep resistivities deeper than 2 m may indicate possible water drainage in the ground, such as between electrode 1-10. In general, the areas with low resistivity are assumed to be soil without larger roots or rocks, allowing better infiltration. In the area of electrode 10-18 below 1 m, there was deep resistivity, whereby this could be a possible drainage path of water along the potential bedrocks. The high resistivity at the surface between the electrodes could be explained by poor contact from electrode to soil and should therefore not be taken into consideration. In the comparison of the tomograms between the measurement dates from 19.07.-22.07. only minor changes regarding the resistivity could be observed. The precipitation event took place between 22.07. and 24.07., as visible in figure 18. A logical decrease of the electrical resistivity due to the precipitation is difficult to recognise in the tomogram of the 24.07.. Only in the area of electrodes 43-48 a slight decrease of the resistivity could be observed, but this area is also disturbed by bad contact of the electrode to the ground, which makes an interpretation difficult.

Repeating patterns could also be observed over the survey dates from site Well001. Compared to Poor\_meas001, there were fewer small-scale patterns. In the surrounding of Well001 only one tree with DBH around 40 cm existed. It is possible that the high resistivity within the rooting zone near electrode 14 to 17 was caused by this tree due to water consumption and existing roots in the soil. Near electrode 35-48 was mainly spruce regeneration found on the surface, which could form the high resistivities located in the rooting zone. However, the probability is low that spruce regeneration is already growing roots to a depth of 50 - 100 cm. Between electrode 26 and 35 there is an area below 1 m with higher resistivities in the range of 3500 ohm m, which were possibly caused by lower water infiltration. In comparison to Poor\_meas001, lower resistivities were observed below 1 m, which could be due to less bedrock in the subsurface or higher water infiltration. Comparing the tomograms between the survey dates, an increase of resistivity could be observed, for example in the upper area between electrode 35-48 or in the lower area between electrode 10-17. The dry conditions and high temperatures could be an explanation for the increase of resistivity. The precipitation event is clearly visible in the tomogram at 24.07. compared to Poor\_meas001, as the topsoil showed a decrease in resistivity across the entire profile line. Partly, the decrease in resistivity also extended deeper into the profile.

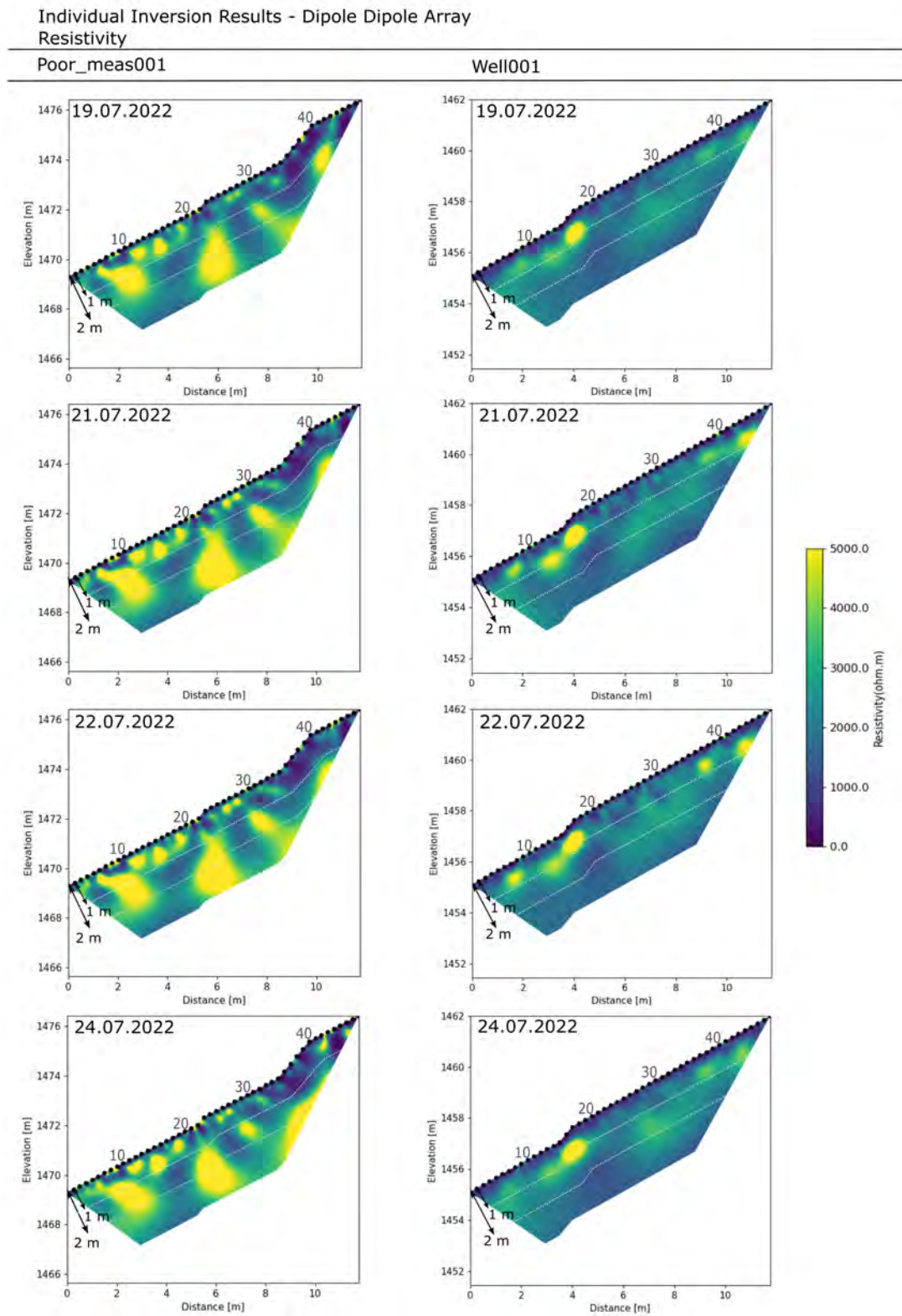
There are no clear differences between the tomograms with dipole-dipole array and those with Wenner-Schlumberger array (see appendix D.2). The Wenner-Schlumberger tomograms show mainly the electrical resistivities in the rooting zone because of the lower depth range, but similar patterns were visible as in the dipole-dipole array. The lower resistivities near electrode 43-48 at Poor\_meas001 can be seen nicely, as well as at Well001 the high resistivity caused by the spruce at electrode 14-17. The deeper resistivities in the topsoil due to precipitation can be seen clearly, especially at Well001.

Figure 29 shows the individual electrical resistivity tomograms of the August survey from 18.08.-22.08.. The tomograms in August show similar resistivity patterns as the July tomograms, but the electrical resistivities in general appeared to be slightly higher. At site Poor\_meas001 the area of resistivity between electrode 1-13 appears to be much larger and wider, as well as the area deeper in the subsurface between electrode 26-40. As this low resistivity areas lied below the rooting zone, the effect from trees can be excluded. It is unclear why the resistivity appeared higher in August, although the weather conditions in July were much drier and higher resistivity would be expected. The remaining patterns could also be seen in the July tomograms. According to figure 19 the precipitation events occurred on 18. and 19.08. Between electrode 35-48 clear resistivity changes to lower values could be observed between the survey dates, whereby on 19.08. the lowest resistivities could be recognised.

The situation at the Well001 site appears similar, as the same patterns as in the tomograms of July could be observed. Only the increased resistivity on 22.08. at 2 m between electrode 22-26 was seen for the first time in a tomogram, but it is not clear what formed it. The precipitation events could be clearly recognised by the decrease in resistivity at the topsoil. In addition, on 22.08. a decrease in resistivity could be observed between electrodes 11-13 at a depth of about 1 m, which may have been caused by infiltration.

The comparison of the tomograms with dipole-dipole array and those with Wenner-Schlumberger array in August (see appendix D.2) shows, that similar patterns down to 1 m depth could be observed. However, at Well001 less high resistivity was observed in the upper area near electrodes 34-48 compared to the dipole-dipole array tomogram. In contrast, the precipitation events were even better recognisable for both sites on the tomograms with Wenner-Schlumberger array, based on wetting of the topsoil and water infiltration.

Regarding absolute values, electrical resistivity values for gravel and sand range from 50 ohm m when wet to  $>10^4$  ohm m in dry conditions, whereas compact rock can reach even higher resistivity in range of  $10^5$  and  $10^6$  ohm m [19]. With reference to chapter 3.2, in which the soil type was determined, as well as the initial geology, the range of electrical resistivities in the tomograms would fit to the material.



**Figure 28:** Individual electrical resistivity tomograms from the sites Poor\_meas001 and Well001 with the dipole-dipole array from the July survey. The tomograms from 19., 21., 22. and 24.07. are shown.



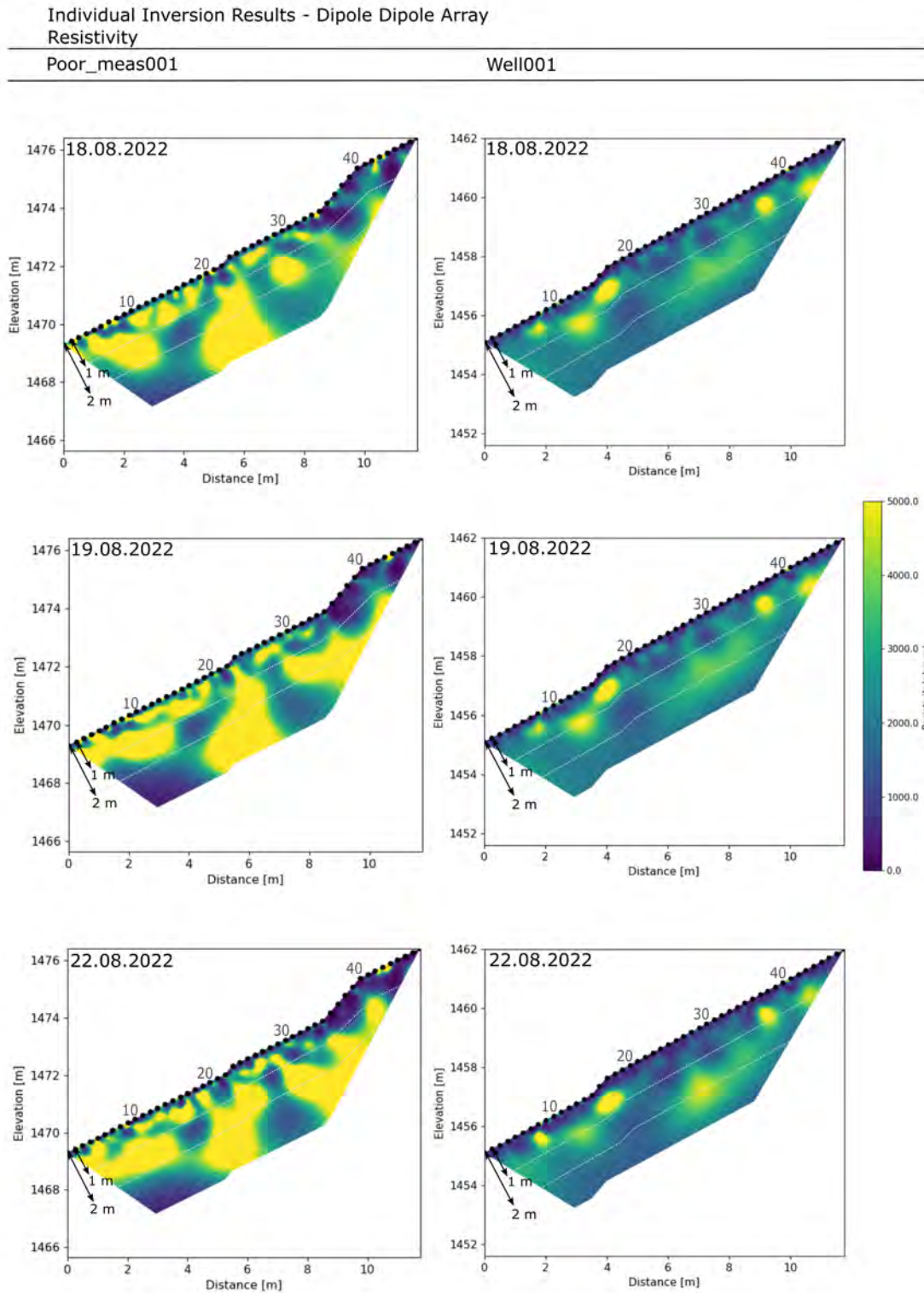


**Figure 29:** Individual electrical resistivity tomograms from the sites Poor\_meas001 and Well001 with the dipole-dipole array from the August survey. The tomograms from the 18., 19., and 22.08. are shown.

### 3.4.3. Time-Lapse Electrical Resistivity Tomography

The results of the time-lapse inversion from the July ERT survey are provided in figure 30, where the differences in percent to the inversion of 19.07. are shown. At site Poor\_meas001 no clear differences could be observed from the 19.07. to 21.07. At 22.07. a large positive difference in the upper range between electrode 35-38 could be observed, as well as minor small-scale differences over the entire profile line. It is not clear what could have caused the large increase in resistivity, as it is not observed on other tomograms, it may be due to an error. The minor small-scale resistivity changes in the rooting space may be due to water consumption of the trees. The difference tomogram on the 24.07., after the precipitation event, shows many smaller positive and negative patterns of differences more pronounced than before, whereas an interpretation was not intuitive. In the upper area, a decrease in difference could be observed, which indicates lower resistivity maybe due to the precipitation and though water infiltration. The small-scale differences along the profile line may be due to inhomogeneous infiltration or errors caused by poor electrode contact.

Site Well001 only shows minor differences from the initial date 19.07. to 21.07. and 22.07.. A slight increase in differences could be observed at the surface, indicating higher resistivities, which corresponds to the dry and warm weather conditions. However, no changes can be seen further in the depth. Among other things, both difference tomograms showed partially high differences between the electrodes, which could be caused by poor contact between the electrode and the ground. The high resistivity difference on 21.07. near electrode 40 is not clear, whether this is due to poor electrode contact or some other cause. On 24.07. the precipitation event is clearly visible, as negative differences can be seen in the topsoil along the profile line, which indicates water infiltration. Positive differences could be observed near electrode 14-17, which could be caused by the roots of the spruce. Comparing the tomograms between the sites, greater variability and smaller-scale resistivity changes could be observed for Poor\_meas001. The difference tomograms with the Wenner-Schlumberger array (see appendix D.2) showed similar patterns as with the dipole-dipole array. The processes in the topsoil were even more clearly visible with the Wenner-Schlumberger array, especially the effect of the precipitation event could be nicely observed.

Figure 31 shows the difference tomograms from the August survey. Poor\_meas001 showed large differences from the initial date of 18.08. to 19.08. and 22.08.. The differences ranged in both positive and negative directions and sometimes reached more than 2 m deep. In the rooting zone, small positive and negative differences could be observed, which may indicate large resistivity changes due to tree roots. The high differences between the electrodes were probably due to poor electrode contact. In the lower area below 1 m, large negative differences could be observed, which indicate a decrease in resistivity. It is interesting that the difference tomograms do not obviously correspond to the resistivity tomograms, as they indicate much larger changes over the survey period, which could not be recognised in the resistivity tomograms (see figure 29).

In contrast, Well001 showed no large differences from 18 to 19.08., except for a slight decrease in resistivity at the topsoil, which fits to the precipitation. On 22.08., larger negative differences became visible in the topsoil, which may be due to water infiltration after the precipitation. Also known patterns such as the high resistivity difference between electrodes 14-17 could be observed, which was probably caused by the spruce roots. Deeper in the profile at 2 m, near electrodes 23-29, a high difference could be observed, which was also visible in the resistivity tomograms. Basically, the difference tomogram showed lower resistivities over the entire profile line, which corresponds with the precipitation event. The difference tomogram with the Wenner-Schlumberger array from the August survey (see appendix D.2) clearly show the small-scale resistivity changes in the topsoil of Poor\_meas001. The tomogram for 22.08. showed similarly variable differences as the dipole-dipole array. At Well001, the differences were consistent with the dipole-dipole array, although the resistivity increases on 22.08. were less pronounced. The resistivity decrease in the topsoil can be nicely observed.



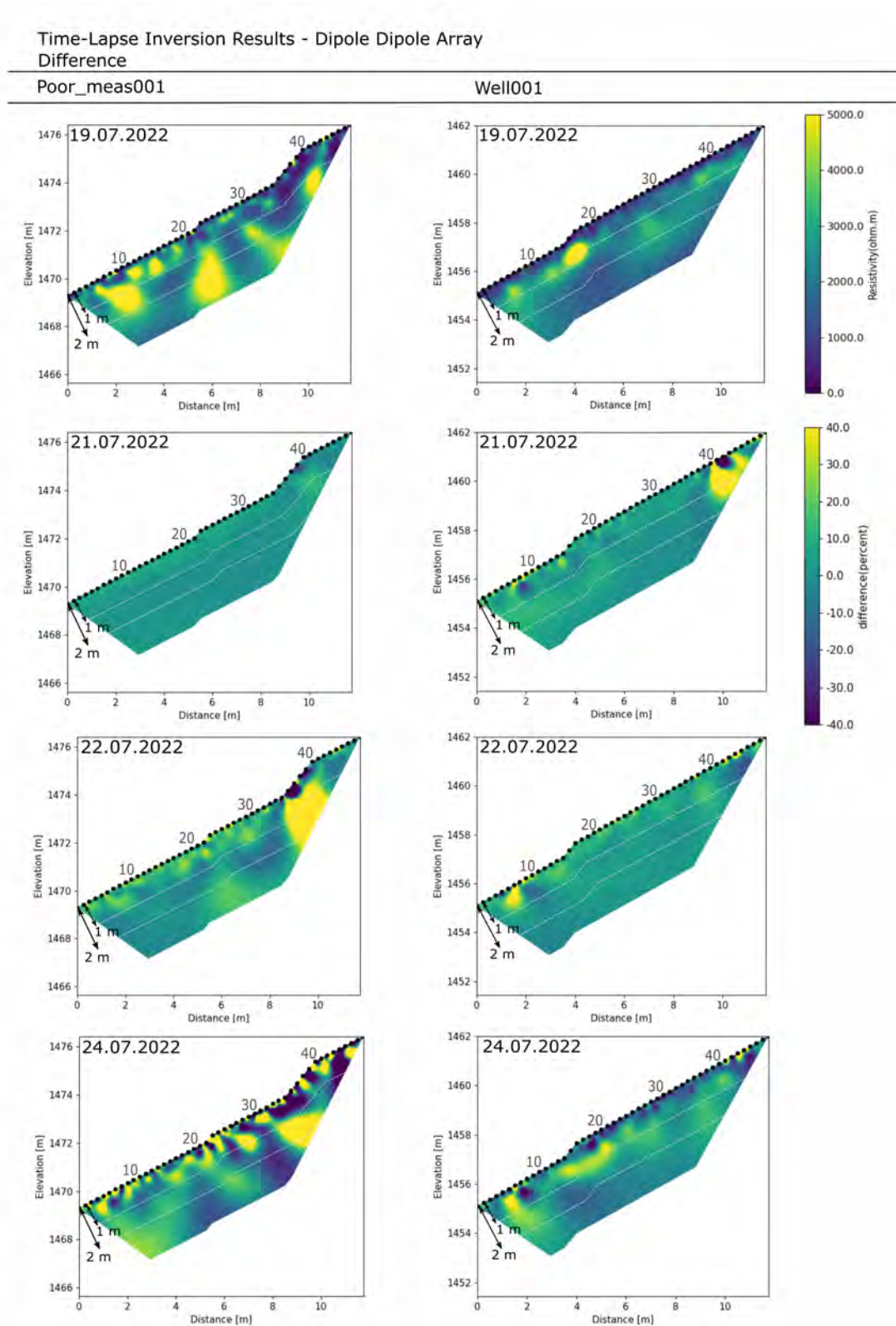


**Figure 30:** Time-lapse electrical resistivity tomograms from the sites Poor\_meas001 and Well001 with the dipole-dipole array from the July survey. From the 19.07. the electrical resistivity tomogram is shown. From the 21, 22. and 24.07. the difference tomograms are shown.

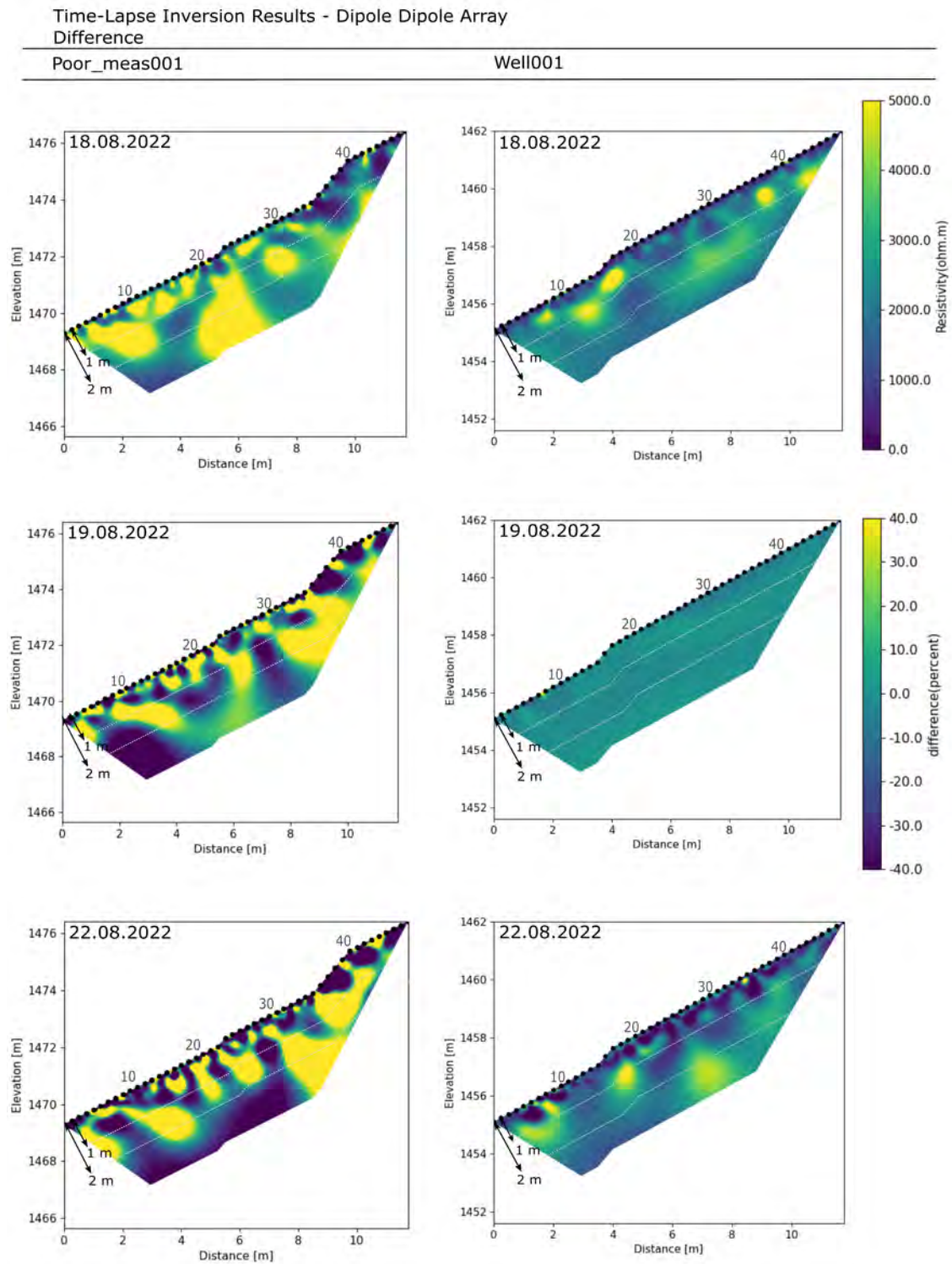


**Figure 31:** Time-lapse electrical resistivity tomograms from the sites Poor\_meas001 and Well001 with the dipole-dipole array from the July survey. From the 18.08. the electrical resistivity tomogram is shown. From the 19. and 22.08. the difference tomograms are shown.

#### 3.4.4. Analysis Electrical Resistivity Values

In the following chapter, the modelled electrical resistivity values of the ERT survey are analysed. Boxplots are used to compare the modelled resistivities of the two sites per survey date. In addition, a Wilcoxon test was used to examine whether the boxplots differ significantly. The histograms were used to analyse the distribution of electrical resistivity by survey date. In the results only the figures of the ERT survey with the dipole-dipole array are presented, those with the Wenner-Schlumberger array are shown in appendix D.3. Nevertheless, a comparison of the results of both arrays is described here.

The boxplots in figure 32 show the modelled electrical resistivity values of the ERT survey in July sorted by survey date and site. The result of the Wilcoxon test shows that the sites differ significantly on all survey dates. Comparing the resistivity medians between the sites clearly shows that Poor\_meas001 always had a higher median than Well001, which means higher electrical resistivity values for Poor\_meas001. In addition, the interquartile range of Poor\_meas001 was also wider over the entire measurement period, which implies a higher variability of the electrical resistivity values. The ranges and medians of both sites shifted upwards to higher values over the survey period, which corresponds to the mentioned dry period. However, this could be observed more clearly for Poor\_meas001.

The distribution of the modelled electrical resistivities from the sites per survey date is represented as histograms in figure 33. At Poor\_meas001, a right skewed distribution could be observed at the beginning of the survey. However, in the course of the survey the distribution pattern becomes more indistinct and the peak shifts from low to higher resistivity. Furthermore, the distribution becomes wider from 19.07. on, as higher resistivities were reached.

At the right side of figure 33 the electrical resistivity distribution from site Well001 is shown as histograms. The distributions did not show a clear distribution pattern. Compared to Poor\_meas001, the distributions tended to be narrower with less values in the high resistivity range. From 05.07.-08.07. there were distinct peaks in the range of 2000 ohm m, but from the 15.07. the electrical resistivities were distributed further to the right and the histograms became wider.

In both figures 32 and 33 the drying out of the soil due to the high temperatures and the absence of precipitation was visible from the 15.07 on, due to the increase of higher electrical resistivity values. The precipitation event on 23.07 can not be clearly observed in both illustrations.

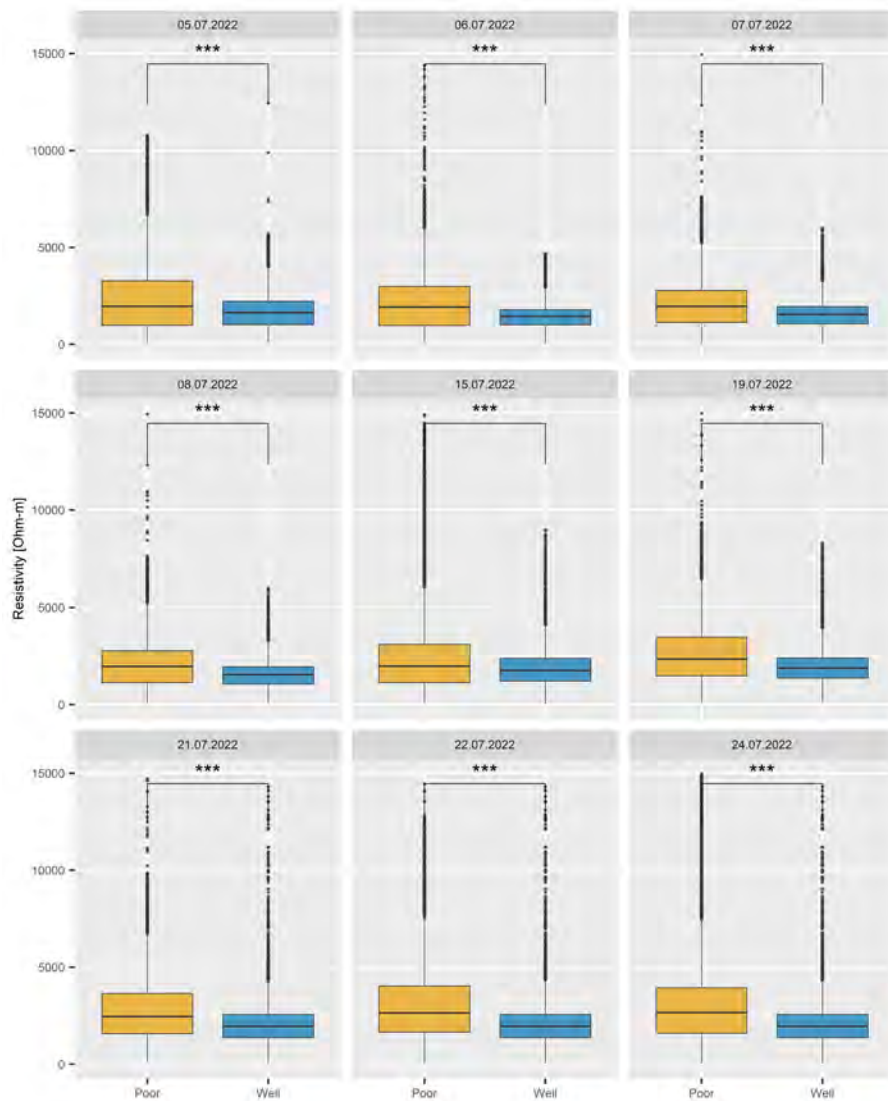


**Figure 32:** Boxplots of the modelled electrical resistivity values of the dipole-dipole array during July survey. All survey dates are presented.

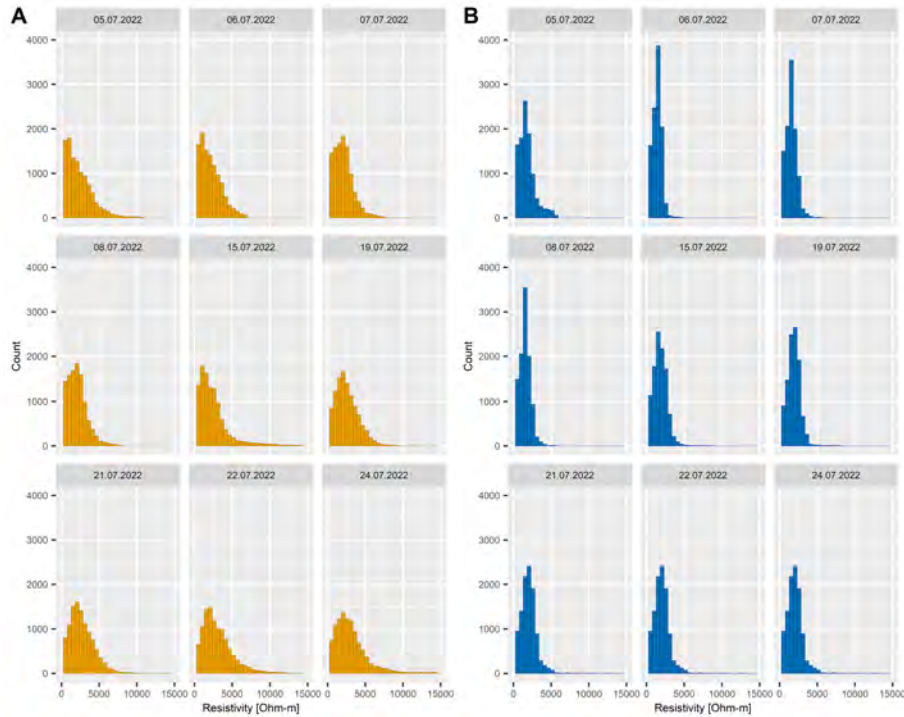


**Figure 33:** Histograms of the modelled electrical resistivity values of the dipole-dipole array during July survey. All survey dates are presented. **A** Poor\_meas001 and **B** Well001

Figure 34 shows the modelled electrical resistivity values of the August survey as boxplots. The Wilcoxon test showed for all survey dates that the sites differ significantly from each other. Similar to the survey in July, the Poor\_meas001 site showed a wider interquartile range than Well001, indicating a higher variability in resistivity. In addition, the medians of Poor\_meas001 were higher on all survey dates than Well001, which indicates higher electrical resistivity values. Considering the median of Poor\_meas001, it could be seen that the median increased on 19.08. and decreased on 22.08. than at the start of the survey. At Well001, the changes from the median were only within a small range, first a slight decrease and then a further increase on the 22.08.. The interquartile ranges from both sites on 22.08. expanded to lower resistivity values than on the other dates. The measurements of 18.08. and 19.08. were made between a precipitation event, which can be seen in figure 19. It is interesting to observe that the medians of the electrical resistivities were higher despite the precipitation event and only on 22.08. a decrease could be observed. At Well001, in contrast, there was no clear response to the precipitation, except for expanding the interquartile range to lower values.

The distribution of the electrical resistivities at the August survey is displayed in figure 35 as histograms. The distributions did not show any clear distribution patterns. Although, it is distinct that the electrical resistivities of Poor\_meas001 showed a flatter and wider distribution. In contrast, Well001 showed a clear peak on 18.08. close to 2500 ohm m. In the course of the survey period, Poor\_meas001 showed a slight decrease in electrical resistivity and thus a shift to the left, especially at the 22.08. after the precipitation event. At Well001, the clear peaks as well decreased and there was a shift to the left to lower resistivity values .



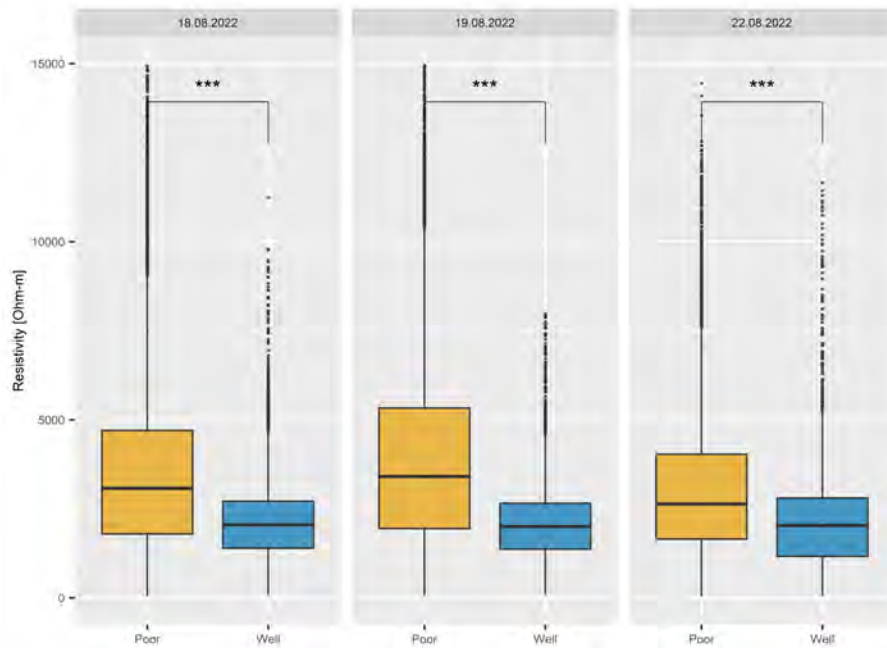


**Figure 34:** Boxplots of the modelled electrical resistivity values of the dipole-dipole array during August survey. All survey dates are presented.

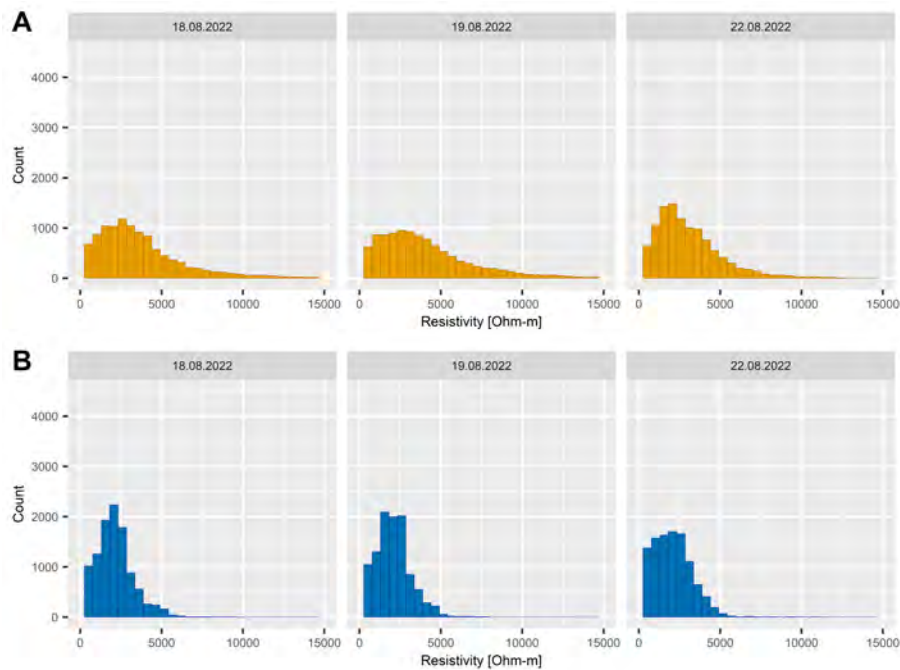


**Figure 35:** Histograms of the modelled electrical resistivity values of the dipole-dipole array during August survey. All survey dates are presented. **A** Poor\_meas001 and **B** Well001

Comparing the boxplots of the electrical resistivities between the dipole-dipole and the Wenner-Schlumberger array, for example at figures 32 and 65 (see appendix D.3), it could be observed that the interquartile ranges of both sites were wider in the Wenner-Schlumberger array. The medians

did not differ significantly, only after 19.07. the median of Poor\_meas001 did increase steadily. Compared to the dipole-dipole array, the median of Poor\_meas001 decreased more strongly at Wenner-Schlumberger array, after the precipitation event. Well001 also showed a more pronounced change in the medians with Wenner-Schlumberger than the boxplots of the dipole-dipole array. It is important to note that the count of data points of a ERT measurement differs strongly between the arrays. The histogram comparison between the two arrays from the July survey in figure 33 and 66 (see appendix D.3) showed no clear differences. Only the reaction to the precipitation event was more clearly recognisable in the Wenner-Schlumberger array as a leftward shift with a reduction in the resistivity.

The boxplots in August in figure 34 and 67 (see appendix D.3) showed no great difference between the arrays. Only the interquartile ranges of the dipole-dipole array reached higher resistivity values. The resistivity distribution in the histograms in figure 35 and 68 (see appendix D.3) showed a more irregular and narrower distribution in the Wenner-Schlumberger array, especially for Poor\_meas001. However, Well001 showed stronger peaks, but a narrower distribution. Overall, the output of the histograms do not differ strongly for both arrays. The Wilcoxon test for all Wenner-Schlumberger array boxplots showed a significant result, which means the sites differed significantly.

#### 3.4.5. Correlation of Electrical Resistivity and Volumetric Water Content

In the following chapter, the comparison of the electrical resistivity values and the corresponding VWC values is shown in a scatter plot. The aim was to check whether the theoretical relationship between electrical resistivity and VWC is fulfilled. Figure 36 compares the data points from all ERT surveys with the VWC values at the depths of 30 and 50 cm. The sites could be clearly separated vertically in the scatter plot, whereas Well001 showed higher VWC values than Poor\_meas001. Horizontally the distribution of the electrical resistivity was not that clearly separable. Considering only the right part of the trend line, mainly the values of Well001, the trend line showed the expected disproportionate course. In contrast, the trend line on the left part, mainly the values of Poor\_meas001, almost a horizontal line could be observed, which does not fulfil the theoretical assumptions.

Separating the values by depth, as in figure 37, the trend lines changed clearly. The left side in figure 37 shows the data points from 30 cm, with the blue trend line showing the curve including both sites and the green and red lines separated by site. For the depth at 30 cm, the trend lines give reasonable results, with the line for Poor\_meas001 showing a more curved shape due to outliers. The trend line from Well001 was a nearly linear function. The right side in figure 37 shows the data points of depth 50 cm. In this case, a clear vertical separation of the sites in terms of VWC could be seen, which results a strongly undulating blue trend line. However, if the trend line was divided according to sites, a better results was provided, which indicated the expected trend.

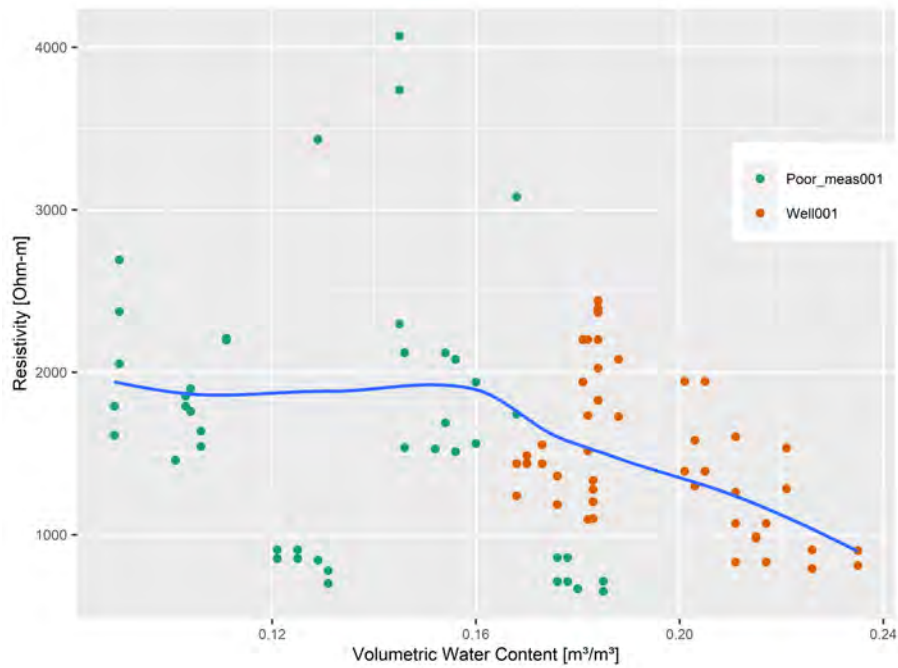


**Figure 36:** Scatter plot of VWC and electrical resistivity values from depths 30 and 50 cm. Data points from both sites and all ERT surveys were used. The blue trend line shows a smoothed curve according to the method LOESS.

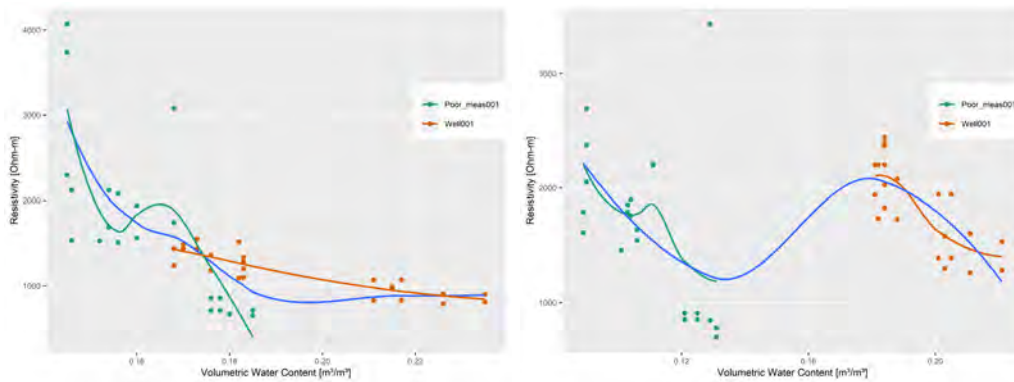


**Figure 37:** Scatter plot of VWC and electrical resistivity values separated by depth. Data points from both sites and all ERT surveys were used. The blue line shows a smoothed curve according to the method LOESS. The green and red lines show the smoothed curve of the respective site. On the left side are the data points from 30 cm and on the right side the data points from 50 cm illustrated.



## 4. Discussion

### 4.1. Vegetation Recording

The aim of the vegetation recording was to create an impression of the sites regarding soil, vegetation and canopy cover, as well as to point out the differences in coverage rate between the sites. Recording the different layers and categories allowed a more differentiated comparison of the sites. To address the second research question, it was particularly important to analyse the effects that the differences in coverage may have.

The results of the vegetation recording showed that in the soil layer no clear differences between the sites could be observed, except for the categories litter and moss. The "well" structured forest stands showed a higher percentage of moss cover and the "poor" structured forest stands a higher percentage of litter cover. The most distinct difference could be observed in the herb layer, where none of the "poor" structured forest stands achieved a cover above 10 percent at the end of the recording period. In contrast, the "well" sites showed almost 50 % of herb cover at the end of the recording period, with Well001 showing the lowest percentage with slightly higher than 30 %. The "poor" sites had no shrub layer and the "well" sites only a small one, thus no clear difference could be observed there. However, the difference in the tree layer was more distinct, as the "poor" structured forest stands showed a canopy cover of 62 - 77 % and the "well" structured forest stands one of 0 - 23 %. The species identification and their ecological indicators showed that mainly acid indicating species and neutral species were present. Most species were humidity indicators and only a few species indicated alternately wetness or dryness. On the "well" sites many humidity indicators were found and on the "poor" sites more dryness indicators. Acid indicators tended to be found more on the "poor" structured forest stands, which could be a consequence of the larger litter coverage, as the pH value of the soil layer normally decreases with an increasing litter cover [33]. However, for a conclusive statement, the herb cover of the "poor" sites was too low in comparison to the "well" sites.

The vegetation recordings clearly highlighted the structural differences between the sites. Based on these, a number of consequences can be inferred, which are caused by the structural differences and thus can influence the soil hydrology. The assumed consequences were important for the interpretation of the results of soil moisture trends and electrical resistivity tomograms. The sites differed significantly in terms of their soil cover, which can have a major influence on water infiltration. Poorly degradable litter such as spruce needles can form water-repellent organic overlay horizons, which make water infiltration more difficult and thus higher surface runoff can occur. In contrast, the infiltration capacity at the "well" structured forest stands might be considerably improved by the intensive herb and moss layer, also due to the roots. Clearly, water infiltration is also influenced by the rooting depth and intensity, whereby this is strongly dependent on the tree species [13]. At the study site only spruces occurred, which develop a shallow rooting system and thus create poorer conditions for deep water infiltration [20]. This thesis did not deal with the species composition in depth, but more diverse tree species would probably be better preconditions for a more diverse rooting depth and thus deeper water infiltration.

According to the vegetation recording, the sites showed large differences in the degree of canopy cover, which has a clear influence on the interception capacity. With decreasing canopy cover, the interception capacity decreases for individual precipitation events, but also on an annual average. However, for extreme precipitation events, the interception capacity decreases over time [22]. Therefore, it can be assumed that more precipitation reaches the ground at the "well" sites than at the "poor" structured forest stands. A low degree of canopy cover can also lead to a different micro climate, where the temperatures are significantly higher. This could be observed at the soil temperatures, as the "well" sites showed the highest medians in soil temperature for all depths (see figure 15). Another striking difference becoming apparent through denser forest cover, is the higher transpiration capacity than in more open stands, which can have a direct influence on soil

moisture, especially in the rooting zone [22].

The discussed structural differences clearly showed that the sites differ strongly regarding coverage rate of the vegetation layers. Especially visible from the canopy cover, as the "well" structured forest stands are located at the edge of a gap. The comparison of a dense spruce forest with an rather open forest stand could be criticised for being too contrasting in terms of forest structure. Also because the sites may differ too strongly, as many forest characteristics could be lost in the "well" sites due to the previous mentioned aspects. Placing the "well" sites in a more multi-layered stand with a wider DBH distribution and higher canopy cover could be more suitable to analyse the research questions.

Recording of vegetation coverage is a very subjective method, as it was made by only one person and therefore strongly influenced by personal assessment. For example comparing the canopy cover of the inventory from the cantonal geoportals with the canopy cover of this thesis, showed that they differ slightly. The canopy cover of the inventory map is 80 % [18]. Therefore, it is possible that the canopy cover was underestimated in this thesis. However, it must also be taken into account that in the cantonal inventory only one value is recorded for a large area. In this thesis the vegetation recording areas were punctual and only covered a small area of 1 m<sup>2</sup>.

A further consequence of the punctual vegetation recordings is that only the individual situations at the sites were described through the results and not the entire forest area. Due to the small-scale differences and heterogeneity of the forest area, it is not possible to generalise the results. For example, the vegetation recording leads to the impression that no tree regeneration was present in the "poor" structured forest. However, this did not describe the entire forest area, but only the marked sites.

## 4.2. Logger and Weather Station Data

In this thesis, the data from the weather station, the VWC and soil temperature values from the sensors at all sites were analysed from February to August 2022. Regarding both research questions, the long-term trend of the values was evaluated, but also the short-term trend before and after precipitation events with a focus on the ERT survey periods, as well as the possible correlation with the vegetation coverage rates of the layers.

The period of snowmelt was analysed in particular, as it is especially critical regarding shallow landslides because the soils are already highly saturated [13]. The analysis of the VWC trends showed that the "poor" structured forest stands reacted more strongly to snowmelt, especially at depth 10 cm, as the increase in VWC was higher than at the "well" structured forest stands. In contrast, Meteo showed the strongest response, which corresponds to the location in a gap without canopy cover, as there possibly was larger amount of snow in the gap than in dense forest. However, site Poor\_meas001 showed a large increase in VWC too, but over a much longer period of time. It is not clear why the increase was delayed. It might be related to the relief and the resulting surface runoff of the site.

During the larger precipitation event in late June (2nd highlight in the overview figure 11), a similar reaction could be observed. The "poor" structured forest stands showed again larger increases in the VWC than the "well" sites. Both observations are consistent with the observations of the preliminary investigations in the Dischma Valley Davos [15], indicating that soils in the "poor" structured forest stand react much stronger and more abruptly to larger precipitation events and snowmelt. The soil of the "well" structured forest stands instead, shows a clearly higher storage capacity, which could be observed in lower increases of the VWC values after snowmelt or precipitation. In this study, the differences in water storage capacity between sites were also most pronounced during snowmelt. In addition, an interesting aspect is that the factor interception is

not relevant in the case of snowmelt, but only when no precipitation occurs during the same time. Therefore, the differences in canopy cover between the sites can be omitted in this comparison, which further supports the observation of lower storage capacity at the "poor" structured forest stands. The second observation nicely confirms that the "well" sites can delay water saturation during a longer precipitation event [15].

The long-term analysis of the VWC values showed that the sensors at 10 cm had the highest variability, which was to be expected since the sensor is closest to the ground surface. This can be seen in the wide interquartile ranges in figure 12, but also in the stronger reactions of the curves compared to the deeper sensors (see figure 11). Over the entire study period the sites Meteo and Well001 showed higher medians of VWC values at all depths than the "poor" sites, which means the "well" structured forest stands tended to have higher soil moisture. Meteo probably had the highest median and variability because of its location in a gap without canopy cover, the site is therefore more exposed to precipitation but also to solar radiation.

Although, Well001 showed a higher median for 30 cm than for 10 cm, the other sites tended to show decreasing soil moisture with depth. Compared to the "well" sites, the "poor" structured forest stands tended to show lower VWC values at 30 and 50 cm and flatter responses to precipitation events. Also, Well002 had rather low medians of VWC values for 30 and 50 cm and did not follow the trend of Meteo and Well001. These observations could indicate that poorer infiltration and less deep percolation occurred at the "poor" sites in the denser forest stand, which might be related to the lower topsoil rooting. The 10 cm sensor of Poor001 had strikingly low VWC values with low responses compared to the other sites, but the 30 cm and 50 cm sensors of Poor001 were less extreme. Possible reasons for the low VWC values could be that the 10 cm sensor was located in a cavity or at a position, where no water is flowing through, referring to preferential flow in soils [1].

Based on the observation of the higher soil moisture values at the "well" sites, it is interesting to refer to the following studies with similar and confirming results. Breitsameter (1996) already observed that in thinned forest stands higher soil moisture values existed due to lower interception and lower evapotranspiration than in dense, non-thinned stands. From that study they concluded, the older the trees and the denser the forest, the faster the water tension increases in the intensively rooted zone [7]. Similarly, Hager (1988) observed that the looser the forest stand, the more slowly and less profoundly water is extracted from the soil [16].

For the time periods of the ERT surveys, only the VWC values for Well001 and Poor\_meas001 were analysed. The ERT survey in July was performed from 05.07. to 24.07.2022. The first survey was done after a precipitation event, which was followed by a dry and warm phase without precipitation until the 23.07.. After the first precipitation event the responses from the 10 cm sensor of Well001 was stronger in comparison to Poor\_meas001, as the increase was higher. This is probably related to lower interception and thus more precipitation reaching the soil, which can also be observed by the time shift of the peaks. In the deeper sensors at 30 and 50 cm the peaks of Poor\_meas001 were much flatter and less distinct (see figure 18), which is probably again related to lower water infiltration capacity to the deeper sensors at Poor\_meas001. During the second precipitation event, Poor\_meas001 showed no reaction at all, whereas the 10 cm sensor of Well001 showed a clear and high jump. However, the infiltration to the deeper sensors is also less pronounced here, which might be related to the dry soil and the small amount of precipitation [1]. Particularly interesting is that the 10 cm sensor of Poor\_meas001 was higher than Well001 before the second precipitation event, after that Well001 had overtaken Poor\_meas001. Referring to the overview in figure 11, Poor\_meas001 showed higher VWC values at the 10 cm sensor since the snowmelt and was only overtaken after the dry phase. In the other depths, Well001 showed always higher VWC values, as well as in the general comparison of the medians. This difference could be related to the poorer infiltration performance of Poor\_meas001, as the water infiltrates less to the deeper sensors and thus causes higher values for the 10 cm sensor.

The August survey took place from 18.08. to 22.08.2022, with precipitation events on 18.08. and 19.08.. The VWC sensors of Well001 showed clear responses to the precipitation with shallower peaks to increasing depths due to infiltration. In contrast, the 10 cm sensor of Poor\_meas001 showed a slight increase over several days but barely  $0.025 \text{ m}^3/\text{m}^3$ . In contrast, the 10 cm sensor of Well001 showed an increase of almost  $0.3 \text{ m}^3/\text{m}^3$ . The deeper sensors at 30 and 50 cm showed no response at all. It may be that Poor\_meas001 showed almost no reaction, since it was a rather small precipitation event, where it is possible that all precipitation was caught in the canopy due to interception. The large difference in VWC values between the sites was also particularly clear at the 50 cm sensor, as Poor\_meas001 was almost  $0.1 \text{ m}^3/\text{m}^3$  lower, indicating clear differences in percolation in the soil.

Overall, single point measurements only reflect the situation at a specific location and are thus less transferable. This could especially be observed on the results, as the expected trends were not always fulfilled, for example at site Poor001 and Well002. The large surface heterogeneity at the sites also influences the infiltration behaviour, which cannot always be measured with single point measurements. Especially soils can change considerably within a few metres regarding aggregate structure, porosity or stone content and thus influence the percolation behaviour of water. Water content measurements depend strongly on the porosity of the soil and the resulting preferential flow, which means that the water possibly did not always reach the sensor [1].

### 4.3. Electrical Resistivity Tomography

During this thesis, two ERT surveys were performed in July and August at the sites Well001 and Poor\_meas001, one with the dipole-dipole array and the other with the Wenner-Schlumberger array. The aim of the measurements was to provide spatial dynamics in soil moisture in a two-dimensional profile with electrical resistivity as an indicator for volumetric water content and as an addition to the single point measurements. The intention was to perform the measurements shortly before and after precipitation events, which was difficult to realise, so the time intervals were sometimes longer. In addition, comparing the locations, it should be taken into account that the measurements were performed not at the same time, but with a time shift of approximately 1 hour

In the data analysis, the modelled individual and time-lapse electrical resistivity tomograms were investigated. In addition, the distributions of electrical resistivity values between the sites were compared. The challenge in interpreting electrical resistivity tomograms was that it is made visually, which makes it very subjective and therefore depend on experience and practice. The results of the individual inversions showed that at Well001 the investigated precipitation events were clearly visible on the tomograms. A distinct decrease in resistivity in the topsoil could be observed due to water infiltration. Not all resistivity patterns could be clearly identified, but the effect of the roots from a large spruce, could be assigned. However, the effect of spruce regeneration could not be precisely attributed, as the roots might be not deep enough. Below the rooting zone, the resistivity seemed to be rather low and mostly homogeneous over the entire profile.

In contrast, the tomograms of Poor\_meas001 showed a more complex resistivity pattern in the rooting zone but also deeper in the profile, which made the interpretation more difficult. Stronger changes of resistivity patterns could be observed between the survey dates. The small-scale patterns in the rooting zone could be attributed to the higher rooting intensity and thus increased water consumption of the trees and the tree roots itself. Below the rooting zone, a more constant pattern of high and low resistivities could be observed, which may be shaped by the presence of bedrock. The deep resistivities deeper than 2 m may indicate possible water drainage in the ground, such as between electrode 1-10. The investigated precipitation events were only poorly visible on the tomograms, except for the upper area from electrode 43 upwards, where distinct lower resistivities could be observed after precipitation. Since this area was mainly covered with

moss, the water might have been infiltrated better there.

The results of the time-lapse difference tomograms were more difficult to interpret, especially for Poor\_meas001, as there were rather complex patterns of positive and negative differences. The tomograms gave the impression that considerably large differences occurred in the soil within one day, for example in the case of figure 31. The difference tomograms were also not fully complementary with the resistance tomograms. In contrast, site Well001 was much simpler to interpret. The displayed differences fitted better to the resistivity tomograms and the weather events.

The comparison with the results of Dick et al. (2018) showed that they also observed more heterogeneous soil moisture dynamic and wetting and drying patterns under forest than under shrub cover, which confirms the results from Poor\_meas001. They related the observations to vegetation distribution and canopy structure, as the dwarf shrubs produce a more homogeneous canopy cover than dense forest. Meanwhile, in the forest, the greatest changes were in the areas where the trees were concentrated, reflecting water uptake and canopy partitioning. This means forest area exerted a stronger influence on soil moisture than the shrubs. As under the shrub cover only small changes in soil moisture were visible during the growing season [10]. Nonetheless, the results cannot be completely transferred to this thesis, as the Well001 site is not completely covered with dwarf shrubs.

It seems obvious that the dipole-dipole array method was more suitable for this thesis, as it reached a greater investigation depth. The aim was to investigate the horizon of shallow landslides, which reaches up to 2 m, so the Wenner-Schlumberger array was less suitable, because it reaches only slightly more than 1 m depth. Nevertheless, the tomograms with the Wenner-Schlumberger array gave a clear impression of the rooting zone and thus a valuable addition for the analysis. As mentioned in the chapter 2.2.4, the Wenner-Schlumberger array provides a higher signal strength, which is advantageous in areas with higher background noise, such as soils with large heterogeneity for example high stone content [29]. The studied soils in this thesis are susceptible to background noise because the stone content is rather high and the organic content low, as it is typical for mountain forests [13].

As shown in the results, the high electrical resistivity between the electrodes indicated poor contact between soil and electrode. This could be observed at both sites, but more often at Poor\_meas001, which sometimes made the interpretation of the tomograms more difficult. Possible reasons for the errors could be poorly conductive ground such as dead wood, stones or dry soil. A possibility to reduce systematic errors of poor electrode contact or noise averaging are reciprocal measurements [29]. However, this was not done in this thesis due to time limitations.

The analysis of the modelled electrical resistivity values showed that Poor\_meas001 had higher medians and variability of electrical resistivity compared to Well001. Especially during the dry phase in July, it was clearly recognisable for Poor\_meas001, as the medians increased steadily over this time. In contrast, the precipitation events were not clearly detectable from the analysis of the electrical resistivities for both sites. In the August survey, the precipitation events were also not clearly visible, only at Well001 on 22.08. the resistivity was distributed more to a lower range, but the median remained the same. Overall, the observations corresponded well with the results of the VWC analysis, for example Poor\_meas001 showed the high electrical resistivities, but also low VWC values. The reactions to the dry phase and precipitation appeared to be more distinct from the electrical resistivity values with the Wenner-Schlumberger arrays. The reason for this was probably that the array only includes the values of the topsoil and most of the differences in electrical resistivity due to precipitation or drought occurred near the surface.

The results of the correlation analysis between electrical resistivity and volumetric water content showed that all data from both sites and sensors in one figure (see figure 36) did not provide the expected result. The expected result would be a convex function with the disproportionate

condition that decreasing electrical resistivity corresponds to increasing soil water content [29]. Considering only Well001, the function would appear quite reasonable, but the distribution of the Poor\_meas001 values is not suitable. However, if the values were divided according to sensor and site, the functions corresponded better to the expected result. Especially the depth 30 cm showed a nice result, whereas at 50 cm still a clear separation between the sites could be identified. In principle, the comparison of electrical resistivity and soil water content should be independent of location and depth. However, these ideal relationship is based on laboratory tests and more homogeneous materials, so it is reasonable that the results here did not correspond to the model result [3]. The study of Fäth et al. (2022) showed a very good result of a correlation between mean resistivity and mean water content in the main rooting zone, but they used more values, which were measured over a longer period of time. An improvement of the calculation method or a correction with pedotransfer functions, incorporating soil physical parameters, could improve the result of the correlation [12].

## 5. Conclusion

In this thesis, short- and long-term dynamics of soil moisture were investigated in "well" and "poor" structured forest stands. The focus lied particularly on precipitation events and on comparing reactions of the different sites. Thereby it was analysed if a correlation between soil moisture dynamics and the coverage rate of the vegetation layers can be observed. Volumetric water content measurements enabled a detailed representation of the soil water content trends at different depths over the entire study period. The use of the ERT method allowed a detailed visualisation and comparison of vegetation and soil water interactions between different forest structures at a spatial resolution, which would not have been possible only using point measurements.

The results of the long-term soil moisture analysis showed nicely that the "poor" structured forest stands responded more strongly and more abruptly to long-lasting precipitation events or snow-melt. This observation confirmed the assumption that the soil in a "well" structured forest has a higher water storage capacity and thus can absorb more water during a long-term precipitation event. This means in a "well" structured forest the saturation of the pore water content is more delayed, what might reduce the risk of shallow landslides formation. Concerning soil moisture values, the "well" structured forest stands showed higher volumetric water content over the entire study period, which may be due to lower interception, evapotranspiration and higher water infiltration in the more thinned forest stand. This is a clear consequence of the different vegetation coverage rates of the layers, especially the tree layer. In contrast, the studied precipitation events showed less or no responses to precipitation from the "poor" structured forest stands.

The ERT surveys confirmed the low response to the precipitation events at the "poor" site, as only at the "well" structured forest stand water infiltration was clearly visible in the tomograms. At the "poor" structured forest stand, water infiltration was less visible and only in small-scale areas. This might be a consequence from higher canopy cover, as interception makes the largest difference in small precipitation events. Unfortunately, due to difficult forecasting, the investigation did not include long-lasting precipitation events as the thesis intended to.

Nevertheless, the ERT tomograms showed distinct differences between the sites in the rooting zone and the subsoil. The tomograms of the dense forest stand showed more heterogeneous and small-scale soil moisture patterns, indicating more intensive rooting and water consumption of the trees. It showed that the dense forest stand exerted an stronger influence on soil moisture dynamic than the thinned forest stand. The area below the rooting zone in the "well" structured stand showed a more homogeneous resistivity pattern, whereby significantly lower electrical resistivities were measured. In contrast, the "poor" site showed large electrical resistivity patterns lower than 1 m depth, which might be formed by bedrock and different water drainage.

In order to provide more detailed conclusions regarding the formation of shallow landslides, it would be important to further perform ERT survey during longer-lasting precipitation events, to focus on the impact of extreme precipitation events. To reduce the large structural differences between the sites, ERT measurements could be performed at site Well002, as the site has higher canopy cover. This would allow a comparison of less extreme structural differences and thus the interception effect would be reduced, which might had the largest effect for the results in this thesis. A comparison of ERT results from several sites, also from the "poor" structured forest stands, would provide a better verification of the results.

Overall, for a better understanding, which influences forest structure has on soil water balance and shallow landslides, further investigations over longer time periods are needed. Thereby, particular attention should be given on the planned intervention in the dense forest stand, to exactly observe how it will affect the soil water balance. Better insights about which structural elements cause the greatest impact on soil water balance are required in order to develop specific management instructions for landslide protection forests.

## Acknowledgements

I would like to express my thanks for the great opportunity to complete my Master's thesis at the WSL Institute for Snow and Avalanche Research SLF in Davos. I am grateful for having the chance to look into such an interesting research organisation, and I can look back on a very interesting time in which I have learned a lot. Moreover, I am thankful to be able to contribute to such an important and topical research project.

I would especially like to thank my co-supervisors Alexander Bast and Frank Graf for their support during the past months. The regularly meetings to discuss my methods and results were extremely valuable and a great help in the process of my thesis. Also, the field visits together were very interesting. Further special thanks to my supervisor Peter Bebi for his support and feedback during the process of writing.

Finally, my special thanks go to the many helpers during the field work and the ERT measurements, especially for the heavy towing. Many thanks to Roman Schrott, Fabian Rengel, Nicolo Gianelli and Simon Stegemann. Furthermore, I would like to thank my friends and family for all their proofreading, good advice, and the profound confidence in me that accompanied me during the process of this thesis.



## References

- [1] Wulf Amelung et al. *Scheffer/Schachtschabel: Lehrbuch der Bodenkunde*. Springer Spektrum, 2018. ISBN: 9783662558706. URL: <http://www.weltbild.ch/3/16844950-1/ebook/scheffer-schachtschabel-lehrbuch-der-bodenkunde.html?wea=2225271>.
- [2] Amt für Wald und Naturgefahren. *Anleitung zur Waldbestandeskartierung mit der Checkliste BK94.05*. Chur, 1998. URL: [https://www.gr.ch/DE/institutionen/verwaltung/diem/awn/dokumentenliste\\_afw/3\\_5\\_3\\_2\\_bk\\_checkliste\\_1994\\_5\\_anleitung.pdf](https://www.gr.ch/DE/institutionen/verwaltung/diem/awn/dokumentenliste_afw/3_5_3_2_bk_checkliste_1994_5_anleitung.pdf).
- [3] G. E. Archie. “The Electrical Resistivity Log as an Aid in Determining Some Reservoir Characteristics”. In: *SPE Reprint Series* 55 (1942), pp. 9–16. ISSN: 08910901. DOI: 10.2118/942054-g.
- [4] Alexander Bast, Frank Graf and Peter Bebi. *WaWaRu – Waldstruktur , Wasserhaushalt und flachgründige Rutschungen*. 2019, Date Accessed: 25.04.2022. URL: <https://www.wsl.ch/en/projects/investigating-forest-structure-water-balance-and-shallow-landslides-the-wawaru-project.html>.
- [5] Peter Bebi et al. “Waldentwicklung und flachgründige Rutschungen: eine grossflächige GIS-Analyse”. In: *Schweizerische Zeitschrift für Forstwesen* 170.6 (2019). ISSN: 0036-7818. DOI: 10.3188/szf.2019.0318.
- [6] Guillaume Blanchy et al. “ResIPy, an intuitive open source software for complex geoelectrical inversion/modeling”. In: *Computers and Geosciences* 137. February (2020), p. 104423. ISSN: 00983004. DOI: 10.1016/j.cageo.2020.104423. URL: <https://doi.org/10.1016/j.cageo.2020.104423>.
- [7] Josef Breitsameter. “Untersuchungen zum Feststoffaustrag aus unterschiedlich dicht bewaldeten Kleineinzugsgebieten im Flysch und in den Kalkalpen der Tegernseer Berge”. In: *Forstliche Forschungsberichte München* 154 (1996).
- [8] Bundesamt für Landestopografie. *swisstopo*. 2021, Date Accessed: 07.06.2022. URL: [https://map.geo.admin.ch/?lang=en&topic=ech&bgLayer=ch.swisstopo.pixelkarte-farbe&layers=ch.swisstopo.zeitreihen,ch.bfs.gebaeude\\_wohnungs\\_register,ch.bav.haltstellen-oev,ch.swisstopo.swisstlm3d-wanderwege,ch.astra.wanderland-sperrungen\\_umleitungen&layers](https://map.geo.admin.ch/?lang=en&topic=ech&bgLayer=ch.swisstopo.pixelkarte-farbe&layers=ch.swisstopo.zeitreihen,ch.bfs.gebaeude_wohnungs_register,ch.bav.haltstellen-oev,ch.swisstopo.swisstlm3d-wanderwege,ch.astra.wanderland-sperrungen_umleitungen&layers).
- [9] D. L. Corwin and S. M. Lesch. “Apparent soil electrical conductivity measurements in agriculture”. In: *Computers and Electronics in Agriculture* 46.1-3 SPEC. ISS. (2005), pp. 11–43. ISSN: 01681699. DOI: 10.1016/j.compag.2004.10.005.
- [10] Jonathan Dick et al. “Using repeat electrical resistivity surveys to assess heterogeneity in soil moisture dynamics under contrasting vegetation types”. In: *Journal of Hydrology* 559 (2018), pp. 684–697. ISSN: 00221694. DOI: 10.1016/j.jhydrol.2018.02.062. URL: <https://doi.org/10.1016/j.jhydrol.2018.02.062>.
- [11] Heinz Ellenberg and Frank Klötzli. *Waldgesellschaften und Waldstandorte der Schweiz*. Vol. 48/4. 494. Zürich: Beer, 1972.
- [12] Julian Fäth, Julius Kunz and Christof Kneisel. “Monitoring spatiotemporal soil moisture changes in the subsurface of forest sites using electrical resistivity tomography (ERT)”. In: *Journal of Forestry Research* 33.5 (2022), pp. 1649–1662. ISSN: 19930607. DOI: 10.1007/s11676-022-01498-x. URL: <https://doi.org/10.1007/s11676-022-01498-x>.
- [13] Monika Frehner, Brächt Wasser and Raphael Schwitter. *Nachhaltigkeit und Erfolgskontrolle im Schutzwald. Wegleitung für Pflegemassnahmen in Wäldern mit Schutzfunktion*. Bern: Bundesamt für Umwelt BAFU, Volzug Umwelt, 2005, p. 564.
- [14] Frank Graf et al. “Pflanzenwirkungen zum Schutz vor flachgründigen Rutschungen”. In: *WSL Berichte* 56 (2017), p. 42. URL: <https://www.dora.lib4ri.ch/wsl/islandora/object/wsl:12978>.

- 
- [15] Frank Graf et al. “Schutz – Wald – Struktur : Einfluss auf flachgründige Rutschungen”. In: *Ingenieurbiologie, Mitteilungsblatt NR. 3* (2020).
- [16] H. Hager. “Stammzahlreduktion-Die Auswirkungen auf Wasser-, Energie- und Nährstoffhaushalt von Fichtenjungwüchsen”. In: *Forstliche Schriftenreihe, Universität für Bodenkultur* (1988).
- [17] Kevin Hayley et al. “Low temperature dependence of electrical resistivity: Implications for near surface geophysical monitoring”. In: *Geophysical Research Letters* 34.18 (2007), pp. 1–5. ISSN: 00948276. DOI: 10.1029/2007GL031124.
- [18] Kanton Graubünden. *Geoportal der kantonalen Verwaltung Graubünden*, Date Accessed: 10.08.2022. URL: <https://edit.geo.gr.ch/>.
- [19] Klaus Knödel, Gerhard Lange and Hans-Jürgen Voigt. *Environmental Geology*. Springer Berlin Heidelberg, 2007. ISBN: 9783540746690.
- [20] Lore Kutschera and Erwin Lichtenegger. *Wurzelatlas mitteleuropäischer Waldbäume und Sträucher*. 2. Auflage. Leopold Stocker Verlag, 2013.
- [21] E. Landolt et al. *Flora indicativa: Ökologische Zeigerwerte und biologische Kennzeichen zur Flora der Schweiz und der Alpen*. Bern: Haupt, 2010. ISBN: 978-3-258-07461-0.
- [22] Gerhard Markart, Kohl Bernhard and Perzl Frank. “Der Bergwald und seine hydrologische Wirkung - eine überschätzte Grösse?” In: *LWF Wissen 55, Berichte der Bayerischen Landesanstalt für Wald und Forstwirtschaft* (2006).
- [23] Meter Group AG. *User Manual Atmos 41*. 2022, Date Accessed: 17.10.2022. URL: [http://library.metergroup.com/Manuals/20635\\_ATMOS41\\_Manual\\_Web.pdf](http://library.metergroup.com/Manuals/20635_ATMOS41_Manual_Web.pdf).
- [24] Meter Group AG. *User Manual Teros 11/12*. 2022, Date Accessed: 17.10.2022. URL: [http://publications.metergroup.com/Manuals/20587\\_TEROS11-12\\_Manual\\_Web.pdf](http://publications.metergroup.com/Manuals/20587_TEROS11-12_Manual_Web.pdf).
- [25] Meter Group AG. *User Manual Teros 21*. 2022, Date Accessed: 17.10.2022. URL: <http://library.metergroup.com/Integrator%20Guide/18407%20TEROS%2021%20Gen2%20Integrator%20Guide.pdf>.
- [26] Christine Moos et al. “How does forest structure affect root reinforcement and susceptibility to shallow landslides?” In: *Earth Surface Processes and Landforms* 41.7 (2016). ISSN: 10969837. DOI: 10.1002/esp.3887.
- [27] Felix Naef and Carla Thoma. *Hydrologischer Atlas der Schweiz, Tafel 5.9*. Geographisches Institut Universität Bern (GIUB), 2015, Date Accessed: 17.10.2022. URL: [http://www.hadesdaten.unibe.ch/sites/dateien/pdf/Tafel\\_59.pdf](http://www.hadesdaten.unibe.ch/sites/dateien/pdf/Tafel_59.pdf).
- [28] RStudio Team. *RStudio: Integrated Development Environment for R*. Boston, MA: RStudio, PBC, 2022, Version: 2022.2.2.485. URL: <http://www.rstudio.com/>.
- [29] A. Samouëlian et al. “Electrical resistivity survey in soil science: A review”. In: *Soil and Tillage Research* 83.2 (2005), pp. 173–193. ISSN: 01671987. DOI: 10.1016/j.still.2004.10.004.
- [30] Universität Zürich. *Website Methodenberatung Universität Zürich*, Date Accessed: 21.10.2022. URL: <https://www.methodenberatung.uzh.ch>.
- [31] VSS-Expertenkommission (5.08). *Geotechnische Erkundung und Untersuchung Geotechnische Kenngrössen*. Ed. by Schweizerischer Verband der Strassen und Verkehrsfachleute VSS. 2011, Schweizer Norm 670 010.
- [32] Leupold W. et al. *Geologischer Atlas der Schweiz 1:25 000*. Geologische Kommission der Schweiz, 1935, 423 Scaletta (Atlasblatt 9).

- [33] Marco Walser et al. “Merkblatt für die Praxis Der Waldboden lebt – Vielfalt und Funktion der Bodenlebewesen”. In: *Eidg. Forschungsanstalt WSL CH-8903 Birmensdorf* (2018), pp. 1–12. URL: [https://www.researchgate.net/profile/Ivano\\_Brunner/publication/323868516\\_Der\\_Waldboden\\_lebt\\_-\\_Vielfalt\\_und\\_Funktion\\_der\\_Bodenlebewesen/links/5d8b748ca6fdcc255499d3a8/Der-Waldboden-lebt-Vielfalt-und-Funktion-der-Bodenlebewesen.pdf](https://www.researchgate.net/profile/Ivano_Brunner/publication/323868516_Der_Waldboden_lebt_-_Vielfalt_und_Funktion_der_Bodenlebewesen/links/5d8b748ca6fdcc255499d3a8/Der-Waldboden-lebt-Vielfalt-und-Funktion-der-Bodenlebewesen.pdf).
- [34] Adrian Wicki and Christian Hauck. “Monitoring critically saturated conditions for shallow landslide occurrence using electrical resistivity tomography”. In: *Vadose Zone Journal* 21.4 (2022), pp. 1–23. ISSN: 15391663. DOI: 10.1002/vzj2.20204.

## 6. Declaration of Originality



Eidgenössische Technische Hochschule Zürich  
Swiss Federal Institute of Technology Zurich

### Eigenständigkeitserklärung

Die unterzeichnete Eigenständigkeitserklärung ist Bestandteil jeder während des Studiums verfassten Semester-, Bachelor- und Master-Arbeit oder anderen Abschlussarbeit (auch der jeweils elektronischen Version).

Die Dozentinnen und Dozenten können auch für andere bei ihnen verfasste schriftliche Arbeiten eine Eigenständigkeitserklärung verlangen.

Ich bestätige, die vorliegende Arbeit selbständig und in eigenen Worten verfasst zu haben. Davon ausgenommen sind sprachliche und inhaltliche Korrekturvorschläge durch die Betreuer und Betreuerinnen der Arbeit.

**Titel der Arbeit** (in Druckschrift):

The Influence of Forest Structure on Soil Water Balance and Shallow Landslides

**Verfasst von** (in Druckschrift):

Bei Gruppenarbeiten sind die Namen aller Verfasserinnen und Verfasser erforderlich.

**Name(n):**

Temperli

**Vorname(n):**

Annette Janina

Ich bestätige mit meiner Unterschrift:

- Ich habe keine im Merkblatt „Zitier-Knigge“ beschriebene Form des Plagiats begangen.
- Ich habe alle Methoden, Daten und Arbeitsabläufe wahrheitsgetreu dokumentiert.
- Ich habe keine Daten manipuliert.
- Ich habe alle Personen erwähnt, welche die Arbeit wesentlich unterstützt haben.

Ich nehme zur Kenntnis, dass die Arbeit mit elektronischen Hilfsmitteln auf Plagiate überprüft werden kann.

**Ort, Datum**

Davos, 05.12.2022

**Unterschrift(en)**

Bei Gruppenarbeiten sind die Namen aller Verfasserinnen und Verfasser erforderlich. Durch die Unterschriften bürgen sie gemeinsam für den gesamten Inhalt dieser schriftlichen Arbeit.

## 7. Appendix

### A. Vegetation Recording

#### A.1. Results Vegetation Recording

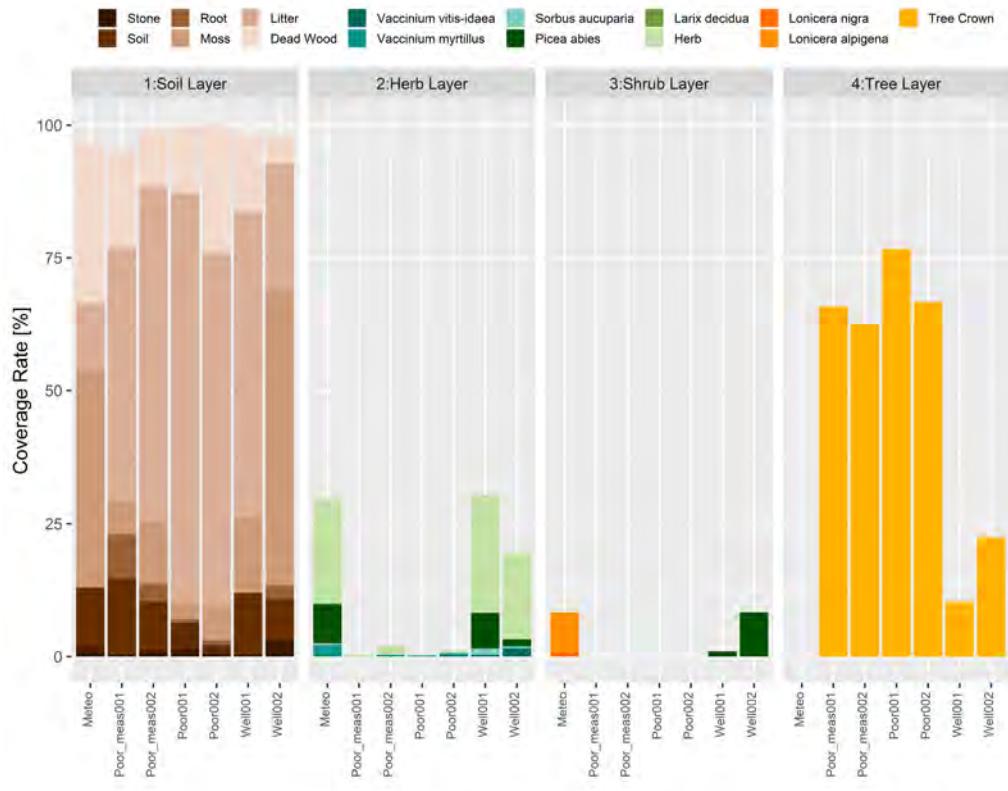


**Figure 38:** Coverage rates in percentage from all vegetation layers (soil, herb, shrub and tree) at 19.05.2022. The stackbars are divided in the shown categories. The brown shades described the categories in the soil layer, the blue-green shades the categories in the herb layer, the red shades the categories in the shrub layer and yellow the canopy cover in the tree layer

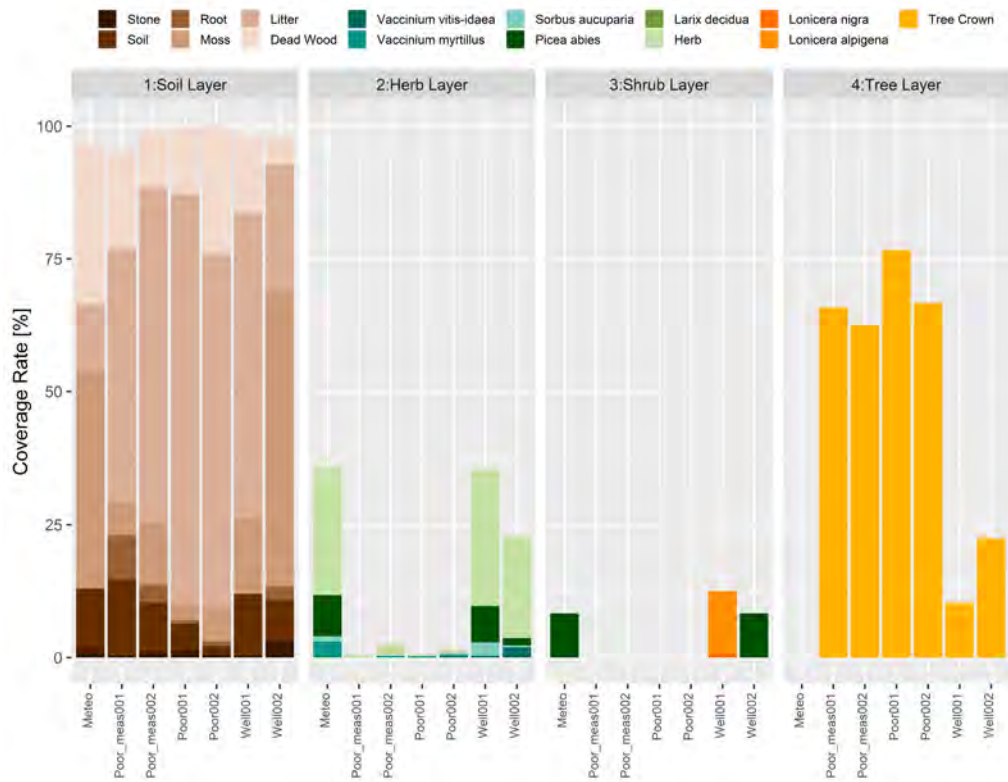


**Figure 39:** Coverage rates in percentage from all vegetation layers (soil, herb, shrub and tree) at 27.05.2022. The stackbars are divided in the shown categories. The brown shades described the categories in the soil layer, the blue-green shades the categories in the herb layer, the red shades the categories in the shrub layer and yellow the canopy cover in the tree layer

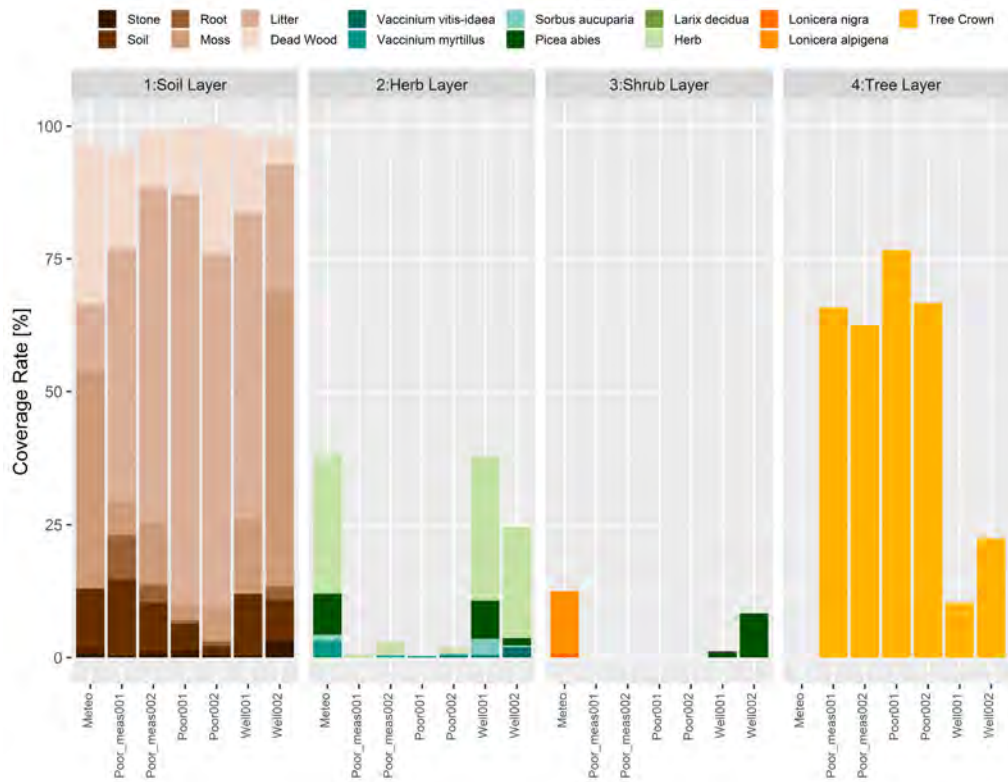


**Figure 40:** Coverage rates in percentage from all vegetation layers (soil, herb, shrub and tree) at 03.06.2022. The stackbars are divided in the shown categories. The brown shades described the categories in the soil layer, the blue-green shades the categories in the herb layer, the red shades the categories in the shrub layer and yellow the canopy cover in the tree layer

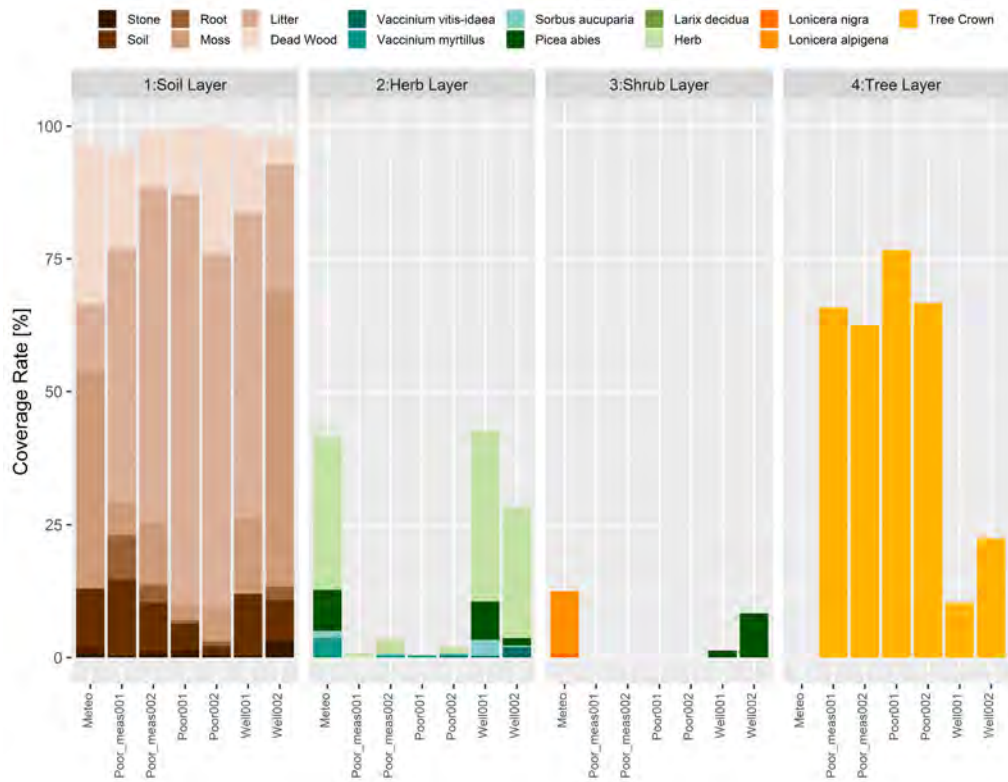


**Figure 41:** Coverage rates in percentage from all vegetation layers (soil, herb, shrub and tree) at 10.06.2022. The stackbars are divided in the shown categories. The brown shades described the categories in the soil layer, the blue-green shades the categories in the herb layer, the red shades the categories in the shrub layer and yellow the canopy cover in the tree layer



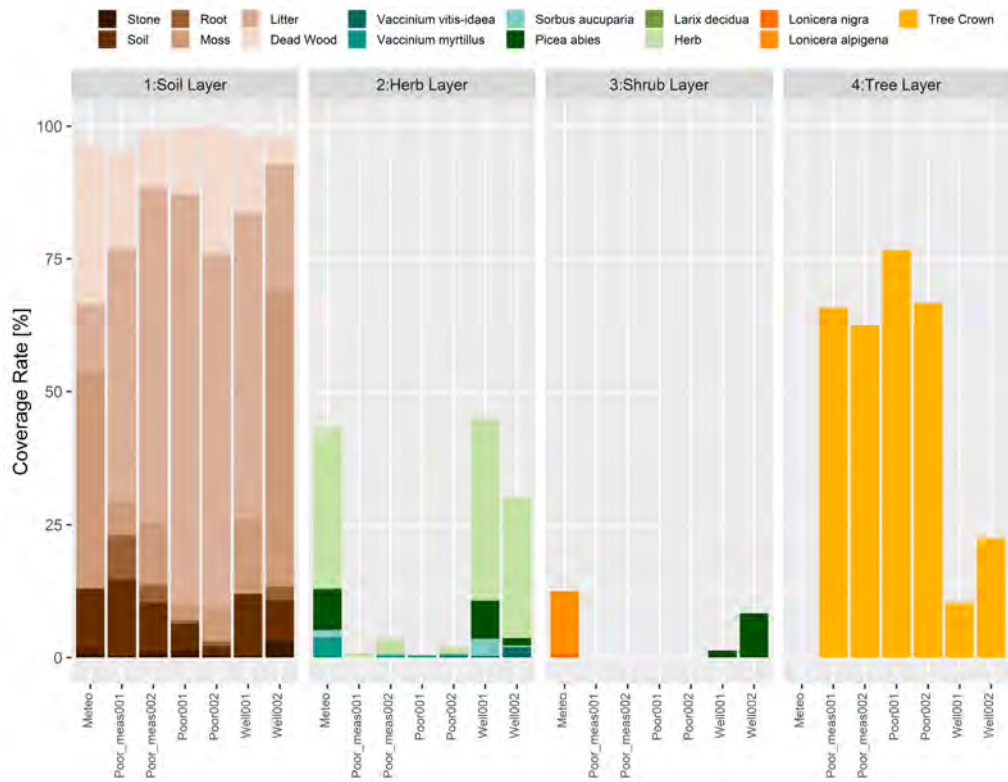


**Figure 42:** Coverage rates in percentage from all vegetation layers (soil, herb, shrub and tree) at 17.06.2022. The stackbars are divided in the shown categories. The brown shades described the categories in the soil layer, the blue-green shades the categories in the herb layer, the red shades the categories in the shrub layer and yellow the canopy cover in the tree layer

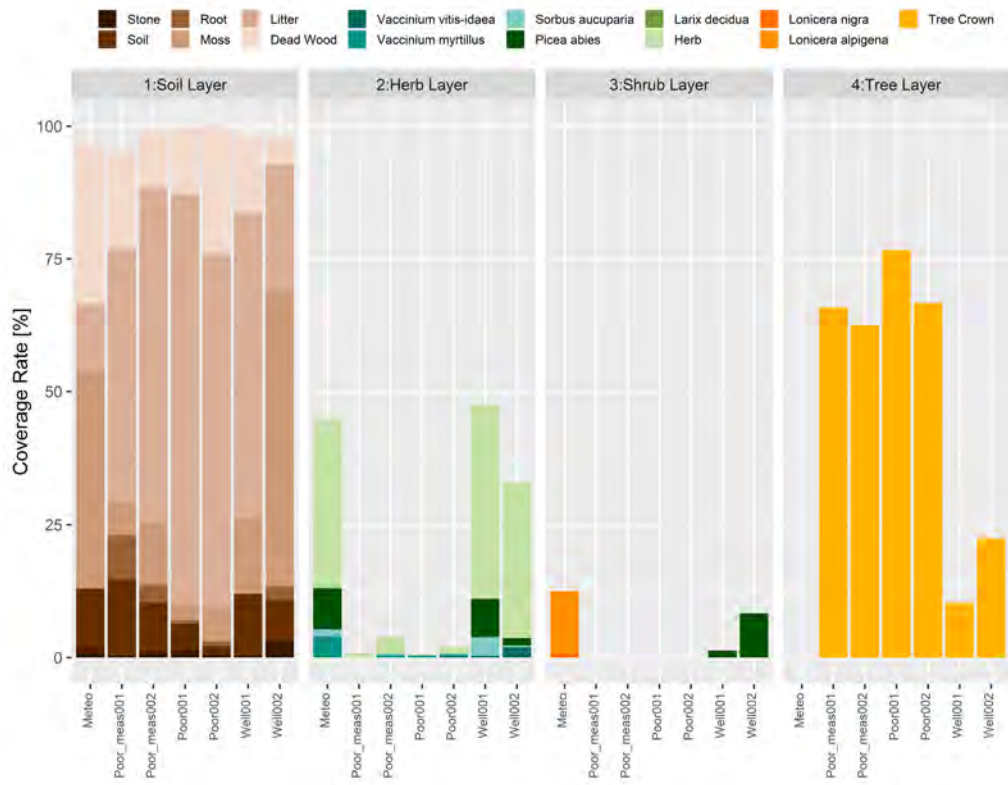


**Figure 43:** Coverage rates in percentage from all vegetation layers (soil, herb, shrub and tree) at 24.06.2022. The stackbars are divided in the shown categories. The brown shades described the categories in the soil layer, the blue-green shades the categories in the herb layer, the red shades the categories in the shrub layer and yellow the canopy cover in the tree layer

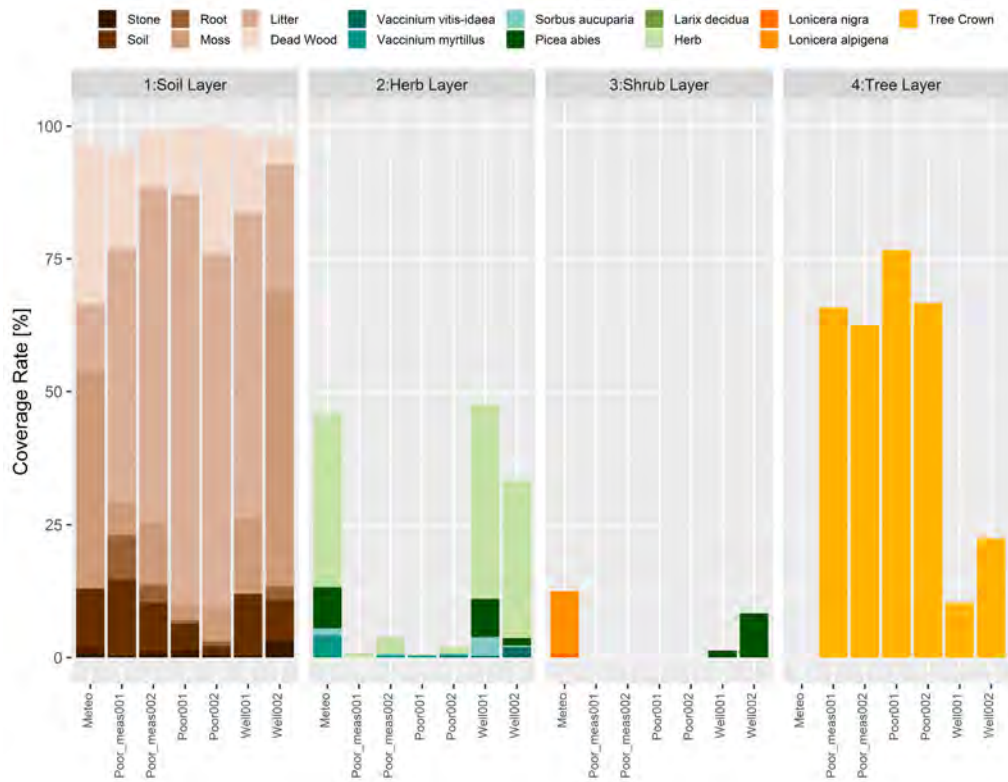


**Figure 44:** Coverage rates in percentage from all vegetation layers (soil, herb, shrub and tree) at 08.07.2022. The stackbars are divided in the shown categories. The brown shades described the categories in the soil layer, the blue-green shades the categories in the herb layer, the red shades the categories in the shrub layer and yellow the canopy cover in the tree layer

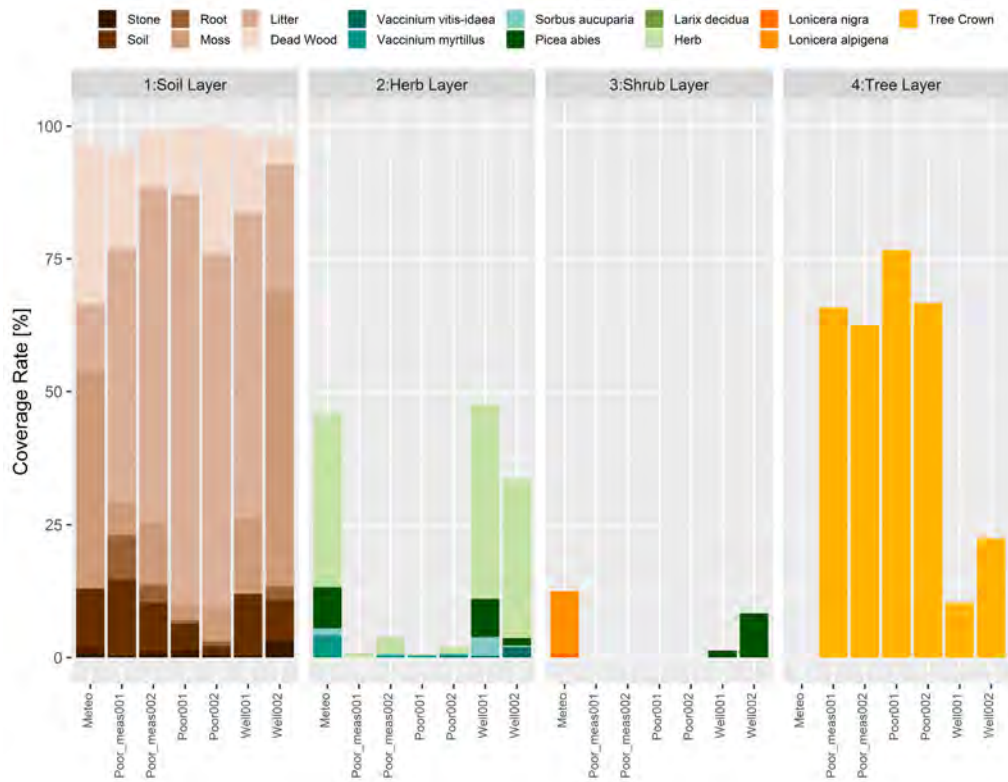


**Figure 45:** Coverage rates in percentage from all vegetation layers (soil, herb, shrub and tree) at 22.07.2022. The stackbars are divided in the shown categories. The brown shades described the categories in the soil layer, the blue-green shades the categories in the herb layer, the red shades the categories in the shrub layer and yellow the canopy cover in the tree layer






## A.2. Species List of Herb and Shrub Layer

**Table 6:** Overview of the recorded species with the corresponding indicators. The ecological indicator values according to Landolt et. al. include the factors: moisture index F, reaction index R, nutrient index N, light index L, temperature index T, continent index K. Site name are abbreviated.

| Specie                 |                             | Ecological Indicator [21] | Site                                     |                       |
|------------------------|-----------------------------|---------------------------|--|-----------------------|
| Anemone apennina       | Apenninen-Windröschen       |                           |  | W2                    |
| Carex Montana          | Berg-Segge                  | 2+w42-334                 | Alkaline, alternately moist or dry       | W1,W2                 |
| Dactylorhiza fuchsii   | Fuchs' Knabenkraut          | 3+w+42-33+3               |  | M,W1                  |
| Daphne mezereum        | Echter Seidelbast           | 3w43-233                  |  | W1,PM2                |
| Dyopteris expansa      | Alpen-Wurmfarn              | 3+w23-22+2                |  | M                     |
| Fragaria vesca         | Wald-Erdbeere               | 333-333                   | Medium, wet                              | M,W1,W2               |
| Hieracium murorum      | Wald-Habichtskraut          | 233-233                   |  | M,W1,W2,PM1,PM2,P1,P2 |
| Homogyne alpina        | Grüner Alpenlattich         | 3+22-323                  | Acid                                     | M,W1,W2               |
| Knautia dipsacifolia   | Wald-Witwenblume            | 3+33-333                  |  | W2                    |
| Larix decidua          | Lärche                      | 322-424                   |  | M                     |
| Lonicera alpigena      | Alpenheckenkirsche          | 3w43-22+2                 |  | M                     |
| Lonicera nigra         | Schwarze Heckenkirsche      | 333-22+3                  |  | M                     |
| Luzula sylvatica       | Gewöhnliche Wald-Hainsimse  | 3+22-232                  | Acid                                     | M,W2,PM1,PM2,P1,P2    |
| Melampyrum sylvaticum  | Wald-Wachtelweizen          | 3+w12-22+3                | Acid and dryness                         | W1,W2,PM2             |
| Oxalis acetosella      | Wald-Sauerklee              | 322-133                   | Surface acidity ( mould indicator)       | M,W1,W2,PM2,P1        |
| Paris quadrifolia      | Vierblättrige Einbeere      | 3+w43-233                 | Medium, wet conditions, heavy clay soils | M,W1,W2               |
| Petasites albus        | Weisse Pestwurz             | 4w+34-233                 | Moist                                    | M,W2                  |
| Phyteuma spicatum      | Ährige Rapunzel             | 333-232                   | Medium, wet                              | W2                    |
| Picea abies            | Fichte                      | 3x3-12+3                  |  | M,W1,W2,PM2           |
| Ranunculus lanuginosus | Wolliger Hanenfuss          | 3+w34-22+2                | Moist                                    | M,W1,W2               |
| Rubus fruticosus       | Brombeere                   |                           | Nutrients                                | M,W1,W2               |
| Sorbus aucuparia       | Vogelbeere                  | 333-333                   |  | M,W1,W2,PM2,P2        |
| Urtica dioica          | Grosse Brennessel           | 3+w+35-33+                | Nutrients                                | M                     |
| Vaccinium myrtillus    | Heidelbeere                 | 3w+12-22+3                | Acid                                     | M,W1,W2,PM2,P1,P2     |
| Vaccinium vitis-idaea  | Preiselbeere                | 2+w12-423                 | Acid and dryness                         | M,W1,W2,P2            |
| Veronica urtifolia     | Nesselblättriger Ehrenpreis | 3+w43-32+3                | Wet, humid conditions                    | M,W1,W2               |



**A.3. Photo Documentation of the Vegetation Recording**

|   |  |
|---|--|
| <b>METEO</b>  |  |
| <b>v_1   meteo:</b>   |  |
| 13.05.2022  | 05.08.2022   |
|    |    |
| <b>v_2_r   meteo:</b>   |  |
| 13.05.2022  | 05.08.2022   |
|   |   |
| <b>v_3_r   meteo:</b>   |  |
| 13.05.2022  | 05.08.2022   |
|  |  |



**Figure 46:** Photo documentation of the vegetation recording from the first (13.05.2022) and last (05.08.2022) recording day at site Meteo.



A VEGETATION RECORDING

| <b>WELL001</b>  |  |
|---|--|
| <b>v_1_r_well001:</b>   |  |
| 13.05.2022  | 19.05.2022   |
|    |    |
| <b>v_2_l_well001:</b>   |  |
| 13.05.2022  | 19.05.2022   |
|   |   |
| <b>v_3_r_well001:</b>   |  |
| 13.05.2022  | 19.05.2022   |
|  |  |



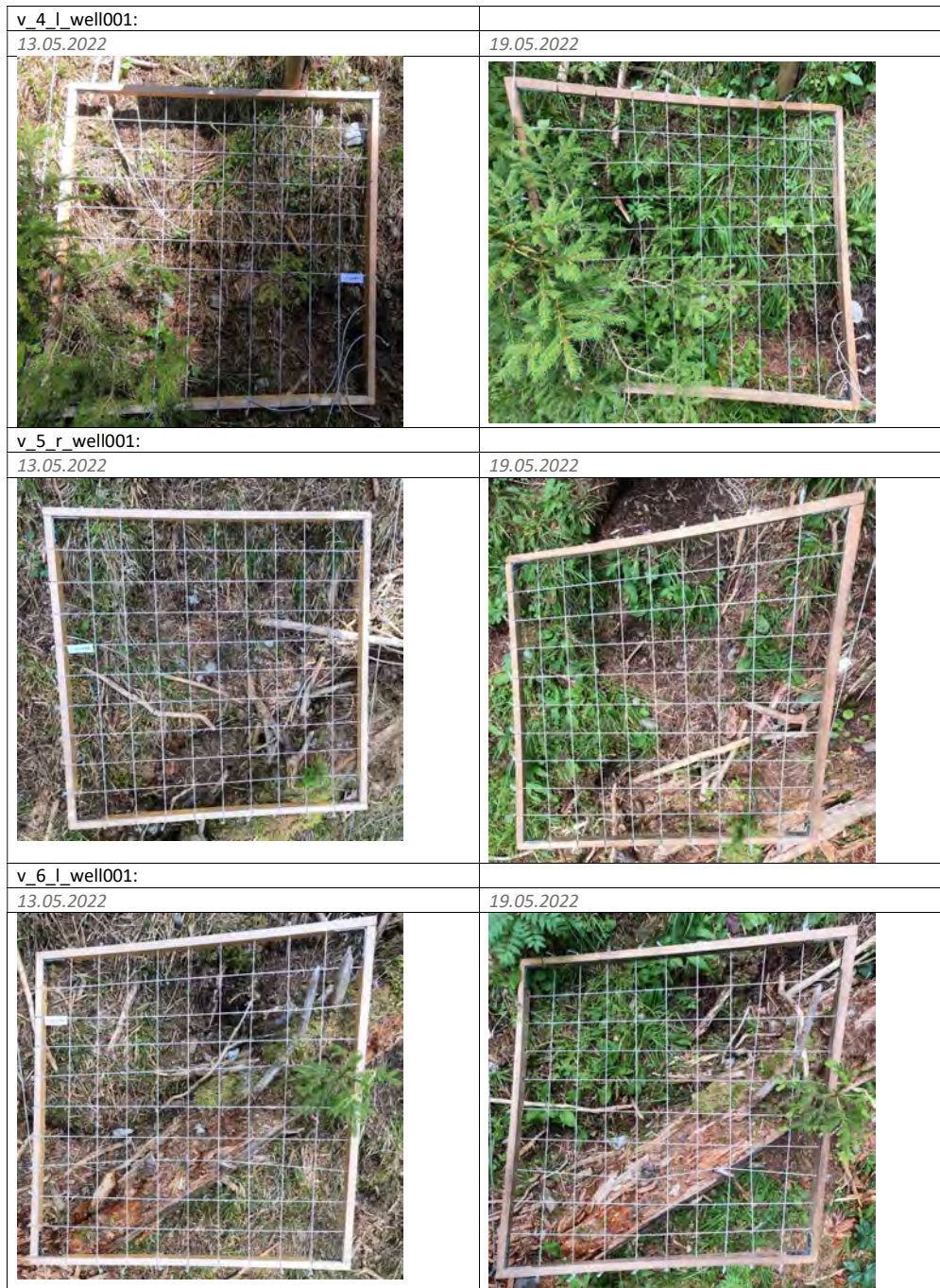


**Figure 47:** Photo documentation of the vegetation recording from the first (13.05.2022) and last (05.08.2022) recording day at site Well001.

A VEGETATION RECORDING

| <b>WELL002</b>  |  |
|---|--|
| <b>v_1_r_well002:</b>   |  |
| 13.05.2022  | 19.05.2022   |
|    |    |
| <b>v_2_l_well002: (frame can not be placed correctly)</b>                           |  |
| 13.05.2022  | 19.05.2022   |
|   |   |
| <b>v_3_r_well002:</b>   |  |
| 13.05.2022  | 19.05.2022   |
|  |  |








**Figure 48:** Photo documentation of the vegetation recording from the first (13.05.2022) and last (05.08.2022) recording day at site Well002.

A VEGETATION RECORDING







|   |  |
|---|--|
| <b>POOR M 001</b>   |  |
| v_1_r_poorM001: (frame can not be placed correctly)                                 |  |
| 13.05.2022  | 19.05.2022   |
|    |    |
| v_2_l_poorM001:   |  |
| 13.05.2022  | 19.05.2022   |
|   |   |
| v_3_r_poorM001:   |  |
| 13.05.2022  | 19.05.2022   |
|  |  |









|   |  |
|---|--|
| v_4_l_poorM001:   |  |
| 13.05.2022  | 19.05.2022   |
|    |    |
| v_5_r_poorM001:   |  |
| 13.05.2022  | 19.05.2022   |
|   |   |
| v_6_l_poorM001: (frame can not be placed correctly)                                 |  |
| 13.05.2022  | 19.05.2022   |
|  |  |

**Figure 49:** Photo documentation of the vegetation recording from the first (13.05.2022) and last (05.08.2022) recording day at site Poor\_meas001.

A VEGETATION RECORDING







|   |  |
|---|--|
| <b>Poor M 002</b>   |  |
| <b>v_1_r_poorM002:</b>  |  |
| 13.05.2022  | 05.08.2022   |
|    |    |
| <b>v_2_l_poorM002:</b>  |  |
| 13.05.2022  | 05.08.2022   |
|   |   |
| <b>v_3_r_poorM002:</b>  |  |
| 13.05.2022  | 05.08.2022   |
|  |  |









|   |  |
|---|--|
| v_4_l_poorM002:   |  |
| 13.05.2022  | 05.08.2022   |
|    |    |
| v_5_r_poorM002:   |  |
| 13.05.2022  | 05.08.2022   |
|   |   |
| v_6_l_poorM002:   |  |
| 13.05.2022  | 05.08.2022   |
|  |  |

**Figure 50:** Photo documentation of the vegetation recording from the first (13.05.2022) and last (05.08.2022) recording day at site Poor\_meas002.

A VEGETATION RECORDING

| <b>POOR 001</b>   |  |
|---|--|
| <b>v_1_l_poor001:</b><br>13.05.2022   | 05.08.2022   |
|    |    |
| <b>v_2_r_poor001:</b><br>13.05.2022   | 05.08.2022   |
|   |   |
| <b>v_3_r_poor001:</b><br>13.05.2022   | 05.08.2022   |
|  |  |



|   |  |
|---|--|
| v_4_l_poor001:  |  |
| 13.05.2022  | 05.08.2022   |
|    |    |
| v_5_r_poor001: (frame can not be placed correctly)                                  |  |
| 13.05.2022  | 05.08.2022   |
|   |   |
| v_6_l_poor001:  |  |
| 13.05.2022  | 05.08.2022   |
|  |  |

**Figure 51:** Photo documentation of the vegetation recording from the first (13.05.2022) and last (05.08.2022) recording day at site Poor001.

A VEGETATION RECORDING

|   |  |
|---|--|
| <b>POOR 002</b>   |  |
| <b>v_1_l_poor002:</b>   |  |
| 13.05.2022  | 19.05.2022   |
|    |    |
| <b>v_2_r_poor002:</b>   |  |
| 13.05.2022  | 19.05.2022   |
|   |   |
| <b>v_3_r_poor002:</b>   |  |
| 13.05.2022  | 19.05.2022   |
|  |  |





**Figure 52:** Photo documentation of the vegetation recording from the first (13.05.2022) and last (05.08.2022) recording day at site Poor002.

## B. Soil Analysis

### B.1. Photo Documentation Soil Profile



**Figure 53:** Soil profile at Well001 with depth of 60 cm. The soil profile was done during the installation of the sensor and data loggers.





**Figure 54:** Soil profile at Poor\_meas001 with depth of 60 cm. The soil profile was done during the installation of the sensor and data loggers.

## C. Logger and Weather Station Data

### C.1. Kruskal-Wallis Test

```

Kruskal-Wallis rank sum test

data:  m³/m³ Water Content 10 (12) by site
Kruskal-Wallis chi-squared = 194942, df = 6, p-value < 2.2e-16

> dunn_10
Dunn (1964) Kruskal-Wallis multiple comparison
p-values adjusted with the Holm method.

  Comparison      Z      P.unadj      P.adj
1  Meteo - Poor_meas001 212.750363 0.000000e+00 0.000000e+00
2  Meteo - Poor_meas002 276.404780 0.000000e+00 0.000000e+00
3  Poor_meas001 - Poor_meas002 100.569670 0.000000e+00 0.000000e+00
4  Meteo - Poor001 348.810362 0.000000e+00 0.000000e+00
5  Poor_meas001 - Poor001 233.511051 0.000000e+00 0.000000e+00
6  Poor_meas002 - Poor001 176.056686 0.000000e+00 0.000000e+00
7  Meteo - Poor002 306.823401 0.000000e+00 0.000000e+00
8  Poor_meas001 - Poor002 148.627604 0.000000e+00 0.000000e+00
9  Poor_meas002 - Poor002 48.058632 0.000000e+00 0.000000e+00
10 Poor001 - Poor002 -148.599662 0.000000e+00 0.000000e+00
11 Meteo - Well001 215.532243 0.000000e+00 0.000000e+00
12 Poor_meas001 - Well001 4.382001 1.175943e-05 1.175943e-05
13 Poor_meas002 - Well001 -96.197787 0.000000e+00 0.000000e+00
14 Poor001 - Well001 -231.015563 0.000000e+00 0.000000e+00
15 Poor002 - Well001 -144.260585 0.000000e+00 0.000000e+00
16 Meteo - Well002 153.483064 0.000000e+00 0.000000e+00
17 Poor_meas001 - Well002 -93.723685 0.000000e+00 0.000000e+00
18 Poor_meas002 - Well002 -194.336005 0.000000e+00 0.000000e+00
19 Poor001 - Well002 -287.068532 0.000000e+00 0.000000e+00
20 Poor002 - Well002 -242.413664 0.000000e+00 0.000000e+00
21 Well001 - Well002 -98.116983 0.000000e+00 0.000000e+00

```

**Figure 55:** Result of Kruskal-Wallis rank sum test and Dunn test with the method "Holm" with the variable VWC at depth 10 cm.

```

Kruskal-Wallis rank sum test

data:  m³/m³ Water Content 30 (12) by site
Kruskal-Wallis chi-squared = 414912, df = 6, p-value < 2.2e-16

> dunn_30
Dunn (1964) Kruskal-Wallis multiple comparison
p-values adjusted with the Holm method.

  Comparison      Z      P.unadj      P.adj
1  Meteo - Poor_meas001 185.49995 0 0
2  Meteo - Poor_meas002 239.00362 0 0
3  Poor_meas001 - Poor_meas002 84.53235 0 0
4  Meteo - Poor001 326.51153 0 0
5  Poor_meas001 - Poor001 230.90187 0 0
6  Poor_meas002 - Poor001 182.60899 0 0
7  Meteo - Poor002 289.99520 0 0
8  Poor_meas001 - Poor002 165.09166 0 0
9  Poor_meas002 - Poor002 80.55826 0 0
10 Poor001 - Poor002 -136.58514 0 0
11 Meteo - Well001 48.91551 0 0
12 Poor_meas001 - Well001 -215.81202 0 0
13 Poor_meas002 - Well001 -300.34388 0 0
14 Poor001 - Well001 -354.18207 0 0
15 Poor002 - Well001 -380.90543 0 0
16 Meteo - Well002 380.85167 0 0
17 Poor_meas001 - Well002 308.66439 0 0
18 Poor_meas002 - Well002 224.08030 0 0
19 Poor001 - Well002 -54.66942 0 0
20 Poor002 - Well002 143.47555 0 0
21 Well001 - Well002 524.60674 0 0

```

**Figure 56:** Result of Kruskal-Wallis rank sum test and Dunn test with the method "Holm" with the variable VWC at depth 30 cm.

```

Kruskal-Wallis rank sum test

data: °C Soil Temperature 10 (12) by site
Kruskal-Wallis chi-squared = 89806, df = 6, p-value < 2.2e-16

> dunnT10
Dunn (1964) Kruskal-Wallis multiple comparison
p-values adjusted with the Holm method.

  Comparison      Z      P.unadj      P.adj
1  Meteo - Poor_meas001 -6.487254 8.741516e-11 2.622455e-10
2  Meteo - Poor_meas002 55.433246 0.000000e+00 0.000000e+00
3  Poor_meas001 - Poor_meas002 97.824661 0.000000e+00 0.000000e+00
4  Meteo - Poor001 -12.028879 2.505400e-33 1.753780e-32
5  Poor_meas001 - Poor001 -8.819435 1.150385e-18 5.751924e-18
6  Poor_meas002 - Poor001 -64.702450 0.000000e+00 0.000000e+00
7  Meteo - Poor002 -11.008008 3.496482e-28 2.097889e-27
8  Poor_meas001 - Poor002 -7.142258 9.181003e-13 3.672401e-12
9  Poor_meas002 - Poor002 -104.960022 0.000000e+00 0.000000e+00
10 Poor001 - Poor002 4.739095 2.146748e-06 4.293496e-06
11 Meteo - Well001 -100.097259 0.000000e+00 0.000000e+00
12 Poor_meas001 - Well001 -147.901344 0.000000e+00 0.000000e+00
13 Poor_meas002 - Well001 -245.729608 0.000000e+00 0.000000e+00
14 Poor001 - Well001 -75.662168 0.000000e+00 0.000000e+00
15 Poor002 - Well001 -140.748393 0.000000e+00 0.000000e+00
16 Meteo - Well002 -97.787280 0.000000e+00 0.000000e+00
17 Poor_meas001 - Well002 -144.281568 0.000000e+00 0.000000e+00
18 Poor_meas002 - Well002 -242.145535 0.000000e+00 0.000000e+00
19 Poor001 - Well002 -73.573312 0.000000e+00 0.000000e+00
20 Poor002 - Well002 -137.126258 0.000000e+00 0.000000e+00
21 Well001 - Well002 3.673901 2.388754e-04 2.388754e-04

```

**Figure 57:** Result Kruskal-Wallis rank sum test and Dunn test with the method "Holm" with the variable VWC at depth 50 cm.

```

Kruskal-Wallis rank sum test

data: °C Soil Temperature 30 (12) by site
Kruskal-Wallis chi-squared = 69104, df = 6, p-value < 2.2e-16

> dunnT30
Dunn (1964) Kruskal-Wallis multiple comparison
p-values adjusted with the Holm method.

  Comparison      Z      P.unadj      P.adj
1  Meteo - Poor_meas001 -58.39923 0.000000e+00 0.000000e+00
2  Meteo - Poor_meas002 -8.35100 6.768722e-17 6.768722e-17
3  Poor_meas001 - Poor_meas002 79.06695 0.000000e+00 0.000000e+00
4  Meteo - Poor001 -52.71578 0.000000e+00 0.000000e+00
5  Poor_meas001 - Poor001 -11.60344 3.958322e-31 7.916645e-31
6  Poor_meas002 - Poor001 -56.77093 0.000000e+00 0.000000e+00
7  Meteo - Poor002 -43.32771 0.000000e+00 0.000000e+00
8  Poor_meas001 - Poor002 23.80779 2.773280e-125 8.319839e-125
9  Poor_meas002 - Poor002 -55.25480 0.000000e+00 0.000000e+00
10 Poor001 - Poor002 25.20383 3.636964e-140 1.454786e-139
11 Meteo - Well001 -145.12886 0.000000e+00 0.000000e+00
12 Poor_meas001 - Well001 -137.02727 0.000000e+00 0.000000e+00
13 Poor_meas002 - Well001 -216.09642 0.000000e+00 0.000000e+00
14 Poor001 - Well001 -66.66675 0.000000e+00 0.000000e+00
15 Poor002 - Well001 -160.82816 0.000000e+00 0.000000e+00
16 Meteo - Well002 -118.25723 0.000000e+00 0.000000e+00
17 Poor_meas001 - Well002 -94.57785 0.000000e+00 0.000000e+00
18 Poor_meas002 - Well002 -173.67748 0.000000e+00 0.000000e+00
19 Poor001 - Well002 -42.40486 0.000000e+00 0.000000e+00
20 Poor002 - Well002 -118.39026 0.000000e+00 0.000000e+00
21 Well001 - Well002 42.50343 0.000000e+00 0.000000e+00

```

**Figure 58:** Result Kruskal-Wallis rank sum test and Dunn test with the method "Holm" with the variable soil temperature at depth 10 cm.

```

Kruskal-Wallis rank sum test

data: m³/m³ Water Content 30 (12) by site
Kruskal-Wallis chi-squared = 414912, df = 6, p-value < 2.2e-16

> dunn_30
Dunn (1964) Kruskal-Wallis multiple comparison
p-values adjusted with the Holm method.

  Comparison      Z P.unadj P.adj
1   Meteo - Poor_meas001 185.49995    0    0
2   Meteo - Poor_meas002 239.00362    0    0
3   Poor_meas001 - Poor_meas002 84.53235    0    0
4   Meteo - Poor001 326.51153    0    0
5   Poor_meas001 - Poor001 230.90187    0    0
6   Poor_meas002 - Poor001 182.60899    0    0
7   Meteo - Poor002 289.99520    0    0
8   Poor_meas001 - Poor002 165.09166    0    0
9   Poor_meas002 - Poor002 80.55826    0    0
10  Poor001 - Poor002 -136.58514    0    0
11  Meteo - Well001 48.91551    0    0
12  Poor_meas001 - Well001 -215.81202    0    0
13  Poor_meas002 - Well001 -300.34388    0    0
14  Poor001 - Well001 -354.18207    0    0
15  Poor002 - Well001 -380.90543    0    0
16  Meteo - Well002 380.85167    0    0
17  Poor_meas001 - Well002 308.66439    0    0
18  Poor_meas002 - Well002 224.08030    0    0
19  Poor001 - Well002 -54.66942    0    0
20  Poor002 - Well002 143.47555    0    0
21  Well001 - Well002 524.60674    0    0
    
```

Figure 59: Result Kruskal-Wallis rank sum test and Dunn test with the method "Holm" with the variable soil temperature at depth 30 cm.

```

Kruskal-Wallis rank sum test

data: °C Soil Temperature 50 (12) by site
Kruskal-Wallis chi-squared = 126172, df = 6, p-value < 2.2e-16

> dunnT50
Dunn (1964) Kruskal-Wallis multiple comparison
p-values adjusted with the Holm method.

  Comparison      Z      P.unadj      P.adj
1   Meteo - Poor_meas001 -97.2050790 0.000000e+00 0.000000e+00
2   Meteo - Poor_meas002 -23.8461739 1.109563e-125 3.328688e-125
3   Poor_meas001 - Poor_meas002 115.8932226 0.000000e+00 0.000000e+00
4   Meteo - Poor001 -85.4140643 0.000000e+00 0.000000e+00
5   Poor_meas001 - Poor001 -16.4702734 5.999864e-61 1.199973e-60
6   Poor_meas002 - Poor001 -82.6749986 0.000000e+00 0.000000e+00
7   Meteo - Poor002 -116.4734118 0.000000e+00 0.000000e+00
8   Poor_meas001 - Poor002 -30.4446610 1.409596e-203 5.638383e-203
9   Poor_meas002 - Poor002 -146.3288120 0.000000e+00 0.000000e+00
10  Poor001 - Poor002 -0.9221604 3.564449e-01 3.564449e-01
11  Meteo - Well001 -210.7315956 0.000000e+00 0.000000e+00
12  Poor_meas001 - Well001 -179.3633192 0.000000e+00 0.000000e+00
13  Poor_meas002 - Well001 -295.2606402 0.000000e+00 0.000000e+00
14  Poor001 - Well001 -85.9822997 0.000000e+00 0.000000e+00
15  Poor002 - Well001 -148.9035379 0.000000e+00 0.000000e+00
16  Meteo - Well002 -180.4281625 0.000000e+00 0.000000e+00
17  Poor_meas001 - Well002 -131.4908499 0.000000e+00 0.000000e+00
18  Poor_meas002 - Well002 -247.4322565 0.000000e+00 0.000000e+00
19  Poor001 - Well002 -58.6169953 0.000000e+00 0.000000e+00
20  Poor002 - Well002 -101.0232289 0.000000e+00 0.000000e+00
21  Well001 - Well002 47.9424079 0.000000e+00 0.000000e+00
    
```

Figure 60: Result Kruskal-Wallis rank sum test and Dunn test with the method "Holm" with the variable soil temperature at depth 50 cm.



## D. Electrical Resistivity Tomography

### D.1. Output Inversion

**Table 7:** Overview of the time-lapse resistivity inversions. The column measurements read shows the number of measurements which were used for the inversion after filtering in pre-processing. The number of inversions describes the number of calculation runs needed to achieve a result in the desired range. The Final RMS Misfit describes the achieved error at the last inversion.

| Time-Lapse Inversion |              |         |                   |              |                  |  |
|----------------------|--------------|---------|-------------------|--------------|------------------|--|
| Date                 | Site         | array   | Measurements read | # Iterations | Final RMS Misfit |  |
| 19.-24. 07.2022      | Well001      | Dip-Dip | 1574              | 4            | 1.54             |  |
|                      |              |         | 1574              | 1            | 1.82             |  |
|                      |              |         | 1574              | 2            | 1.14             |  |
| 19.-24. 07.2022      | Poor_meas001 | Dip-Dip | 1528              | 1            | 1.02             |  |
|                      |              |         | 1528              | 3            | 1.5              |  |
|                      |              |         | 1528              | 6            | 1.16             |  |
| 19.-24. 07.2022      | Well001      | WENSL   | 458               | 3            | 7.99             |  |
|                      |              |         | 458               | 1            | 0.98             |  |
|                      |              |         | 458               | 1            | 1.01             |  |
| 19.-24. 07.2022      | Poor_meas001 | WENSL   | 433               | 1            | 1.01             |  |
|                      |              |         | 433               | 3            | 1.26             |  |
|                      |              |         | 433               | 4            | 1.02             |  |
| 18.-22.08.2022       | Well001      | Dip-Dip | 1603              | 1            | 1.01             |  |
| 18.-22.08.2022       | Poor_meas001 | Dip-Dip | 1603              | 2            | 1                |  |
|                      |              |         | 1484              | 9            | 1.1              |  |
|                      |              |         | 1484              | 9            | 1.13             |  |
| 18.-22.08.2022       | Well001      | WENSL   | 507               | 1            | 1.01             |  |
|                      |              |         | 507               | 1            | 1.32             |  |
| 18.-22.08.2022       | Poor_meas001 | WENSL   | 469               | 5            | 1.2              |  |

**Table 8:** Overview of the output from the individual resistivity inversions. The column measurements read shows the number of measurements which were used for the inversion after filtering in pre-processing. The number of inversions describes the number of calculation runs needed to achieve a result in the desired range. The Final RMS Misfit describes the achieved error at the last inversion.

| Individual Inversion |              |         |                   |   |                  |                  |
|----------------------|--------------|---------|-------------------|---|------------------|------------------|
| Date                 | Site         | array   | Measurements read | # | Iterations       | Final RMS Misfit |
| 05.07.2022           | Well001      | Dip-Dip | 1753              | 5 |                  | 1.07             |
| 06.07.2022           | Well001      | Dip-Dip | 1790              | 6 |                  | 1.04             |
| 07.07.2022           | Well001      | Dip-Dip | 1839              | 6 |                  | 1.08             |
| 08.07.2022           | Well001      | Dip-Dip | 1841              | 5 |                  | 1.17             |
| 15.07.2022           | Well001      | Dip-Dip | 1784              | 8 |                  | 1.06             |
| 19.07.2022           | Well001      | Dip-Dip | 1769              | 6 |                  | 1.06             |
| 21.07.2022           | Well001      | Dip-Dip | 1748              | 7 |                  | 1.2              |
| 22.07.2022           | Well001      | Dip-Dip | 1749              | 6 |                  | 1.03             |
| 24.07.2022           | Well001      | Dip-Dip | 1794              | 6 |                  | 1.03             |
| 18.08.2022           | Well001      | Dip-Dip | 1722              | 6 |                  | 1                |
| 19.08.2022           | Well001      | Dip-Dip | 1714              | 4 |                  | 1.27             |
| 22.08.2022           | Well001      | Dip-Dip | 1815              | 6 |                  | 0.98             |
| 05.07.2022           | Well001      | WENSL   | 507               | 4 |                  | 1                |
| 06.07.2022           | Well001      | WENSL   | 515               | 3 |                  | 1.17             |
| 07.07.2022           | Well001      | WENSL   | 517               | 3 |                  | 1.25             |
| 08.07.2022           | Well001      | WENSL   | 515               | 3 |                  | 1.28             |
| 15.07.2022           | Well001      | WENSL   | 488               | 4 |                  | 1.07             |
| 19.07.2022           | Well001      | WENSL   | 503               | 3 |                  | 1.17             |
| 21.07.2022           | Well001      | WENSL   | 498               | 5 |                  | 0.99             |
| 22.07.2022           | Well001      | WENSL   | 483               | 3 |                  | 1.08             |
| 24.07.2022           | Well001      | WENSL   | 513               | 3 |                  | 1.19             |
| 18.08.2022           | Well001      | WENSL   | 510               | 3 |                  | 1.15             |
| 19.08.2022           | Well001      | WENSL   | 516               | 3 |                  | 1.22             |
| 22.08.2022           | Well001      | WENSL   | 478               | 3 |                  | 1.23             |
| 05.07.2022           | Poor_meas001 | Dip-Dip | 1765              | 5 |                  | 1.12             |
| 06.07.2022           | Poor_meas001 | Dip-Dip | 1810              | 6 |                  | 1                |
| 07.07.2022           | Poor_meas001 | Dip-Dip | 1810              | 6 |                  | 1                |
| 08.07.2022           | Poor_meas001 | Dip-Dip | 1867              | 6 |                  | 1                |
| 15.07.2022           | Poor_meas001 | Dip-Dip | 1784              | 7 |                  | 0.98             |
| 19.07.2022           | Poor_meas001 | Dip-Dip | 1782              | 6 |                  | 1                |
| 21.07.2022           | Poor_meas001 | Dip-Dip | 1753              | 6 |                  | 0.99             |
| 22.07.2022           | Poor_meas001 | Dip-Dip | 1781              | 6 |                  | 1.15             |
| 24.07.2022           | Poor_meas001 | Dip-Dip | 1698              | 7 |                  | 1.05             |
| 18.08.2022           | Poor_meas001 | Dip-Dip | 1691              | 7 |                  | 1.16             |
| 19.08.2022           | Poor_meas001 | Dip-Dip | 1691              | 7 |                  | 1.09             |
| 22.08.2022           | Poor_meas001 | Dip-Dip | 1774              | 7 |                  | 1.08             |
| 05.07.2022           | Poor_meas001 | WENSL   | 513               | 3 |                  | 1.22             |
| 06.07.2022           | Poor_meas001 | WENSL   | 518               | 3 |                  | 1.16             |
| 07.07.2022           | Poor_meas001 | WENSL   | 493               | 4 |                  | 1                |
| 08.07.2022           | Poor_meas001 | WENSL   | 511               | 3 |                  | 1.12             |
| 15.07.2022           | Poor_meas001 | WENSL   | 502               | 4 |                  | 1.18             |
| 19.07.2022           | Poor_meas001 | WENSL   | 478               | 3 |                  | 1.18             |
| 21.07.2022           | Poor_meas001 | WENSL   | 492               | 3 |                  | 1.27             |
| 22.07.2022           | Poor_meas001 | WENSL   | 464               | 4 |                  | 1                |
| 24.07.2022           | Poor_meas001 | WENSL   | 484               | 4 |                  | 1.02             |
| 18.08.2022           | Poor_meas001 | WENSL   | 478               | 4 |                  | 1.15             |
| 19.08.2022           | Poor_meas001 | WENSL   |                   |   | data set invalid |                  |
| 22.08.2022           | Poor_meas001 | WENSL   | 407               | 4 |                  | 1                |



D.2. Inversions with Wenner-Schlumberger Array

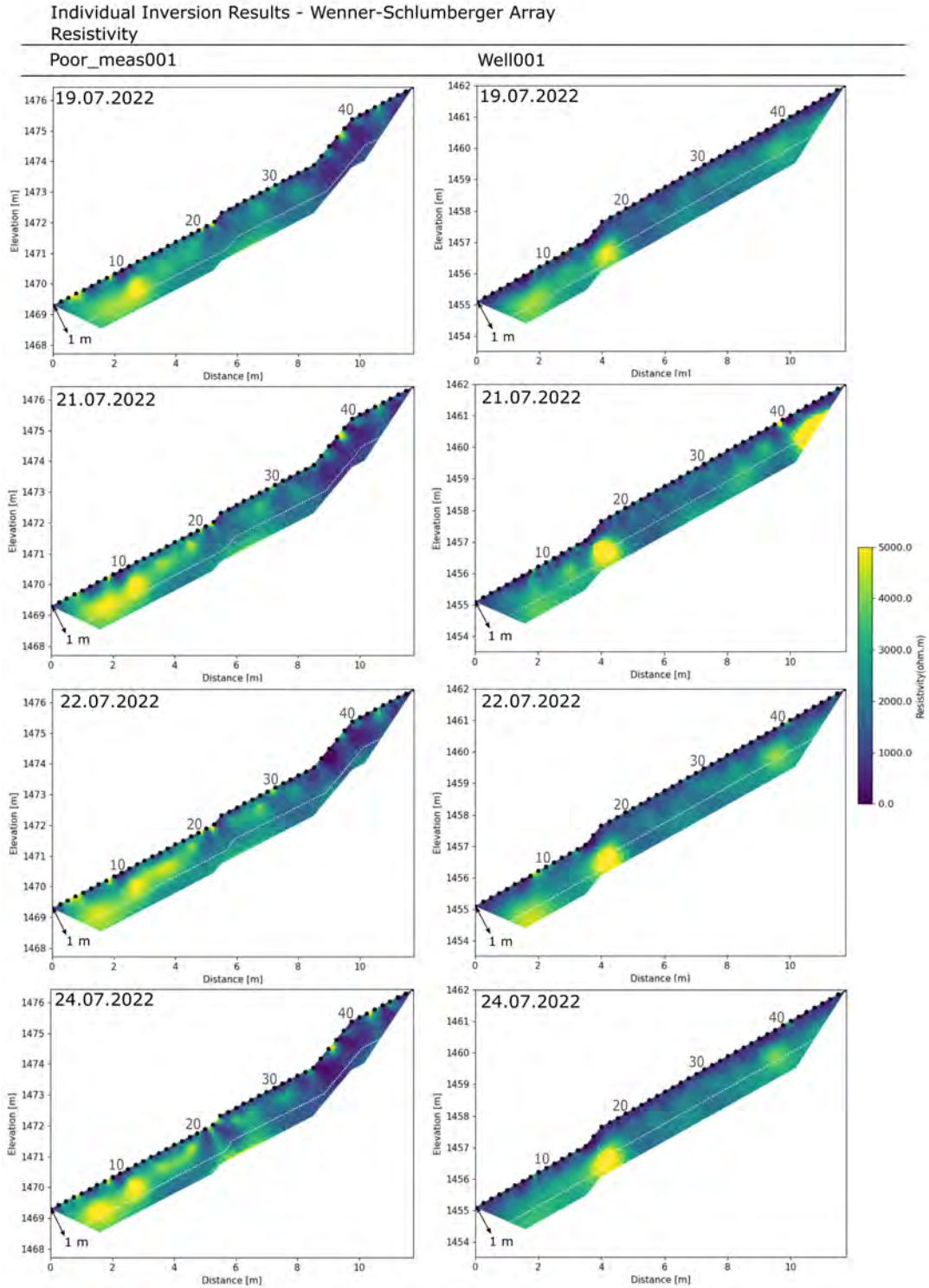


**Figure 61:** Individual electrical resistivity tomograms from the sites Poor\_meas001 and Well001 with the Wenner-Schlumberger array from the July survey. The tomograms from 19., 21., 22. and 24.07. are shown.

## D ELECTRICAL RESISTIVITY TOMOGRAPHY

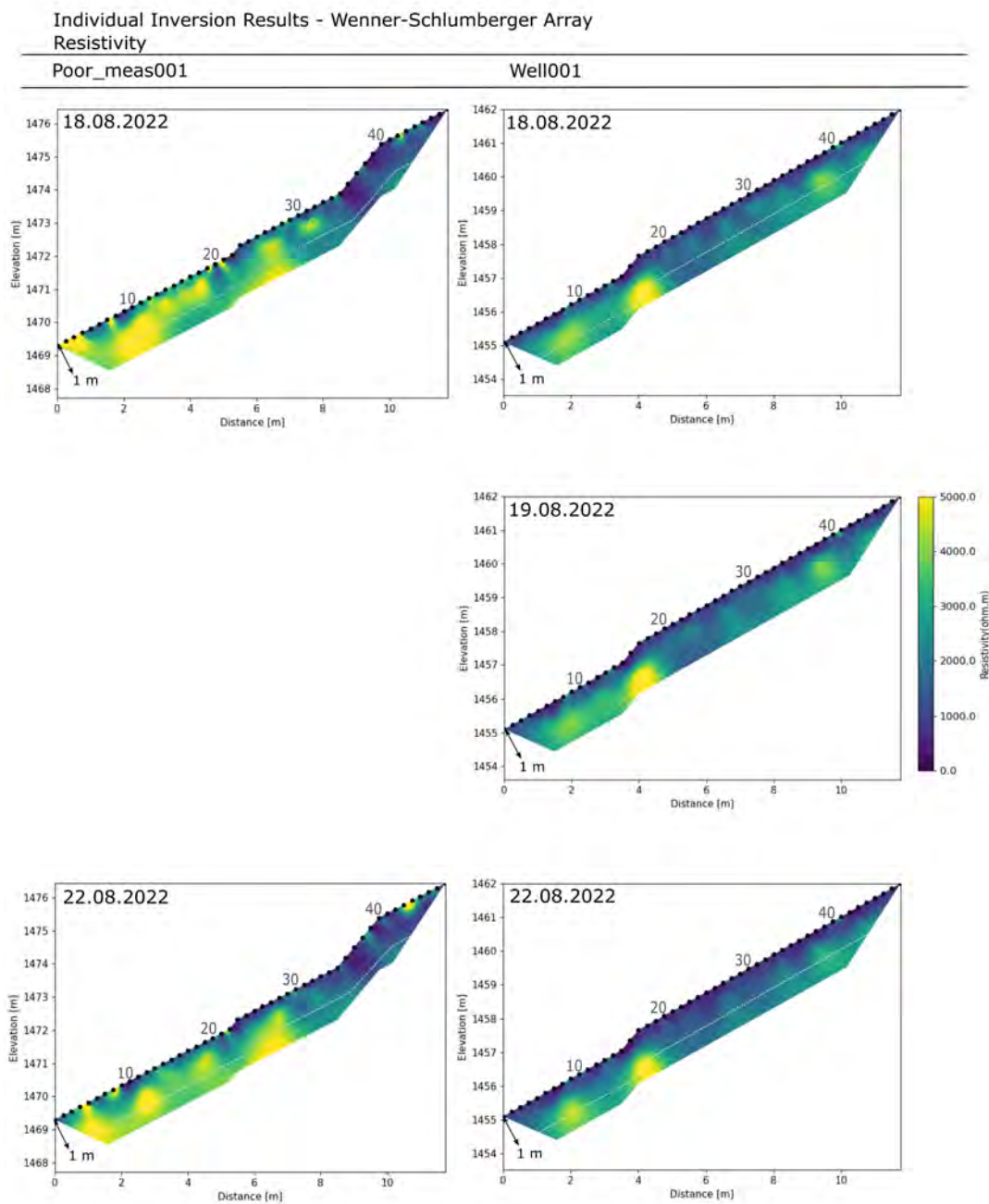


**Figure 62:** Individual electrical resistivity tomograms from the sites Poor\_meas001 and Well001 with the Wenner-Schlumberger array from the August survey. The tomograms from the 18., 19., and 22.08. are shown. The data set from 19.08. at Poor\_meas001 is invalid.

D ELECTRICAL RESISTIVITY TOMOGRAPHY

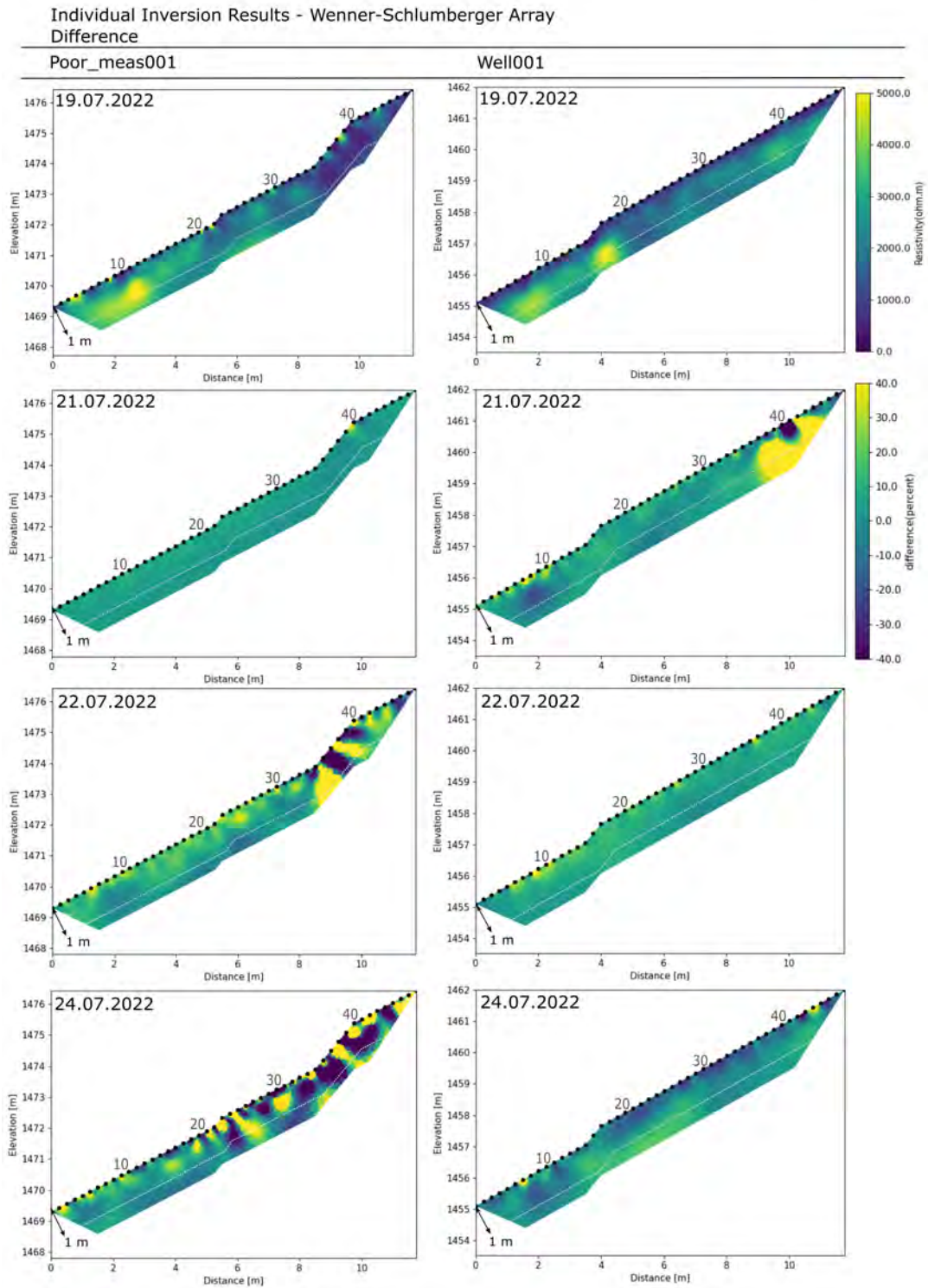


**Figure 63:** Time-lapse electrical resistivity tomograms from the sites Poor\_meas001 and Well001 with the Wenner-Schlumberger array from the July survey. From the 19.07. the electrical resistivity tomogram is shown. From the 21, 22. and 24.07. the difference tomograms are shown.



D ELECTRICAL RESISTIVITY TOMOGRAPHY

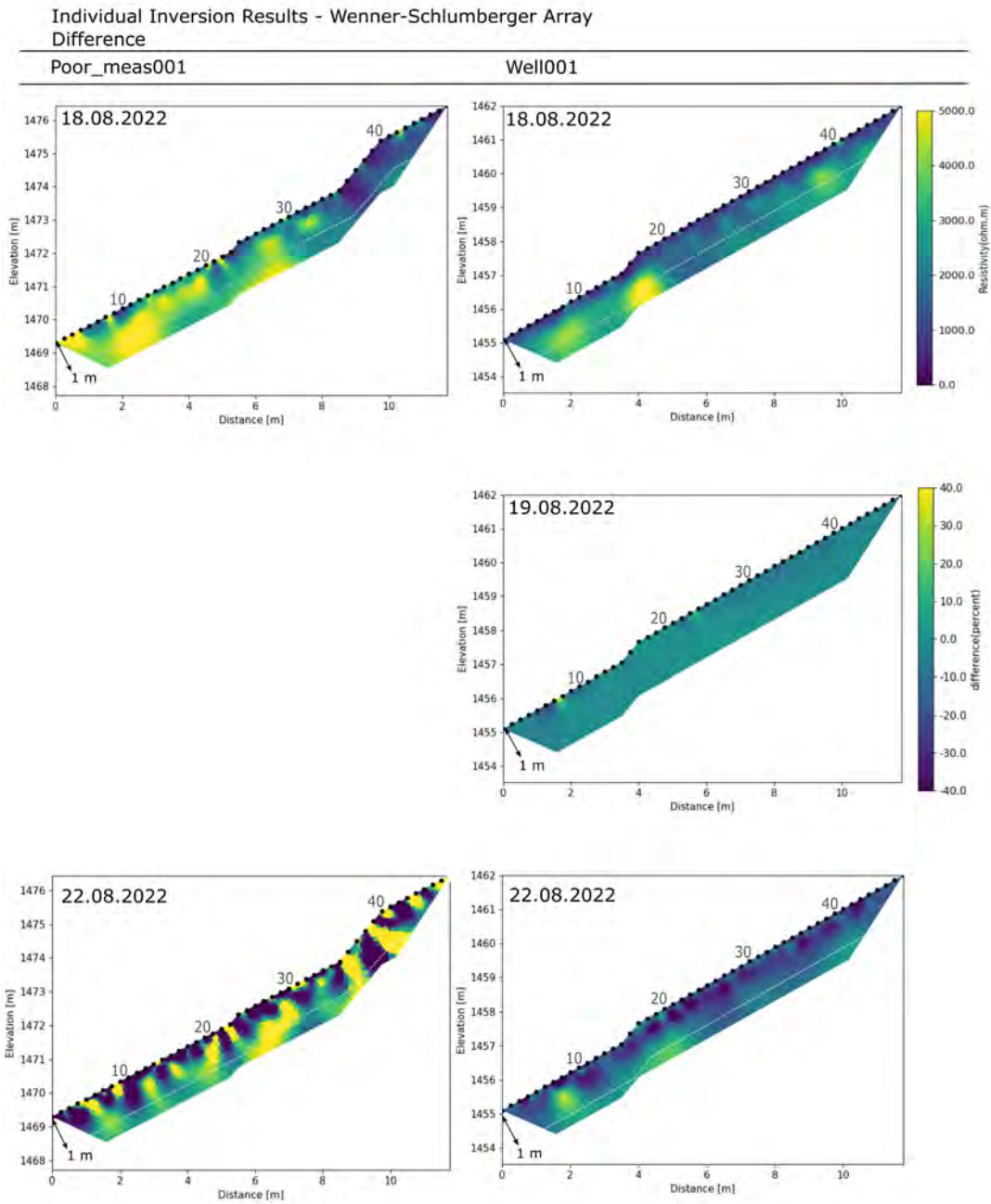


**Figure 64:** Time-lapse electrical resistivity tomograms from the sites Poor\_meas001 and Well001 with the Wenner-Schlumberger array from the July survey. From the 18.08. the electrical resistivity tomogram is shown. From the 19. and 22.08. the difference tomograms are shown. The data set from 19.08. at Poor\_meas001 is invalid.

## D.3. Resistivity Analysis with WENSL Array

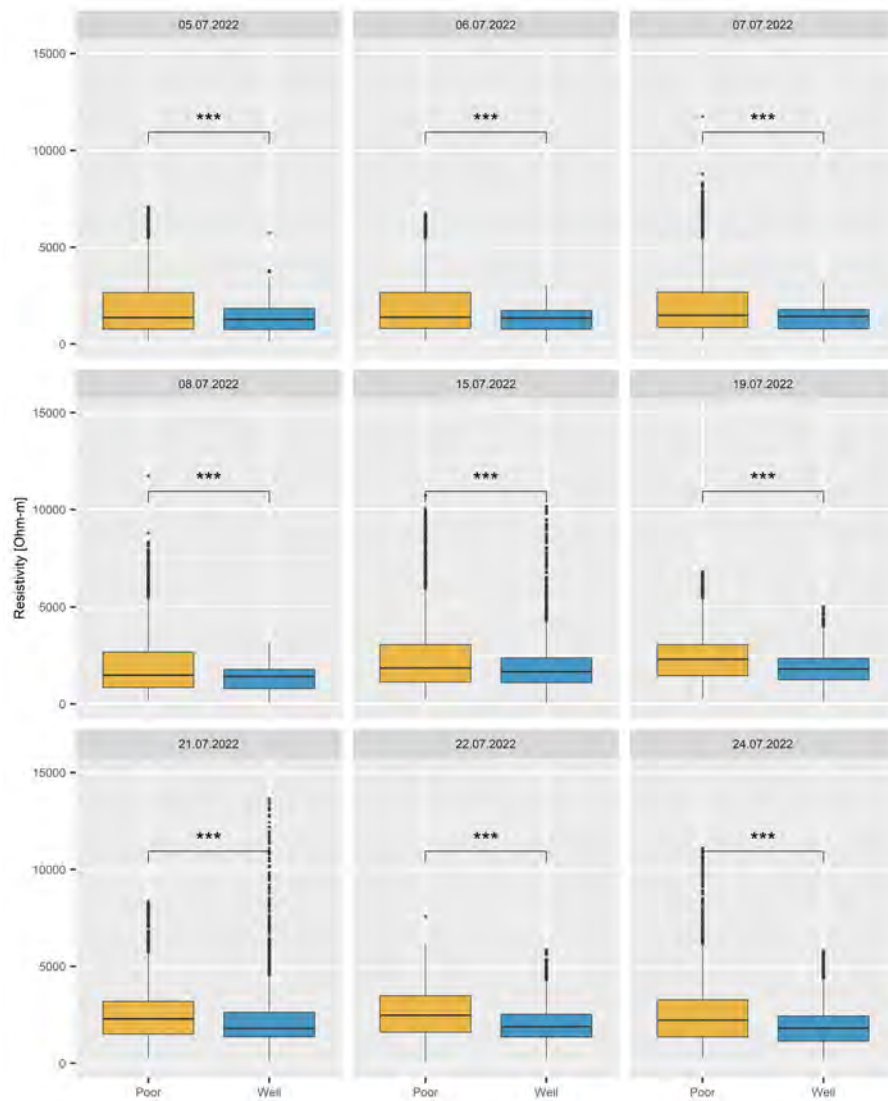


**Figure 65:** Boxplot of the modelled electrical resistivity values of the Wenner-Schlumberger array during July survey. **A** Poor\_meas001 and **B** Well001



## D ELECTRICAL RESISTIVITY TOMOGRAPHY

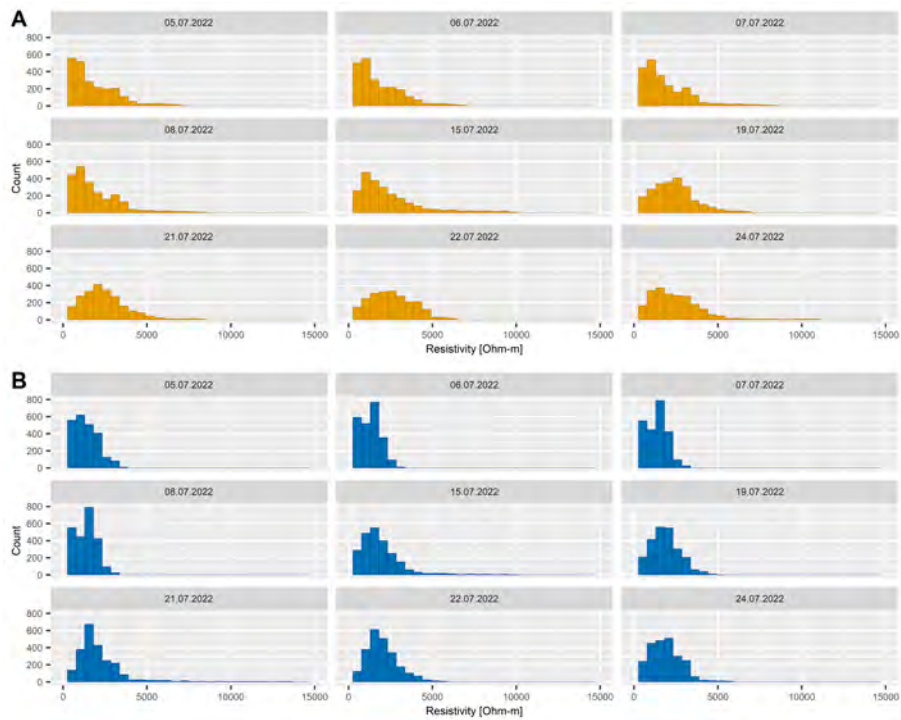


**Figure 66:** Histogram of the modelled electrical resistivity values of the Wenner-Schlumberger array during July survey.

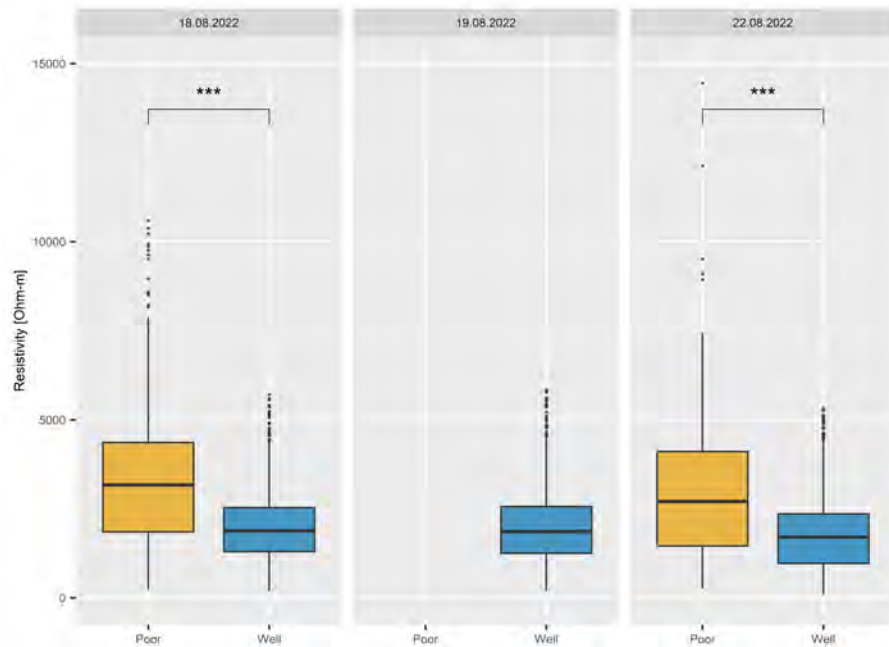


**Figure 67:** Boxplots of the modelled electrical resistivity values of the Wenner-Schlumberger array during August survey.

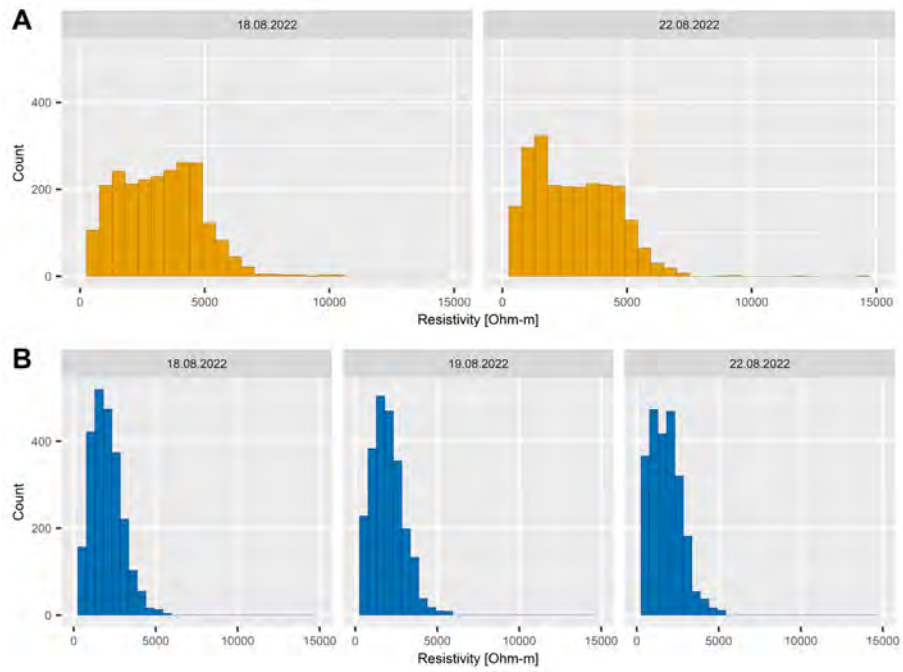


**Figure 68:** Histograms of the modelled electrical resistivity values of the Wenner-Schlumberger array during August survey. **A** Poor\_meas001 and **B** Well001